

THE UNIVERSITY OF CHICAGO

MODELING DUST PRODUCTION, GROWTH, AND DESTRUCTION IN
REIONIZATION-ERA GALAXIES

A DISSERTATION SUBMITTED TO
THE FACULTY OF THE DIVISION OF THE PHYSICAL SCIENCES
IN CANDIDACY FOR THE DEGREE OF
DOCTOR OF PHILOSOPHY

DEPARTMENT OF ASTRONOMY AND ASTROPHYSICS

BY
CLARKE JARETT ESMERIAN

CHICAGO, ILLINOIS

AUGUST 2023

Copyright © 2023 by Clarke Jarett Esmerian
All Rights Reserved

I dedicate this thesis to my parents and my friends for their unconditional and continuous
love and support.

TABLE OF CONTENTS

LIST OF FIGURES	vi
LIST OF TABLES	xi
ACKNOWLEDGMENTS	xii
ABSTRACT	xiv
1 INTRODUCTION	1
2 METHODS AND PARAMETER EXPLORATION	7
2.1 Introduction	7
2.2 Methods	9
2.2.1 Numerical Galaxy Formation Model: Cosmic Reionization on Computers	9
2.2.2 Pathline Sampling: Monte-Carlo Tracers	16
2.2.3 Dust Model: Physics – Creation and Destruction Processes	18
2.2.4 Dust Model: Numerical Integration	24
2.2.5 Correction of Star Formation Rates	27
2.2.6 Calculation of Observable Quantities: M_D , β_{UV} , IRX, τ_{1500}	28
2.3 Results	31
2.3.1 Predictions of Dust Model: Dependence on Dust Model Parameters	31
2.3.2 Effect on Observable Quantities and Comparison to Data	43
2.4 Discussion	48
2.4.1 Numerical Methods: Simulation Self-Consistency, Time-Stepping	48
2.4.2 The Physical Model: Comparison to Previous Efforts and Caveats	49
2.4.3 Prospects for high- z Constraints	52
2.5 Conclusions	52
3 PREDICTIONS FOR THE $Z > 5$ GALAXY POPULATION AND COMPARISON TO OBSERVATIONS	55
3.1 Introduction	55
3.2 Methods	57
3.2.1 Dust Model Parameter Exploration	58
3.3 Results	62
3.3.1 The Mass-Metallicity Relation	62
3.3.2 The Dust Content of High-Redshift Galaxies	64
3.3.3 Forward-Modeled Observable Quantities: Comparison to Data	71
3.4 Discussion	77
3.4.1 Status of Dust Constraints	77
3.4.2 Comparison to Similar Theoretical Work	77
3.5 Conclusion	80

4	ANALYSIS OF THE PREDICTED SPATIAL DISTRIBUTION OF ULTRAVIOLET EMISSION, INFRARED EMISSION, AND ULTRAVIOLET COLOR	83
4.1	Introduction	83
4.2	Methods	84
4.3	Results	87
4.4	Discussion and Conclusion	91
5	CONCLUSION	95
	REFERENCES	99

LIST OF FIGURES

2.1	Simulated galaxy masses, metallicities, and star formation rate as a function of cosmological time. The top panel shows the evolution of the total virial mass, galaxy stellar mass, and galaxy gas mass of the most massive halo in the simulation. The middle panel shows the mass-weighted average galaxy gas and stellar metallicities. The bottom panel shows the star formation rate of the central galaxy, and the same rate corrected by the factor determined by Zhu et al. [2020] to correct stellar masses to observations, stated in Eq. 2.14.	11
2.2	Mass-weighted temperature-density distribution the ISM of our simulated galaxy at $z = 5$	12
2.3	Mass fractions of ISM phases defined by temperature cuts as a function of cosmological time.	13
2.4	Tracer Histories. Solid black lines indicate median tracer quantities as a function of cosmological time. Shaded regions bound the 16th and 84th percentile tracer quantities. The top right panel additionally shows the molecular-fraction weighted average tracer temperature $\langle T \rangle_{\text{H}_2}$ in blue. The bottom left panel shows the metallicity production rates due to AGB stars in blue.	14
2.5	Maps of the simulation metallicity (left panel), tracer metallicity (defined by Eq. 2.11, middle panel), and their ratio (right panel) at the final snapshot of our simulation are shown. Values for tracers in the same cell are averaged. The statistical error in the tracer paths due to their probabilistic nature results in an approximately uniform tracer metallicity across the galactic disk, while the simulation metallicity displays a clear gradient.	25
2.6	The top panel shows the evolution of both simulation (black) and tracer (blue) metallicity as a function of time in the simulation, while the bottom shows their ratio. The solid lines in the top panel show the median tracer value at each snapshot, while the shaded regions enclose the 16th and 84th percentiles. The bottom shows the same for their ratio. By $\sim 800\text{Myr}$, their ratio is close to unity, indicating that the tracer metallicity reflects the simulation metallicity in an average sense. Before that time, however, the tracer metallicity is biased low. We discuss the correction of this bias in Section 2.2.4.	26
2.7	Dust-to-metal ratios (top panel) and the contributions of each process to dust growth with default parameters (bottom panel). Solid lines show mean values for all tracers, and the shaded region on the top panel bounds the 16th and 84th percentiles at each timestep. On the top panel, the solid black line shows f^{dep} and the dashed black line shows $y_{D,\text{SN}} = y_{D,\text{AGB}}$. The rapid variation in simulated ISM quantities sampled by the tracers (as shown in Figure 2.4) result in rapid variation of of these rates, so for readability we have smoothed the lines on the bottom panel with a boxcar average of width 10 Myr.	32
2.8	Effect of Zhu et al. [2020] correction for the SFR rate. D/Z is initially suppressed relative to the default value because of the increased destruction rate due to supernova remnants, but much more rapidly transitions to $\sim f^{\text{dep}}$ because of the enhanced ISM accretion rate due to higher metallicity.	33

2.9	Effect of tying dust destruction rates to local ISM gas temperature. The grey line adopts sputtering destruction rates $\dot{D}_{\text{dest}} = \dot{D}_{\text{sputt}}$. This line is invisible because the dashed blue and dotted green lines – both attempts to increase the growth rate of the dust due to ISM accretion \dot{D}_{accr} (the former by setting the temperature of the cold gas in the accretion term to the simulation temperature, the latter by additionally setting the cold gas fraction to the neutral hydrogen fraction) – are visually indistinguishable. Thus no reasonable modification to the \dot{D}_{accr} overcomes the dominance of the thermal sputtering rate. This is true even if the sputtering is additionally decreased by a factor of 10, as shown with the red dot-dashed line.	34
2.10	Effect of varying production yield $y_{D,\text{SN}} = y_{D,\text{AGB}} = y_D$ on dust evolution. Solid lines show mean values for all tracers, shaded regions encompass tracer 16th and 84th percentiles.	35
2.11	No SN dust production. The default value $y_{D,\text{AGB}} = 0.1$ is used in both cases, while the magenta lines show the predictions of the model when SN production is turned off completely $y_{D,\text{SN}} = 0$. Solid lines and shaded regions are defined in the same way as the previous figure.	36
2.12	Effect of varying supernova remnant destruction efficiency C_{dest}	39
2.13	Effect of varying maximum ISM metal depletion fraction f^{dep}	40
2.14	Effect of varying ISM accretion rate uncertainty/clumping factor C_{accr} and the cold phase gas temperature T_{cold} (which are degenerate, as explained in the text).	42
2.15	Dust mass for representative models as a function of cosmic time (left panel) and stellar mass (right panel). The right panel also contains observational data on the dust masses of galaxies at high redshift $z > 5$ from Hashimoto et al. [2019], Laporte et al. [2017], Schaerer et al. [2015], Tamura et al. [2019], Watson et al. [2015] and Dayal et al. [2022].	43
2.16	Ultraviolet 1500Å luminosities (top panel) and optical depths (bottom panel). Data in the bottom panel are from Ferrara et al. [2022]. Colors are the same as in Figure 2.15.	44
2.17	UV β slope as a function of stellar mass (left panel) and UV AB absolute magnitude (right panel). Grey points are a compilation of observational data for $z > 5$ galaxies from the literature: Schaerer et al. [2015, circles], Ferrara et al. [2022, downward triangles], Finkelstein et al. [2012, plus-signs], Bouwens et al. [2014, hexagons], Dunlop et al. [2013, diamonds], Bhatawdekar and Conselice [2021, stars], Wilkins et al. [2011, filled x], Dunlop et al. [2012, pentagons], and Wilkins et al. [2016, squares].	45
2.18	Maps of stellar surface density (left panel), average dust surface density (middle panel), and average stellar optical depth to dust (right panel) at $z = 5.2$. Quantities are projected along a random axis with respect to the galaxy (the coordinate z axis).	45

2.19	Infrared luminosity as a function of stellar mass (top panel) and IRX- β_{UV} relationship (bottom panel). Since we do not self-consistently calculate dust temperatures from the simulation, we show predictions for a reasonable range in the top panel. The bottom panel assumes $T_D = 40\text{K}$	46
3.1	Spatially-resolved D/Z vs Z relations. Each panel shows the 2D pdf of mass for D/Z vs Z in the ISM of the most massive galaxy at the last snapshot. Different panels correspond to different dust models.	59
3.2	Mass-Metallicity Relation. The galaxy-averaged gas-phase metallicity is shown as a function of stellar mass. Each point represents an individual galaxy at an individual snapshot, colored by redshift. Observational data from galaxies at similar redshifts are from Faisst et al. [2016], Jones et al. [2020], Langeroodi et al. [2022], Nakajima et al. [2023], Heintz et al. [2022], and Williams et al. [2023] converted to mass fraction using $12 + [\text{O}/\text{H}]_{\odot} = 8.71$ and $Z_{\odot} = 0.02$ [Lodders, 2019]	63
3.3	Galaxy-Averaged D/Z vs. Z relations. Each panel shows the evolution of the dust content in our simulated galaxies with a different set of assumed dust model parameters, as indicated by the titles. Each point corresponds to the average D/Z and Z values for an individual galaxy at an individual snapshot. Z is in physical (i.e. mass fraction) units. Points from the same galaxy are connected with grey lines, and colors indicate redshift. The dashed horizontal grey line indicates $D/Z = 0.1$, which is the default production yield in our model and the solid horizontal grey line indicates $D/Z = 0.4$, the value for the Milky Way and a common choice in post-processing analyses (see Discussion).	65
3.4	Dust mass-stellar mass relation. Colors indicate different dust models which include Default and those with varied growth or destruction parameters (i.e. the first two rows of those shown in Fig. 3.3). Each point is a single galaxy at a single redshift, and separate panels are redshift bins. Estimates based on observational data from Sommovigo et al. [2022], Dayal et al. [2022], Hashimoto et al. [2019], Knudsen et al. [2017], Schaerer et al. [2015], Watson et al. [2015], Laporte et al. [2017], Tamura et al. [2019], da Cunha et al. [2015], Marrone et al. [2018], Burgarella et al. [2020, with a redshift for ID27 from Aravena et al. [2016]], Pozzi et al. [2021, with stellar masses from Faisst et al. [2020]], Witstok et al. [2023], and Leńniewska and Michałowski [2019] are shown with the same redshift binning. The predictions of a simpler dust post-processing model on higher-resolution simulations presented in Ma et al. [2019] is shown in the dashed grey line.	66
3.5	Dust-mass stellar-mass relation cont'd. Same as Fig. 3.4 but with Default and the dust models with varied yields (i.e. those in the third row shown in Fig. 3.3).	67

3.6	β_{UV} as a function of UV AB absolute magnitude. Different panels show data for different bins in redshift, different colors are different dust models, the black points indicate values predicted in the absence of dust, and the grey points are a compilation of observational measurements from the literature: Finkelstein et al. [2012, plus-signs], Bouwens et al. [2014, hexagons], Dunlop et al. [2013, diamonds], Bhatwadekar and Conselice [2021, stars], Wilkins et al. [2011, filled x], Dunlop et al. [2012, pentagons], and Wilkins et al. [2016, squares] show sample averages of multiple galaxies, while circles show measurements of individual galaxies with JWST from Roberts-Borsani et al. [2022a], Naidu et al. [2022b], Robertson et al. [2023], and Whittler et al. [2023].	70
3.7	Dust optical depth in the UV vs. absolute UV magnitude. Observational upper constraints from Schaerer et al. [2015], Burgarella et al. [2020], Naidu et al. [2022b], and Ferrara et al. [2022, with absolute UV magnitudes taken from Bouwens et al. [2022b]] are shown. In the lowest redshift bin we also show the predictions from Ma et al. [2018] where high resolution galaxy simulations were post-processed with a simpler dust model. See the discussion for comparison. . .	72
3.8	IRX- β_{UV} relation. Infrared-Excess (IRX) vs. ultraviolet spectral slope β_{UV} for our simulated galaxies in each dust model. Note that a constant dust temperature of $T_D = 40K$ was assumed in calculating all infrared luminosities. The colors and redshift bins are identical to Fig. 3.6. Data shown are from Barisic et al. [2017] [which includes data from Capak et al., 2015, Pavesi et al., 2016], the compilation from Hashimoto et al. [2019], and Bowler et al. [2022].	74
3.9	Infrared luminosity vs. UV luminosity. Colors and observational data are the same as Figure 3.8, with the addition of data from Burgarella et al. [2020]. Additionally, we show predictions without UV dust attenuation in transparent points. These are inconsistent with the simulation, but show the effect of reduced UV opacity with unchanged dust mass.	75
4.1	Images of the most massive galaxy in our box at $z = 5$ with different dust models. The top row shows the 1500\AA UV surface brightness, the middle row shows the spatially resolved UV beta slope (estimated using the 1500\AA and 2500\AA color) and bottom row shows the column density of dust mass (which is proportional to the IR surface brightness in the optically thin regime). Each column shows the predictions of a different set of dust model parameters, as well as the intrinsic UV emission on the leftmost column. Note that no smoothing has been applied to these images, and the pixelation is the result of the simulation grid	84

4.2	UV and IR peak emission offsets. The projected physical distance between the maximum UV emission (accounting for dust attenuation) and the maximum IR emission (as determined by the dust surface density), as a function of UV absolute magnitude (top row) and stellar mass (bottom row). Each point is one of six lines-of-sight for a each snapshot. Data for the most massive galaxy in our box $5 < z < 8.5$ is shown. Different colors correspond to different dust models. Each panel shows different levels of smoothing to capture the effect of observational resolution. Data on the right-most plot are from Table 4 of Inami et al. [2022, with stellar masses from Bouwens et al. [2022b] and Schouws et al. [2022]], whose observations have approximately 0.8 arcsecond resolution in both the IR and UV [McCracken et al., 2012].	88
4.3	Effect of observation resolution on UV and IR morphologies.	89

LIST OF TABLES

2.1	Model Parameters	18
3.1	Explored Parameter Combinations. Note that for each model, any parameter not listed under Key Parameters is the same as the Default model.	60

ACKNOWLEDGMENTS

First and foremost I thank my advisor, Prof. Nick Gnedin. I absolutely would not have obtained a Ph.D. without your support and I very much enjoyed being able to work with you. Your dedication to and patience with your students, the extraordinary sharpness of your intellect, your passion for your field, and (despite all of those qualities) your humility will serve for me as impossibly high standards for the rest of my career. I count myself undeservedly lucky to have had you as a Ph.D. advisor.

I must next thank Prof. Andrey Kravtsov, who was my first research advisor in grad school. Not long after arriving in Chicago I met with you to discuss projects, and at that time I didn't really know exactly what topic I wanted to work on, but after our discussion I initially decided I was most interested in galaxy formation, and that's a decision I have carried through to the end of my Ph.D. I'm very grateful for having had the opportunity to learn from you throughout my time at UChicago – you have taught me more astrophysics than any other single human, and your uncompromising dedication to rigor in your research, the breadth of your scientific contributions, and your encyclopedic knowledge will always inspire me.

I thank Prof. Mike Gladders and Prof. Damiano Caprioli for agreeing to be on my thesis committee, your support and guidance during our committee meetings, and your unique insights into my science.

To especially my advisors and my committee, but also to all of the other scientists with whom I've interacted during my 7 years in this department, I feel extremely privileged to have been able to observe and learn the practice of science from researchers of the absolute highest caliber. Thank you.

This manuscript has been co-authored by Fermi Research Alliance, LLC under Contract No. DE-AC02-07CH11359 with the U.S. Department of Energy, Office of Science, Office of High Energy Physics. This work used resources of the Argonne Leadership Computing

Facility, which is a DOE Office of Science User Facility supported under Contract DE-AC02-06CH11357. An award of computer time was provided by the Innovative and Novel Computational Impact on Theory and Experiment (INCITE) program. This research is also part of the Blue Waters sustained-petascale computing project, which is supported by the National Science Foundation (awards OCI-0725070 and ACI-1238993) and the state of Illinois. Blue Waters is a joint effort of the University of Illinois at Urbana-Champaign and its National Center for Supercomputing Applications. This manuscript is based upon work that is supported by the Visiting Scholars Award Program of the Universities Research Association. This work was completed in part with resources provided by the University of Chicago's Research Computing Center. Our analysis made use of the following publicly available software packages: Matplotlib [Hunter, 2007], SciPy [Jones et al., 2001], NumPy [Walt et al., 2011], COLOSSUS [Diemer, 2018], and yt [Turk et al., 2011].

ABSTRACT

We introduce a model for the explicit evolution of interstellar dust in a cosmological galaxy formation simulation. We post-process a simulation from the Cosmic Reionization on Computers project [CROC, Gnedin, 2014], integrating an ordinary differential equation for the evolution of the dust-to-gas ratio along pathlines in the simulation sampled with a tracer particle technique. This model incorporates the effects of dust grain production in asymptotic giant branch star (AGB) winds and supernovae (SN), grain growth due to the accretion of heavy elements from the gas phase of the interstellar medium (ISM), and grain destruction due to thermal sputtering in the high temperature gas of supernova remnants (SNRs). A main conclusion of our analysis is the importance of a carefully chosen dust destruction model, for which different reasonable parameterizations can predict very different values at the ~ 100 pc resolution of our simulations. We first test this dust model on the most massive galaxy in a $10h^{-1}$ co-moving megaparsec (Mpc) box, for which we find that the total predicted dust mass is somewhat sensitive to parameter choices for the dust model, especially the timescale for grain growth due to accretion in the ISM.

To test whether dust-dependent observable quantities of galaxies at these epochs could be useful for placing constraints on dust physics, we then apply the model to a suite of 11 simulated galaxies with stellar masses from $\sim 10^5 - 10^9 M_\odot$ in the first 1.2 billion years of the universe to make predictions for the dust content of high-redshift galaxies. We explore 9 different sets of dust model parameters, forward modelling observable properties of high-redshift galaxies to compare to data. We find that we are unable to simultaneously match existing observational constraints with any one set of model parameters. Specifically, the models which predict the largest dust masses $D/Z \gtrsim 0.1$ at $z = 5$ – because of high assumed production yields and/or efficient growth via accretion in the ISM – are preferred by constraints on total dust mass and IR luminosities, but these models produce far too much extinction in the UV, preventing them from matching observations of β_{UV} .

To investigate this discrepancy, we analyze the relative spatial distribution of stars and dust as probed by infrared (IR) and ultraviolet (UV) emission. We find that all models predict significant dust attenuation in the central region of the galaxy, resulting in a ring-like morphology for the UV emission. Since IR emission peaks in the center of the galaxy, there are \sim kpc-scale offsets between the points of maximal UV and IR surface brightness when “observed” with infinite resolution, but degrading image resolution to be similar to existing observational capabilities results in no offset between peak brightness in UV and IR. While existing observations only probe galaxies brighter in the UV than the most massive in our sample, they do exhibit much larger offsets that are suggestive of more complicated morphologies. Our results therefore provide strong motivation for the development of a dust model such as the one presented in this dissertation in higher-resolution simulations of galaxy formation which more realistically reproduce the dynamics of the reionization-era ISM.

CHAPTER 1

INTRODUCTION

Cosmic dust is the solid phase of interstellar matter. While it constitutes at most on the order of a few percent of the mass in the Inter-Stellar Medium (ISM) of galaxies [e.g. Rémy-Ruyer et al., 2014, Aniano et al., 2020, Galliano et al., 2021], it is an important source of opacity in the ISM [Draine, 2011], and can thereby have a significant impact on the observable properties of galaxies [e.g. Galliano et al., 2018, Zavala et al., 2021]. A complete physical explanation for the observed properties of the galaxy population throughout cosmic time must therefore account for the dust content – at the very least the amount and spatial distribution – in individual galaxies.

Such an explanation is still incomplete in large part because dust grains are subject to complicated physical processes in a variety of interstellar environments [see Draine, 2003, for a review]. They are observed to be produced in the winds of evolved stars [Lagadec et al., 2008, Srinivasan et al., 2009, Matsuura et al., 2009, Riebel et al., 2012, Nanni et al., 2019, Höfner and Olofsson, 2018] and the remnants of supernova explosions [Dunne et al., 2003, Gomez et al., 2012, De Looze et al., 2017, Matsuura et al., 2011, Sarangi et al., 2018, Micelotta et al., 2018]. They may grow through the accretion of heavy elements in the gas phase of the ISM [Draine, 1990, Dwek, 1998, Weingartner and Draine, 1999, Mattsson and Andersen, 2012, Feldmann, 2015, but see also Ferrara et al. 2016]. They may also be destroyed by various physical processes that dissociate grains such as sputtering and sublimation [Draine and Salpeter, 1979a,b, Jones, 2004, Hoang, 2020].

This complexity is only compounded by the dynamical effects dust itself has on the ISM. Metals depleted from the gas phase onto dust do not contribute to metal-line cooling of hot gas, while the dust grains themselves provide a unique source of some cooling (infrared emission) and heating (photoelectric) processes in the ISM. Dust grain surfaces are thought to catalyze chemical reactions responsible for the most abundant molecules in the ISM. Charged

dust grains dynamically couple the ISM to magnetic fields in regions of low ionization fraction. Moreover, the aforementioned dominance of dust opacity means that regions in which the radiation field is strong enough to be dynamically important will impact gas dynamics through its effect on dust. Consequently, the prediction of the dust content in galaxies requires an accounting for these physical processes – about all of which there remain deep theoretical uncertainties – in a dynamical model of the ISM.

Cosmological, fluid-dynamical galaxy formation simulations can provide such a model. By employing numerical methods that adaptively refine the simulation resolution in the areas of highest density, these simulations can resolve individual galaxy disk scale lengths ($\sim 1\text{kpc}$) in cosmologically representative volumes ($\gtrsim 10\text{Mpc}$, e.g.), or can resolve the disk scale height ($\sim 100\text{pc}$) for the entire cosmological Lagrangian volume of an individual galaxy. Consequently, these models have the ability to simultaneously model the dynamics of the ISM (albeit with a physical fidelity inherently limited by resolution) while self-consistently accounting for the global environment of the galaxy, including its history of star formation and metal enrichment over cosmic time. These simulations have recently achieved success in reproducing many observed galaxy and ISM scaling relations [see e.g. Somerville and Davé, 2015, Naab and Ostriker, 2017, Faucher-Giguère, 2018, Vogelsberger et al., 2020, for recent reviews of galaxy formation simulations]

The explicit coupling of interstellar metal enrichment to the predicted star formation history is commonplace – simulations predict the locations and properties of stellar populations formed from local ISM conditions, and account for the energetic and chemical feedback of these populations on the surrounding ISM based on the tabulated predictions of stellar evolution models [e.g. Leitherer et al., 1999, Conroy and Gunn, 2010]. Metals are then typically assumed to be returned to the gas phase of the ISM and passively advected, modifying the local radiative cooling rates accordingly.

While the dust content of such simulations can be estimated to zeroth-order by assuming

a constant dust-to-metal ratio, recent efforts have begun to include an explicit treatment for the creation, growth, and destruction of dust as a function of local ISM conditions, thereby enabling a prediction of the spatially and temporally varying dust-to-metal ratio self-consistent with the properties of the simulated ISM [e.g. Bekki, 2015, McKinnon et al., 2016, 2017, Aoyama et al., 2018, Gjerger et al., 2018, Hou et al., 2019, Vogelsberger et al., 2019, Davé et al., 2019, Li et al., 2019b, Kannan et al., 2020, Graziani et al., 2020, Li et al., 2021, Granato et al., 2021, Trebitsch et al., 2021, Parente et al., 2022, Choban et al., 2022, Kannan et al., 2022, Lower et al., 2022, Lewis et al., 2023, Hu et al., 2023, Narayanan et al., 2023]. For fully Lagrangian fluid-dynamics solvers or codes with passive tracer particles, this dust modelling can be done in post-processing, such as was done in Hirashita and Aoyama [2019]. These efforts have already provided insights into the physical processes governing dust evolution in galaxies throughout cosmic time. However, they must necessarily contend with the still profound uncertainties in the physics governing dust in the ISM.

The complexity of these processes render any attempt at first-principle estimates of their rates and dependence on ISM properties order-of-magnitude at best. Consequently, the equations governing the evolution of the dust-to-metal ratio include a number of free parameters used to quantify these uncertainties. Ideally, many simulations would be computed with the same initial conditions in which these dust parameters would be systematically varied. This would enable an understanding of their effect on the predicted dust content and comparison with observations for constraints. However, the computational expense of running fully coupled galaxy formation and dust physics simulations severely prohibits the size of this parameter space that can be feasibly explored.

This difficulty is only compounded by the increasingly stringent observational constraints on the dust content of galaxies, and this progress is certain to accelerate in the near future. Already the dust content of galaxies in the local universe has been well characterized [see Galliano et al., 2018, for a recent review], and knowledge of the earlier universe is expanding

rapidly [e.g. Péroux and Howk, 2020, for a recent review]. Spearheaded by large ground-based radio telescopes such as ALMA – which can observe the rest-frame FIR continua associated with thermal dust emission – there are a growing number of galaxies in the reionization era ($z \gtrsim 5$) for which substantial dust content has been indicated by observations [e.g. Bertoldi et al., 2003, Venemans et al., 2012, Willott et al., 2013, Wang et al., 2013, Riechers et al., 2013, Cooray et al., 2014, Watson et al., 2015, da Cunha et al., 2015, Dessauges-Zavadsky et al., 2017, Knudsen et al., 2017, Laporte et al., 2017, Decarli et al., 2017, Venemans et al., 2017, Strandet et al., 2017, Izumi et al., 2018, Marrone et al., 2018, Hashimoto et al., 2019, Tamura et al., 2019, Bakx et al., 2020, Fudamoto et al., 2021, Pozzi et al., 2021, Inami et al., 2022, Bowler et al., 2022]. However, similarly many results place only upper limits on rest-frame FIR emission, or find very blue rest-frame UV colors, both of which naively suggest little or no dust in galaxies of the same epoch [e.g. Walter et al., 2012, Bouwens et al., 2012, Kanekar et al., 2013, Ouchi et al., 2013, Capak et al., 2015, Maiolino et al., 2015, Schaerer et al., 2015, Knudsen et al., 2016, Bradač et al., 2017, Matthee et al., 2019]. Together, these observations suggest an exciting diversity in the dust content of galaxies in the early universe.

These preliminary indications of the cosmic dust content at high redshifts are certain to be completely revolutionized by the explosion of data anticipated from JWST. Its successful launch and commissioning has ushered in a new era of astrophysics, and already galaxies are being found and characterized at earlier cosmic times than ever before [e.g. Robertson et al., 2023]. Because the near-IR wavelength range of JWST instruments (NIRCam and NIRSpec) corresponds to rest-frame UV for reionization-era galaxies, dust attenuation will be measured for the early galaxy population, providing important constraints on dust properties – thus far [Naidu et al., 2022b, Roberts-Borsani et al., 2022a, Whitler et al., 2023], these constraints seem to indicate very little dust obscuration. The sensitivity of radio telescopes like ALMA to FIR continuum dust emission will enable exciting synergies that provide

further information, as has already been demonstrated in Bakx et al. [2023]: they employed this NIR-radio combination to spectroscopically confirm a $z > 12$ galaxy candidate identified with JWST [Naidu et al., 2022b] and place upper limits on its IR luminosity which also suggests minimal dust.

It has also become apparent that a complete accounting for dust effects on galaxies observed with JWST is essential for the interpretation of data – Zavala et al. [2023] and Naidu et al. [2022a] have demonstrated that claims of very high-redshift ($z \gtrsim 10$) galaxies so bright they significantly challenge galaxy formation models can instead be contamination from dusty galaxies at much lower redshifts ($z \lesssim 7$). The full exploitation of high-redshift JWST data for physical constraints on cosmic dawn will benefit fundamentally from accurate dust modeling.

Since the timescales regulating this dust content, while uncertain, are likely comparable to the age of the universe at this epoch [e.g. Hirashita, 2000, Leńniewska and Michałowski, 2019], the observed diversity suggests promise for the ability of high-redshift observations to place unique constraints on the physics of dust in the ISM. However, significant theoretical efforts are needed to bring this promise to fruition: of the existing models that account for dust physics processes in cosmological fluid-dynamical simulations of galaxies in the reionization era [Davé et al., 2019, Graziani et al., 2020, Trebitsch et al., 2021, Lower et al., 2022, Kannan et al., 2022, Lewis et al., 2023], none explores the predictions of more than one set of dust model parameters. This work aims to ameliorate the situation by developing a dust modelling framework that uses the spatially-resolved time-dependent predictions of a galaxy formation simulation calculate the predicted dust content, while being sufficiently light-weight and flexible to enable a thorough exploration of uncertain dust physics parameters. In Chapter 2, we present the model methodology, and its application to a single simulated galaxy. We explore the effects of varying dust model parameters on the predicted dust content of this one galaxy, and their impact on dust-sensitive observables. In Chapter 3, we apply

the model to a suite of simulated galaxies to investigate the dependence of dust properties on model parameters across the galaxy mass range resolved in our simulations, as well as a comprehensive comparison to existing observational data. Chapter 4 investigates the spatially resolved dust content and resulting observable properties of the most massive halo in our suite for different dust model parameter choices. Finally in Chapter 5 we conclude.

CHAPTER 2

METHODS AND PARAMETER EXPLORATION

2.1 Introduction

To enable physical interpretation of these existing and future constraints, in this chapter we introduce a model for the explicit evolution of interstellar dust in a cosmological galaxy formation simulation. Specifically, we post-process a simulation from the Cosmic Reionization on Computers project [CROC, Gnedin, 2014], integrating an ordinary differential equation (ODE) for the evolution of the dust-to-gas ratio along pathlines in the simulation sampled with a tracer particle technique. This model incorporates the effects of dust grain production in asymptotic giant branch (AGB) star winds and supernovae (SN), grain growth in the ISM due to accretion of heavy elements from the gas phase, and grain destruction due to thermal sputtering in high temperature gas of supernova remnants (SNRs). This allows us to predict the fraction of metals in the ISM that are locked up in dust grains as a function of space and time in the simulation and consequently compare dust-dependent observable quantities of high-redshift galaxies with data.

Using tracer particles in post-processing enables us to run many models and fully explore the parameter space of deeply uncertain dust physics processes, admittedly at the expense of self-consistently accounting for dust dynamical effects in the simulation. A fully coupled treatment would be preferable and more realistic, but would prohibit the full exploration of dust model uncertainties due to computational cost. In future work, we plan to implement such a model, the calibration of which will be made feasible by the reduction in the physically interesting dust-model-parameter-space constrained by the post-processing analysis presented in this Chapter and Chapter 2, where we apply the model to a larger sample of galaxies.

The model presented in this Chapter bears many similarities to previous dust modelling

efforts. We base our model largely on the one-zone model presented in Feldmann [2015], which was successful in matching the $z = 0$ dust-to-gas (and dust-to-metal) vs. metallicity relation, and in so doing constrained the characteristic timescale for dust grain growth via accretion in the ISM. While the success of this model is encouraging that it captures the essence of dust physical processes in local galaxies, it is inherently limited by its one-zone nature. This limitation greatly hinders its ability to address questions such as the origin of scatter at constant galaxy metallicity and the spatially resolved dust distribution in galaxies, and leaves serious questions about its applicability in different regimes, such as the era of reionization which is our focus in this work.

We are therefore motivated to apply a model with the same basic physical components to a more sophisticated model for galaxy formation of high-redshift galaxies, provided by the CROC project. Dust models accounting for the same basic physical processes – although often with different assumed parameters and scalings – have been incorporated in fluid dynamical galaxy simulations before, as described in Chapter 1. We are however motivated to develop our model because most previous studies chose not to focus on the prediction of observable galaxy properties in the Epoch of Reionization. Among those that did [Wu et al., 2020, Graziani et al., 2020, Trebitsch et al., 2021, Kannan et al., 2022, Lower et al., 2022, Lewis et al., 2023] none explored the effect of varying the parameters on their dust model, leaving them ill-equipped to evaluate the effect of dust model uncertainties on their predictions. By introducing a flexible post-processing method coupled to state-of-the-art Reionization simulations, we address this current deficiency in the literature.

The structure of this chapter is as follows: in Section 2.2 we review the methods of the CROC simulations, present the methods of our model - both the equations that constitute the physical model and the numerical methods used to solve them, and describe our procedure for predicting observational quantities from our model results. In Section 2.3 we present the preliminary results of the model applied to a simulated massive galaxy ($M_{\star} \approx 2 \times$

$10^9 M_\odot$ by $z = 5$) – both the predictions of its dust content for a wide range of dust model parameters, and the comparisons of these predictions to observational data, as a proof-of-concept. In Section 2.4 we discuss the implications of these results as well as uncertainties in our modeling, comparing to previous efforts. In Section 2.5 we conclude and discuss the main findings resulting from the development of this dust model. This chapter is based on the analysis presented in Esmerian and Gnedin [2022].

2.2 Methods

2.2.1 Numerical Galaxy Formation Model: Cosmic Reionization on Computers

To model the ISM of high-redshift galaxies, we employ the Cosmic Reionization on Computers (CROC) numerical galaxy formation simulations described in Gnedin [2014], Gnedin and Kaurov [2014], Gnedin [2016], to which we refer the reader for details. Here we summarize the main components of the simulation machinery.

CROC Model

CROC uses the Adaptive Refinement Tree (ART) code [Kravtsov, 1999, Kravtsov et al., 2002, Rudd et al., 2008] to solve the three-dimensional inviscid fluid dynamics equations coupled gravitationally to collisionless cold dark matter with cosmological initial and boundary conditions. Cooling and heating processes are accounted for as tabulated in Gnedin and Hollon [2012]. Radiative transfer is fully coupled to the gas dynamics and chemistry and solved using the Optically Thin Variable Edington Tensor (OTVET) approximation [Gnedin and Abel, 2001, Gnedin, 2014]. Molecular hydrogen fractions are calculated from local ISM conditions using the fitting functions of Gnedin and Draine [2014]. Star formation occurs in molecular gas with a fixed depletion time of $\tau_{\text{SF}} = 1.5$ Gyr. Star particles are treated as

single-age stellar populations with a Kroupa [2001] IMF. Stellar feedback effects are incorporated with the delayed cooling subgrid model, adopting a delay timescale of $\tau_{\text{BW}} = 10\text{Myr}$. Star particles source ionizing radiation with an escape fraction $\epsilon_{\text{UV}} = 0.15$.

The specific simulation we ran for this analysis is a cosmological volume $10h^{-1}$ co-moving Mpc on each side, assuming a flat ΛCDM cosmology with $\Omega_{\text{M}} = 0.3036$, $\Omega_{\text{b}} = 0.0479$, $\Omega_{\Lambda} = 0.6964$, and $h = H_0/(100\text{km s}^{-1}\text{Mpc}^{-1}) = 0.6814$. An overdensity on the scale of the simulation box (i.e. the “DC” mode) of $\delta_{\text{DC}} = 0.700869$ was accounted for using supercomoving variables as described in Gnedin et al. [2011]. Adaptive refinement is allowed down to a minimum cell size of 100pc in physical units.

Halo identification is performed with the ROCKSTAR halo finder [Behroozi et al., 2013]. We adopt the virial radius definition corresponding to a redshift-dependent over-density with respect to the critical density defined Bryan and Norman [1998]. We find that during major mergers the halo center identified by ROCKSTAR imperfectly matches the location of the central galaxy, so we re-define the galaxy center as the median of stellar particle positions along each axis, using only stellar particles within the ROCKSTAR identified virial radius – i.e. the median stellar particle x position, y position, and z position. Note that this does not necessarily correspond to the location of an actual star particle – since the median particle position along each axis is not guaranteed to belong to the same particle – but we have confirmed visually that this method provides a good estimate of the central galaxy position. We consider all stellar particles and gas cells within $0.1R_{\text{vir}}$ of this center as belonging to the central galaxy.

Halo and Galaxy Properties

Figure 2.1 shows the evolution of basic simulated galaxy quantities. By the final snapshot of the simulation at $t = 1.18\text{Gyr}$ (corresponding to $z = 5$), the galaxy resides in a dark matter halo of total mass $4.80 \times 10^{11}M_{\odot}$ with a stellar mass of $1.81 \times 10^9M_{\odot}$ and a gas

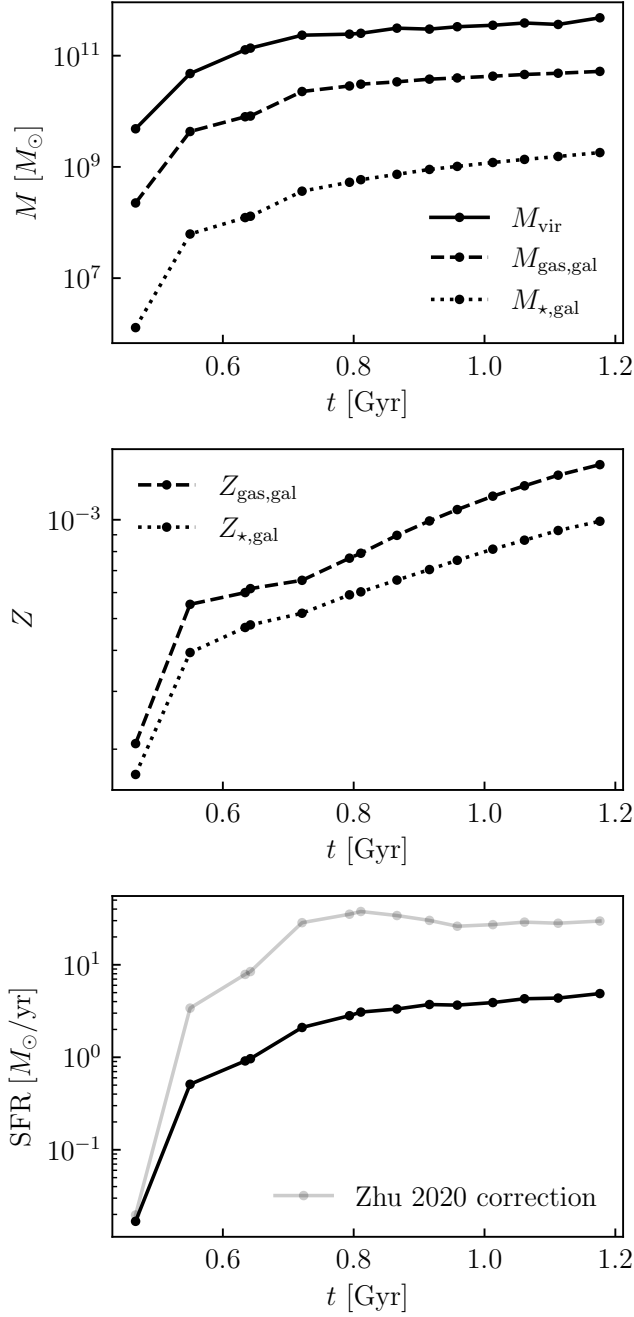


Figure 2.1: Simulated galaxy masses, metallicities, and star formation rate as a function of cosmological time. The top panel shows the evolution of the total virial mass, galaxy stellar mass, and galaxy gas mass of the most massive halo in the simulation. The middle panel shows the mass-weighted average galaxy gas and stellar metallicities. The bottom panel shows the star formation rate of the central galaxy, and the same rate corrected by the factor determined by Zhu et al. [2020] to correct stellar masses to observations, stated in Eq. 2.14.

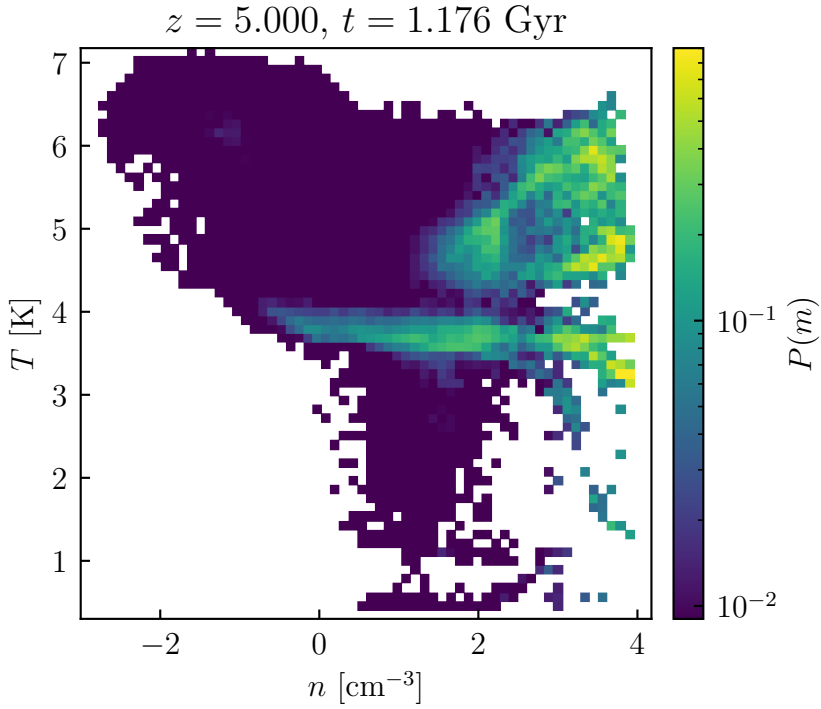


Figure 2.2: Mass-weighted temperature-density distribution the ISM of our simulated galaxy at $z = 5$.

mass of $5.22 \times 10^{10} M_{\odot}$. At this time the central galaxy has a gas and stellar metallicity $Z \approx 10^{-3} = 0.07 Z_{\odot}$, and a star formation rate (averaged over 10Myr) of $4.88 M_{\odot}/\text{yr}$. We focus exclusively on the ISM of this galaxy for the remainder of this chapter.

ISM Phase Structure

Since dust growth and destruction terms depend on the local properties of the ISM, we first examine the distributions of these properties in the simulation. Figure 2.2 shows the temperature-density distribution of the ISM in the final snapshot of the simulation at $z = 5$. At the resolution of this simulation (fixed to 100pc in proper units), the phase structure of the ISM does not appear to be well-resolved, with a substantial fraction of the ISM at unrealistically high temperature ($T \sim 10^5 \text{K}$) given its density ($n \sim 10^3 \text{cm}^{-3}$). We quantify this in Figure 2.3, which shows the mass fraction of four phases defined by temperature cuts:

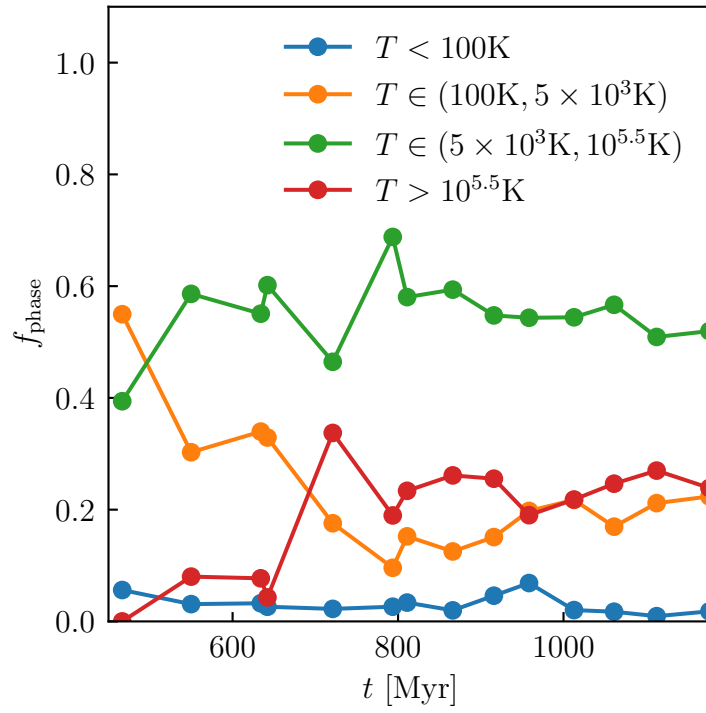


Figure 2.3: Mass fractions of ISM phases defined by temperature cuts as a function of cosmological time.

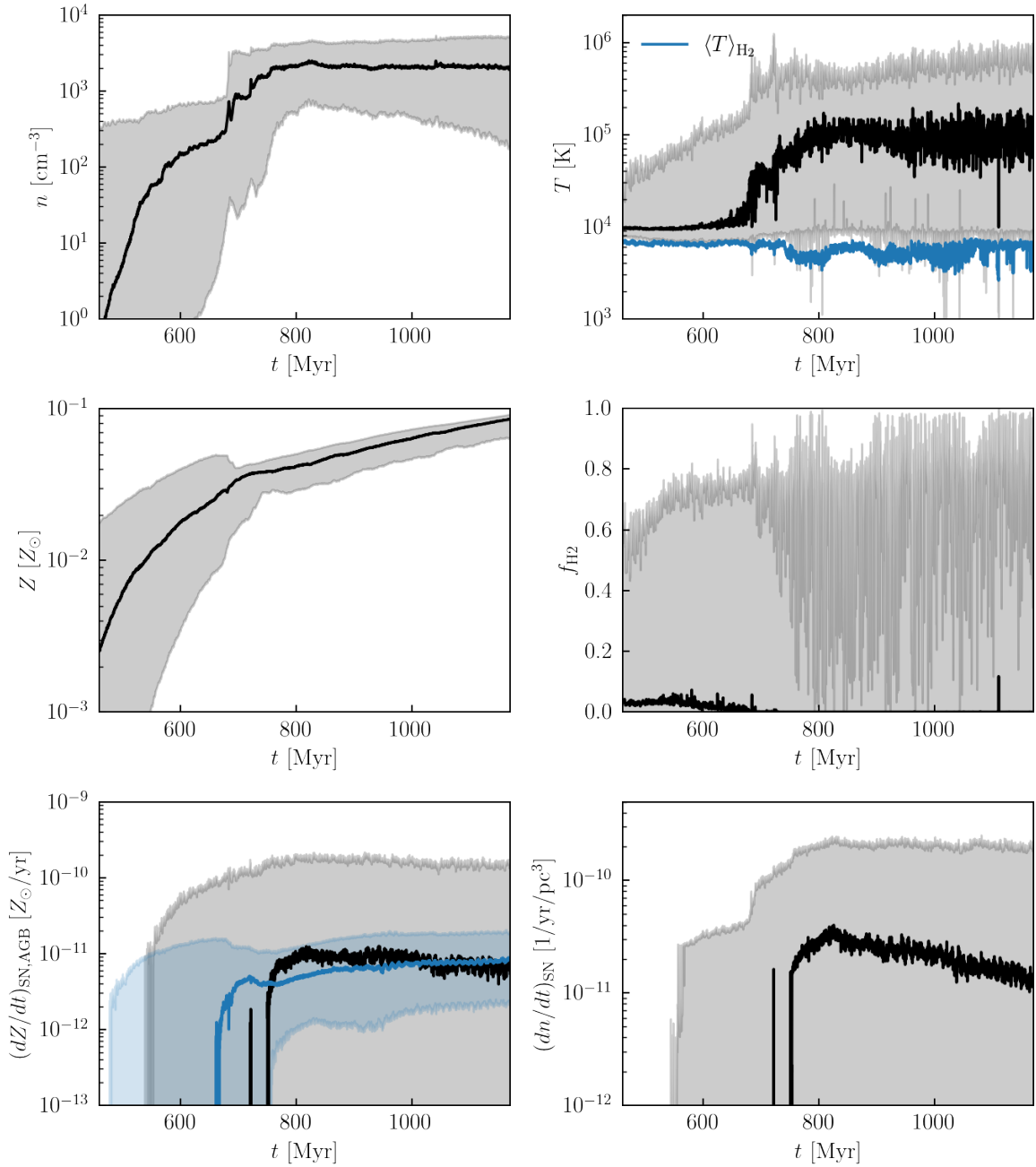


Figure 2.4: Tracer Histories. Solid black lines indicate median tracer quantities as a function of cosmological time. Shaded regions bound the 16th and 84th percentile tracer quantities. The top right panel additionally shows the molecular-fraction weighted average tracer temperature $\langle T \rangle_{\text{H}_2}$ in blue. The bottom left panel shows the metallicity production rates due to AGB stars in blue.

Cold ($T < 100\text{K}$), Warm Neutral Medium (WNM: $100\text{K} < T < 5000\text{K}$), Warm Ionized Medium (WIM: $5000\text{K} < T < 10^{5.5}\text{K}$ and Hot Ionized Medium (HIM: $T > 10^{5.5}\text{K}$). The consistent with Figure 2.2, the mass fractions of the WIM and HIM are large (and the Cold and WNM are therefore small) compared to typical values expected from observations of the Milky Way [Draine, 2011].

There is no a priori reason to expect galaxies located in Milky-Way mass halos at $z \gtrsim 6$ to have the ISM closely resembling the Milky Way one, and the mass fractions in various ISM phases in high redshift galaxies are not known. However, we are also aware that the CROC adopted stellar feedback recipe based on the delayed cooling algorithm results in model galaxies that do not match observations [Zhu et al., 2020]. Hence, we are unable to demonstrate that the ISM structure in our model galaxies is correct. It is likely, therefore, that the high mass fraction of HIM is a numerical artifact from the inadequate stellar feedback recipe.

Furthermore, the blue line on the temperature panel of Figure 2.4 shows the molecular-fraction-weighted temperature of ISM tracers in the last few hundred million years of the simulation. The average temperature of molecular gas is predicted to be unrealistically high, $\sim 4000 - 6000\text{K}$. This is fully expected, as the temperature distribution of the ISM in this simulated galaxy is not sufficiently resolved with the mere 100pc resolution to be physically realistic. Consequently, in the default dust model, we do not use the local ISM temperature in the simulation to calculate dust growth and destruction rates. For the growth rate, which has a $\propto \sqrt{T}$ dependence (see Eq. 2.5), we assume a constant $T = T_{\text{cold}} = 50\text{K}$ by default. For destruction, we calculate the rate based only on the assumption of a fixed dust mass destroyed per each (unresolved) supernova remnant, i.e. $D_{\text{dest}} = D_{\text{SNR}}$, which is independent of temperature (see Eq. 2.5). As we show in the next section, calculating the destruction rate based on thermal sputtering (which depends on the local temperature) dramatically over-predicts the dust destruction rate, even when the growth rate also uses the

local temperature instead of some fixed T_{cold} . It will be interesting in the future to apply a model like this to higher resolution simulations which more realistically capture the local temperature distribution of the ISM and compare the destruction rates predicted by thermal sputtering compared to the unresolved SNR prescription we use here.

2.2.2 *Pathline Sampling: Monte-Carlo Tracers*

As we detail in the next section, our dust model requires the assumption of several free parameters that quantify uncertainties in the physical processes that regulate dust evolution in the ISM. Since first-principles physics and observations generally do not constrain these parameters more tightly than within a few orders-of-magnitude, and the processes dependent on these parameters may interact in a complicated manner, it is necessary to explore a range of parameter values. Doing so would be prohibitively costly if each parameter combination required re-running the entire cosmological fluid-dynamical galaxy formation simulation. Therefore, when running the simulation we produce $\approx 10^4$ pathlines that sample the evolution of the simulated galaxy in an approximately Lagrangian manner. We can then post-process the simulation by integrating our dust model along each of these pathlines for as many different versions of the model that we want to explore without re-running the simulation. This dramatically reduces the computational cost and consequently greatly expands the size of the parameter grid we are able to explore. However, it also precludes an accounting for the possible dynamical effects of dust in the galaxy formation simulation by design. We discuss this issue further in Section 2.4.1.

To calculate the pathlines, we use the Monte Carlo (hereafter MC) tracer method introduced in Genel et al. [2013] and implemented in ART as described in Semenov et al. [2018], to which we refer the reader for details. The tracer particles are initialized to randomly and uniformly sample the Lagrangian region for the dark matter halo of interest. Tracer particle positions are output at ~ 5000 snapshots for an average interval of 0.2 Myr between each. At

every snapshot, the tracers samples the local gas number density n , temperature T , metallicity Z , neutral hydrogen fraction f_{HI} , molecular hydrogen fraction f_{H_2} , the metal production rate from supernovae (SN) \dot{Z}_{SN} , the metal production from asymptotic giant branch (AGB) stars \dot{Z}_{AGB} , and the rate density of supernovae \dot{n}_{SN} . The quantities \dot{Z}_{SN} , \dot{Z}_{AGB} , and \dot{n}_{SN} are assigned from the stellar particles cells using Nearest Grid Point (NGP) interpolation. This makes the sampled quantities somewhat more noisy and avoids extra smoothing, but the MC tracers are already noisy by construction. Note that each metallicity production rate is calculated as

$$\dot{Z}_{\text{process}} = \frac{1}{\rho} \left(\frac{d\rho Z}{dt} \right)_{\text{process}} \quad (2.1)$$

where ρ is the local gas density and $\left(\frac{d\rho Z}{dt} \right)_{\text{process}}$ is the change in the local density of metals due to the relevant production process.

This MC method ensures that the tracers used to sample pathlines statistically reproduce the density distribution of the simulation by being probabilistically exchanged between the cells used to discretize the fluid dynamics equations. The probabilistic nature of their exchange between cells prevents the pathlines from being strictly Lagrangian, and introduces some noise in their sampling of the fluid flow.

However, this is preferable to the severe biases introduced with the alternative “velocity tracer” method [implemented in ART as described in Semenov et al., 2017], wherein tracers are evolved by directly integrating their motion by sampling an interpolated velocity field of the simulation. While this algorithm produces smoother pathlines, its bias is so severe that by the end of the simulation, *all* 10^4 tracers are located at the same position in the simulation – the center of the simulated galaxy. In contrast the MC tracers sample the full density distribution in the ISM of the galaxy *by design* throughout the entire duration of the simulation. This is consistent with the issues identified in Genel et al. [2013], and thus MC tracers are the only viable method for sampling pathlines in our simulation, implemented in

Table 2.1: Model Parameters

Model Parameters	Description	Default (Values Explored)
Production, \dot{D}_{prod}		
$y_{D,\text{SN}}$	Yield (as a fraction of Z) from Supernovae	0.1 (0 – 0.4)
$y_{D,\text{AGB}}$	Yield (as a fraction of Z) from AGB	0.1 (10^{-2} – 0.4)
Gas-Phase Accretion, \dot{D}_{accr}		
C_{accr}	Clumping/Uncertainty Factor	1 (0 – 10)
τ_{accr}	Growth Timescale	3×10^8 yr
f^{dep}	“Depletable” Metal Fraction	0.7 (0.4 – 1)
f_{cold}	Sub-grid cold gas fraction	f_{H_2} ($f_{\text{HI}}, 1$)
T_{cold}	Assumed Temperature of Cold ISM	50 K (Direct from Simulation).
Destruction: SNR, $\dot{D}_{\text{dest}} = \dot{D}_{\text{SNR}}$		
C_{dest}	Destruction Efficiency/Uncertainty Factor	1 (0 – 10)
M_{SNR}	ISM Mass Swept-Up by Each Supernova Remnant	$1000M_{\odot}$
Destruction: Thermal Sputtering, $\dot{D}_{\text{dest}} = \dot{D}_{\text{sput}}$		
C_{sput}	Uncertainty Factor	0 (0.1-1)
τ_{sput}	Destruction Timescale at $T = 10^6\text{K}$	3×10^{-2} Myr
ω	Temperature Dependence Coefficient	3

the ART code as described in Semenov et al. [2018].

Figure 2.4 shows the median value (solid line) and 16th to 84th percentile range (shaded region) for all tracer properties as a function of time.

2.2.3 Dust Model: Physics – Creation and Destruction Processes

Along each pathline we integrate an ordinary differential equation describing the evolution of the dust-to-gas ratio D :

$$\frac{dD}{dt} = \dot{D}_{\text{model}} = \dot{D}_{\text{prod}} + \dot{D}_{\text{accr}} + \dot{D}_{\text{dest}} \quad (2.2)$$

where each term accounts for a different physical process: \dot{D}_{prod} for production by stellar evolution processes, \dot{D}_{accr} for accretion of gas-phase metals onto dust, and \dot{D}_{dest} for destruction processes that dissociate grains and return metals to the gas phase. We explain how each are calculated in our model in the subsections below. Table 2.1 summarizes all of the free parameters in this model, their default values, and the range of each explored in this analysis.

Dust Production in Evolved Stars and Supernovae

$\dot{D}_{\text{prod}} = \dot{D}_{\text{SN}} + \dot{D}_{\text{AGB}}$ accounts for the production of dust, which we assume to come from AGB star outflows and SN ejecta. Note that by “production” we refer exclusively to the formation of grains in these comparatively dense stellar remnant environments, as distinct from “growth by accretion” in the ambient ISM which we describe in the next section (i.e. we assume dust grains do not nucleate from the gas phase in the ambient ISM). We parameterize each of these as constant fractions y_D of the total metal yields from these processes, so that

$$\dot{D}_{\text{SN}}(\dot{Z}_{\text{SN}}|y_{D,\text{SN}}) = y_{D,\text{SN}}\dot{Z}_{\text{SN}} \quad (2.3)$$

$$\dot{D}_{\text{AGB}}(\dot{Z}_{\text{AGB}}|y_{D,\text{AGB}}) = y_{D,\text{AGB}}\dot{Z}_{\text{AGB}} \quad (2.4)$$

where we differentiate between dynamical quantities sampled from the simulation and assumed parameters.

The complexity of dust grain nucleation and growth in both AGB winds and SN ejecta remnants is still lacking a complete first-principles theoretical description – see Höfner and Olofsson [2018] for AGB dust formation, Sarangi et al. [2018] and Micelotta et al. [2018] for SN dust formation. Observational constraints on the total mass of dust produced by AGB stars exist [Lagadec et al., 2008, Srinivasan et al., 2009, Matsuura et al., 2009, Riebel et al., 2012, Nanni et al., 2019], but the dust-to-metal ratio of these outflows is difficult to measure. Large amounts of dust have been observed in SNRs [Dunne et al., 2003, Gomez et al., 2012, De Looze et al., 2017, Matsuura et al., 2011], but the fraction that survives sputtering after being engulfed by the reverse shock is uncertain. Consequently, neither theoretical nor observational constraints on $y_{D,\text{AGB}/\text{SN}}$ are particularly robust, and we treat these both as free parameters.

Some previous efforts to model dust in galaxy simulations [e.g. McKinnon et al., 2016,

Li et al., 2019b] have used the prescription from Dwek [1998] for the production of dust due to AGB and SN, to some success. To obtain an order-of-magnitude estimate for y_D , using equations 22-24 of Dwek [1998], adopting the condensation efficiencies from Li et al. [2019b] (based on Ferrarotti and Gail [2006] for AGB, Bianchi and Schneider [2007a] for SN), and taking protosolar elemental abundances [Asplund et al., 2009, Draine, 2011] gives $y_{D,AGB} \approx 0.07$ and $y_{D,SN} \approx 0.08$. So for default values we take $y_{D,AGB} = y_{D,SN} = 0.1$, and systematically vary both between 10^{-2} and 0.4. We note that, unlike the Dwek [1998] prescription, we do not adjust yields based on the metallicities of stellar populations, since we are not following the abundances of individual elements.

We note that this limitation prevents us from choosing more realistic yields based on expected elemental ratios; several previous investigations [e.g. Zhukovska et al., 2008, Gjergo et al., 2018, Granato et al., 2021, Parente et al., 2022, Choban et al., 2022] have utilized the expectation that silicate dust is composed mainly of MgFeSiO_4 molecules to fix Mg:Fe:Si:O number ratios to 1:1:1:4, thus limiting the total dust mass that can be produced. This further motivates the systematic exploration of a wide range of y_D values done in Section 2.3.1.

Growth via Gas-Phase Accretion

\dot{D}_{accr} accounts for dust growth in the ISM due to the accretion of metals onto grains from the gas phase. Kinetic considerations [see Draine, 1990, Dwek, 1998, Weingartner and Draine, 1999] suggest that this rate has the functional form [Feldmann, 2015]

$$\dot{D}_{\text{accr}}(D, Z, n, T, f_{\text{cold}} | C_{\text{accr}}, \tau_{\text{accr}}, f^{\text{dep}}) = \frac{C_{\text{accr}}}{\tau_{\text{accr}}} f_{\text{cold}} \left(\frac{n}{\text{cm}^{-3}} \right) \left(\frac{T}{\text{K}} \right)^{1/2} D (f^{\text{dep}} Z - D) \quad (2.5)$$

where C_{accr} is a free parameter to account for uncertainties in the dust clumping on scales

unresolved in the simulations, τ_{accr} is the characteristic timescale, f_{cold} is the fraction of cold gas in which accretion can occur, and f^{dep} is the fraction of metals that can be depleted onto dust grains. Since both τ_{accr} , f^{dep} depend upon the average dust grain cross section for each gas phase element that can potentially accrete, and are therefore likely dependent on the detailed composition and geometry of the dust grain population, any theoretical estimate of their values is extremely uncertain. However, Feldmann [2015] showed that the scaling of the galactic dust-to-gas ratio with metallicity depends sensitively on the quantity $t_{\text{dep,H}_2}/t_{\text{ISM}}$, where $t_{\text{dep,H}_2}$ is the molecular depletion timescale and t_{ISM} is their characteristic dust accretion timescale. Using equilibrium and dynamical one-zone models of galactic chemical and dust evolution compared to observations of local galaxies, they constrained $t_{\text{ISM}} \approx 4 \times 10^4 \text{yr}$, and $f^{\text{dep}} \approx 0.7$. Their characteristic timescale can be related to ours as

$$\tau_{\text{acc}} = t_{\text{ISM}} \left\langle \left(\frac{n_{\text{cold}}}{\text{cm}^{-3}} \right) \left(\frac{T_{\text{cold}}}{\text{K}} \right)^{1/2} \right\rangle \quad (2.6)$$

where n_{cold} , T_{cold} are the galaxy-averaged density and temperature of the cool ISM in which grain growth takes place, respectively. These factors are included here since the Feldmann [2015] one-zone modeling did not explicitly account for the density and temperature structure of the ISM in their calculations. Assuming growth takes place in the cold molecular phase [e.g. Zhukovska et al., 2016] lets us estimate $\langle n_{\text{cold}} \rangle \approx 10^3 \text{cm}^{-3}$ and $\langle T_{\text{cold}} \rangle \approx 50 \text{K}$ [Draine, 2011]. We therefore adopt as our default value $\tau_{\text{acc}} = 3 \times 10^8 \text{yr}$ with $C_{\text{acc}} = 1$. Since this constraint was obtained from galaxy-averaged one-zone models compared only to local-universe observations, it is likely very uncertain, especially in our application to the predictions of high- z galaxies. To explore the effects of this uncertainty, we vary the clumping factor C_{acc} from 0 to 10. We adopt $f^{\text{dep}} = 0.7$ as in Feldmann [2015] for our default value, and vary from 0.4 to 1.

There are two more uncertainties in the calculation of Eq. 2.5, both due to the inability of the simulation to resolve the thermodynamic phase structure of the ISM: the appropriate

values for T and f_{cold} . The 100 pc minimum cell size of the simulation means that the resolution of the ISM phases will be marginal at best, and the use of a delayed cooling feedback model risks over-predicting the temperature of the high-density gas. As we show in 2.2.1, the phase structure of the ISM is likely not well resolved in this simulation. Therefore, naively using the simulation temperature for Eq. 2.5 would grossly over-predict the ISM growth rate. Consequently, by default we assume $T = T_{\text{cold}} = 50\text{K}$ for Eq. 2.5 only, but we also present the predictions of the model when the full simulation temperature is used. Since this unresolved cold phase represents a subset of the total gas in each cell, we must also multiply by the mass fraction of cold gas f_{cold} . We can estimate the value of this additional free parameter by equating it to either the neutral fraction f_{HI} which is calculated self-consistently from the radiation field, density, and temperature of the ISM in the simulations, or the molecular fraction f_{H_2} modeled with the Gnedin and Draine [2014] fitting functions. We use $f_{\text{cold}} = f_{\text{H}_2}$ from the simulation by default, since this is the same cold fraction assumed by the star formation prescription of the simulation. However, we also explore the predictions for $f_{\text{cold}} = f_{\text{HI}}$.

Destruction Processes

\dot{D}_{dest} is the rate at which dust is destroyed by energetic processes in the ISM. The most important of these is likely thermal sputtering in high temperature gas – the erosion of dust grains due to thermal collisions with high-temperature gas particles. The timescale for the erosion of graphite, silicate, and iron grains of size a due to thermal sputtering is given by [Draine, 2011, Eq. 25.14]

$$\frac{da}{dt} = -10^{-6} \mu\text{m yr}^{-1} \left[1 + \left(\frac{T}{10^6\text{K}} \right)^{-3} \right] \left(\frac{n_{\text{H}}}{\text{cm}^{-3}} \right) \quad (2.7)$$

which we can convert to change in dust-to-gas ratio (assuming a single size for all grains) as

$$\frac{dD}{dt} = \frac{3}{a} D \frac{da}{dt} \quad (2.8)$$

giving

$$\dot{D}_{\text{sput}}(D, n, T | C_{\text{sput}}, \tau_{\text{sput}}, \omega) = -\frac{C_{\text{sput}}}{\tau_{\text{sput}}} \frac{1}{1 + (T/10^6\text{K})^{-\omega}} \left(\frac{n}{\text{cm}^{-3}}\right) D \quad (2.9)$$

where C_{sput} is a free parameter of default value unity we systematically vary to account for uncertainties, $\tau_{\text{sput}} \approx 3 \times 10^5 \text{yr} (a/\mu\text{m})$ is the characteristic timescale for dust destruction due to sputtering in high temperature gas, and $\omega \approx 3$ parameterizes the temperature dependence of the sputtering rate for $T \ll 10^6\text{K}$. Adopting $a_{\text{eff}} = 0.1\mu\text{m}$ [Draine, 2011], we take $\tau_{\text{sput}} = 3 \times 10^4 \text{yr}$ and $\omega = 3$ as our default values. Simulations of galaxy clusters with a physical dust model [Gjergo et al., 2018, Vogelsberger et al., 2019] suggest this timescale should be increased by a factor as large as 10, which we also explore.

If the temperature and density distribution of the ISM were fully resolved in our simulations, thermal sputtering alone would provide a good estimate of the grain destruction rate. However, since the delayed cooling feedback model likely over-predicts the temperature of the densest ISM gas at the simulation resolution of $\sim 100\text{pc}$, Eq 2.9 with quantities from the simulation likely grossly over-predicts the destruction rate in the ISM.

To correct for this, an alternative method of calculating the destruction rate is tied directly to the local rate of supernovae, which are assumed to be responsible for all of the $\sim 10^6\text{K}$ gas in the ISM where sputtering is most efficient. Let M_{SNR} be the amount of ISM mass swept up by an individual SNR, and C_{dest} be the average efficiency with which grains are destroyed in each SNR. Then the rate of change in dust-to-gas ratio is given by

$$\dot{D}_{\text{SNR}}(D, n, \dot{n}_{\text{SN}} | C_{\text{dest}} M_{\text{SNR}}) = C_{\text{dest}} M_{\text{SNR}} D \frac{\dot{n}_{\text{SN}}}{\rho} \quad (2.10)$$

where \dot{n}_{SN} is the local volumetric rate of supernova explosions and ρ is the gas density.

McKee [1989] estimate $M_{\text{SNR}} \approx 1000M_{\odot}$, which we adopt for our fiducial value. C_{dest} is a free parameter with a fiducial value of unity that we vary to explore the impact of uncertainties in this rate due to both the uncertain destruction efficiency and M_{SNR} .

We note that this prescription ignores destruction due to sputtering in hot gas that is not spatially coincident and directly associated with supernova explosions – i.e. gas in the hot circum-galactic medium (CGM). We expect this is not a major issue because galaxies at this mass are not expected to establish stable, hot circumgalactic media until $z \sim 2$ [Dekel and Birnboim, 2006], much later than the last snapshot of our simulation. However, this remains an uncertainty in our work that we will only be able to fully address with a more sophisticated treatment of feedback and explicitly coupled dust physics done on-the-fly in the simulation.

Moreover, Priestley et al. [2022] point out that this destruction efficiency likely varies with metallicity, since higher metallicity gas will cool more rapidly, thereby reducing the impact of sputtering in high-temperature gas. We defer the inclusion of such higher-order effects to more sophisticated modeling in the near future, but speculate that this is not likely to have a dramatic effect on our results since, as we show in Section 2.3.1, supernova destruction is a subdominant effect unless the destruction efficiency is enhanced by approximately an order-of-magnitude.

Since \dot{D}_{SNR} is not dependent on the local gas temperature, which is likely inaccurate in the simulation due to limited resolution, we adopt $\dot{D}_{\text{des}} = \dot{D}_{\text{SNR}}$ by default, but also explore predictions using $\dot{D}_{\text{des}} = \dot{D}_{\text{sput}}$.

2.2.4 *Dust Model: Numerical Integration*

For each tracer i and each snapshot j in the tracer data, we have the following quantities from the simulation: n_{ij} , T_{ij} , $f_{\text{HI},ij}$, $f_{\text{H}_2,ij}$, $\dot{Z}_{\text{SN},ij}$, $\dot{Z}_{\text{AGB},ij}$, $\dot{n}_{\text{SN},ij}$. For each tracer, we linearly interpolate each quantity X as a function of cosmological time to define a continuous

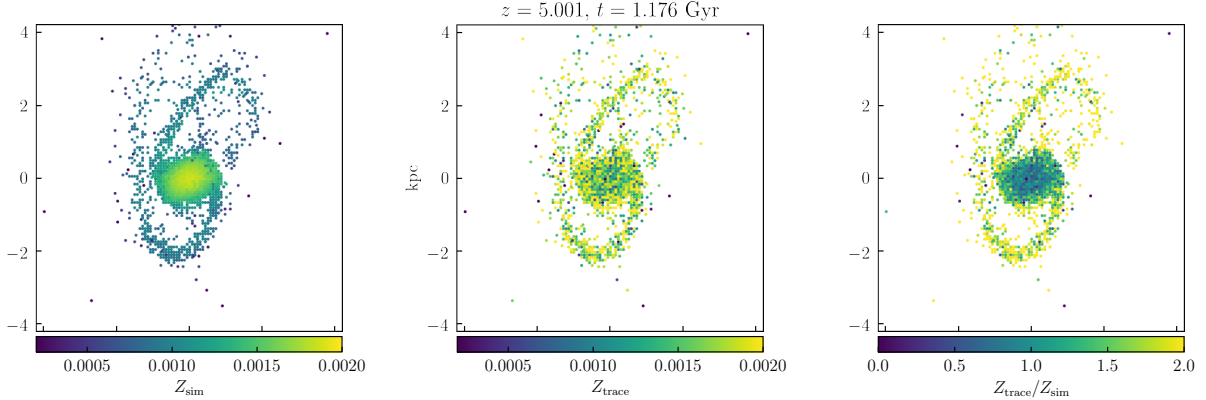


Figure 2.5: Maps of the simulation metallicity (left panel), tracer metallicity (defined by Eq. 2.11, middle panel), and their ratio (right panel) at the final snapshot of our simulation are shown. Values for tracers in the same cell are averaged. The statistical error in the tracer paths due to their probabilistic nature results in an approximately uniform tracer metallicity across the galactic disk, while the simulation metallicity displays a clear gradient.

function $X_i(t)$. This allows us to define a pair of coupled continuous ordinary differential equations for the metallicity and dust-to-gas ratio of each tracer:

$$\frac{dZ_i}{dt} = \dot{Z}_{\text{SN},i}(t) + \dot{Z}_{\text{AGB},i}(t) \quad (2.11)$$

$$\frac{dD_i}{dt} = \dot{D}_{\text{model}}[n_i(t), T_i(t), f_{\text{HI},i}(t), f_{\text{H}_2,i}(t), Z_i(t), \dot{Z}_{\text{SN},i}(t), \dot{Z}_{\text{AGB},i}(t), \dot{n}_{\text{SN},i}(t)]. \quad (2.12)$$

We use the `scipy` [Virtanen et al., 2020] module `solve_ivp` to perform this numerical integration. We have tested our solver against subsets of the model with analytically expressible solutions, all of which are recovered to fractional accuracy of $\lesssim 10^{-7}$ with the adopted solver parameters.

Note that Z_i is *not* generally identical to the metallicity in the simulation sampled by the tracer, call it $Z_{\text{sim},i}$, because of the imperfectly Lagrangian nature of the Monte Carlo tracers (see Section 2.2.2). Indeed, Figure 2.5 compares the spatial distribution of these two

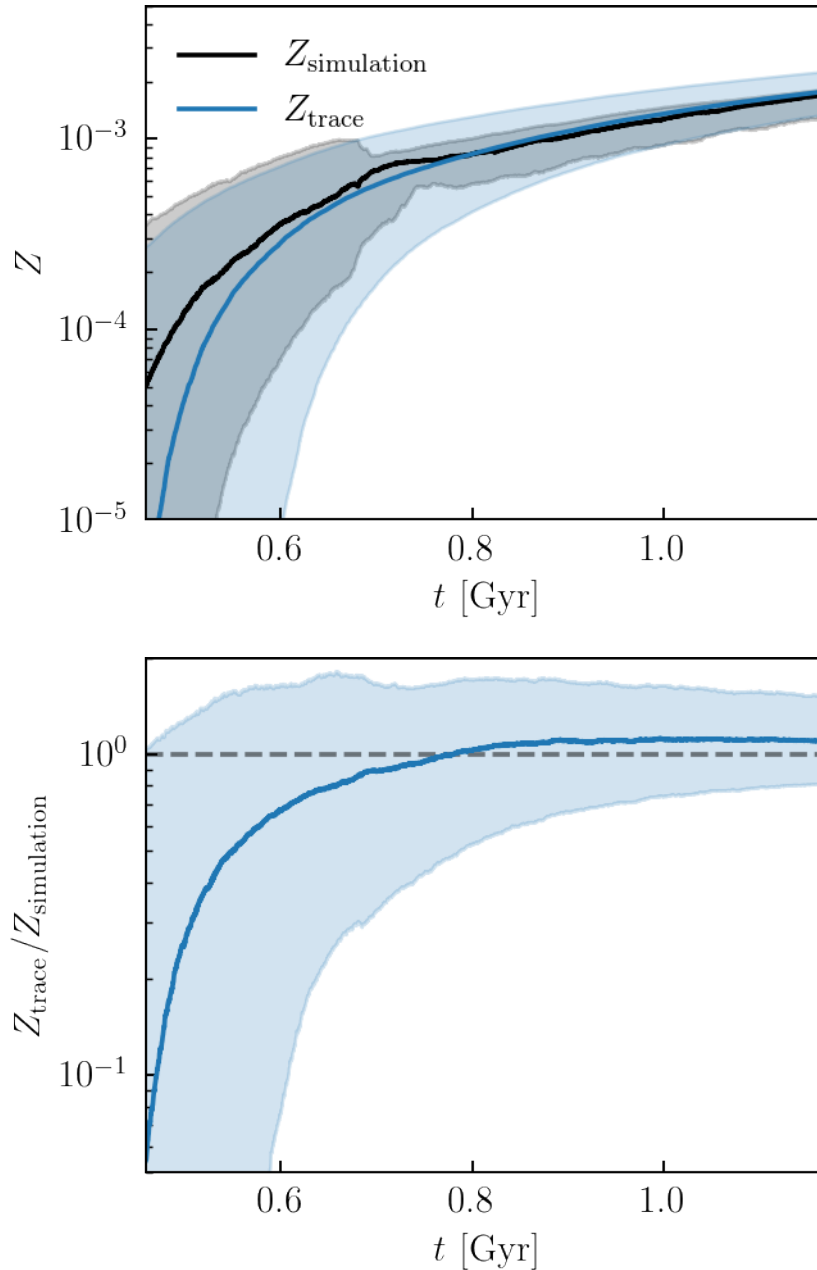


Figure 2.6: The top panel shows the evolution of both simulation (black) and tracer (blue) metallicity as a function of time in the simulation, while the bottom shows their ratio. The solid lines in the top panel show the median tracer value at each snapshot, while the shaded regions enclose the 16th and 84th percentiles. The bottom shows the same for their ratio. By $\sim 800\text{Myr}$, their ratio is close to unity, indicating that the tracer metallicity reflects the simulation metallicity in an average sense. Before that time, however, the tracer metallicity is biased low. We discuss the correction of this bias in Section 2.2.4.

quantities in the last snapshot of our simulation, at $z = 5$. While the simulation predicts a smooth radial gradient in the metallicity of the galaxy disk, the integrated production is both noisy and uniform across the disk due to the probabilistic nature of the tracers.

A more quantitative comparison is shown in Figure 2.6, where the median, 16th and 84th percentiles of these metallicities for all tracers at each time are compared. By the end of the simulation, their ratio is close to unity, indicating the tracers capture the global metal production history of the ISM in the galaxy, but due to sampling issues are biased low at times earlier than ~ 600 Myr. However, this effect can be corrected for: since the simulation metallicity *is* Lagrangian (because it is evolved with an advection solver in the simulation code), we can re-scale the dust-to-gas ratio of each tracer by the ratio of these metallicities. So, for any observable quantity that requires a dust fraction D_{obs} , this is calculated from the D predicted by our model as

$$D_{\text{obs}} = \left(\frac{D}{Z} \right)_{\text{tracer}} Z_{\text{sim}} \quad (2.13)$$

2.2.5 Correction of Star Formation Rates

Zhu et al. [2020] showed that the CROC simulations fail to reproduce the observed stellar mass-halo mass relationship. The stellar masses predicted by the simulations, and therefore star formation rates, are too low at a given halo mass compared to the observations. They provide an empirical formula that re-scales the simulated stellar masses to be consistent with observations:

$$\tilde{M}_\star = M_\star \left[1 + A_z(t) \log_{10} \left(1 + \frac{M_\star}{3 \times 10^8 M_\odot} \right) \right] \equiv M_\star f_{\text{corr}}(t) \quad (2.14)$$

where $A_z = 6, 10, 30$ at $z = 5, 6, 7$. We test the sensitivity of our dust model prediction to this inaccuracy in the simulation by appropriately re-scaling the metal production rates (\dot{Z}_{SN} , \dot{Z}_{AGB}) and supernova rates \dot{n}_{SN} by this same factor: $\dot{\tilde{Z}}_{\text{SN}} = f_{\text{corr}} \dot{Z}_{\text{SN}}$, $\dot{\tilde{Z}}_{\text{AGB}} = f_{\text{corr}} \dot{Z}_{\text{AGB}}$,

and $\dot{n}_{\text{SN}} = f_{\text{corr}} \dot{n}_{\text{SN}}$. Note that this requires re-scaling the simulation metallicity for the correction in Eq. 2.13. We interpolate f_{corr} to all simulation redshifts by fitting a second-order polynomial to A_z . Since the instantaneous metal production and supernova rates depend on the entire current stellar population, they depend on the full prior star formation history. Our correction is therefore a crude approximation. Moreover, substantially increased star formation would also remove additional gas from the galaxy ISM, thereby likely changing the density distribution in a complicated way we do not account for. Consequently, this correction should not be taken as a precise prediction, but rather as providing an estimate of the uncertainty in our predictions due to the inaccuracies in the simulation.

2.2.6 Calculation of Observable Quantities: M_D , β_{UV} , IRX , τ_{1500}

To compare our predictions to observational data, we calculate quantities of our simulated galaxy that depend on dust content and can in principle be measured observationally. These predictions require as input the spatial distribution of the dust mass, which we obtain as follows. For each simulation snapshot we extract a fixed resolution data cube centered on the simulated galaxy with dimensions of $L = 0.2R_{\text{vir}}$ on each side. The data cube has a resolution equivalent to the highest refinement level of the adaptive mesh, since this is the resolution of the ISM gas that contains almost all the dust. Each tracer particle is then identified with its corresponding cell. In order to adequately sample the gas distribution in the simulation, the simulation was run with sufficiently many tracers that most cells in the simulated galaxy ISM have multiple tracers. For each cell we calculate the dust-to-gas ratio as the average of all tracers in the same cell. We can then multiply this quantity by the cell metallicity and the cell mass to obtain the dust mass per cell.

The total dust mass is simply the sum of individual cell dust masses. While this is the most straightforward measure of the galactic dust content, it is difficult to measure the dust mass of high-redshift galaxies, as this relies on assumptions of the grain size distribution and

dust temperature. Consequently, we also forward-model several more directly observable quantities: the attenuated ultraviolet luminosity L_{UV} , the effective optical depth due to dust extinction in the ultraviolet (at $\lambda = 1500\text{\AA}$) τ_{1500} , the logarithmic slope of the galaxy spectrum in the ultraviolet β_{UV} , and the infrared luminosity due to dust thermal radiation L_{IR} and corresponding infrared excess $\text{IRX} \equiv L_{\text{IR}}/L_{\text{UV}}$.

The ultraviolet radiation from galaxies comes from young massive stars, but can be significantly attenuated by interstellar dust. This attenuation is wavelength-dependent such that the shape of the spectrum in this regime is sensitive to the dust column density. β_{UV} is calculated by least-squares fitting a power law of the form $f_\lambda \propto \lambda^\beta$ to the galaxy spectrum in the rest-frame wavelengths $1268 - 2580\text{\AA}$, using only the 10 wavelength windows listed in Table 2 of Calzetti et al. [1994] to avoid contamination from absorption lines. The galaxy spectrum is the combined spectra of each star particle, each of which represents a single-age, uniform-metallicity stellar population attenuated by a dust column density dependent on the observational viewing angle. The unattenuated spectrum of each star particle is calculated using the Flexible Stellar Population Synthesis code [Conroy and Gunn, 2010]. To sample the distribution of viewing angles, we calculate optical depths projected along the 3 coordinate axes in both directions (6 total), which should be random with respect to the galaxy orientation. Optical depths to each star particle as function of wavelength are estimated as

$$\tau_i(\lambda) = \kappa_D(\lambda) \int_i \rho_D dl \quad (2.15)$$

where $\kappa_D(\lambda)$ is the opacity (or mass absorption coefficient) *per unit dust mass*, ρ_D is the dust density, and $\int_i dl$ is the integral along a line-of-sight to a given star i . For $\kappa_D(\lambda)$ we use the ‘‘SMC bar’’ model of [Weingartner and Draine, 2001].¹

1. <https://www.astro.princeton.edu/~draine/dust/dust.html>, converted from a total mass to dust mass absorption coefficient with an assumed dust-to-gas mass ratio of $M_{\text{dust}}/M_{\text{gas}} = (M_{\text{dust}}/M_{\text{H}})/(M_{\text{gas}}/M_{\text{H}}) = 0.00206/1.36 = 0.00151$ from Table 3 of Draine et al. [2007].

Since we do not evolve the full dust-size distribution in our model, and empirical measurements of the dust opacity of high-redshift galaxies do not exist, the choice of dust opacity represents an additional uncertainty in our calculations. It is possible that the dust size distribution, and therefore opacities, is very different at these early cosmic epochs – for example, Granato et al. [2021] evolve two bins in dust size for simulated galaxies and find that the ratio of small to large dust grains increases by approximately a factor of two over the redshift range we consider. Nonetheless, we show that our results are not obviously in tension with the data (Section 2.3.2), suggesting that our adopted dust opacity is a reasonable first-guess. We plan to evaluate this effect by accounting for the dust grain size distribution in future work.

Dust grains are heated to temperatures $T \sim 10 - 100\text{K}$ by the interstellar radiation field, causing them to emit thermal radiation in the infrared. Assuming the ISM is optically thin to this radiation, the specific luminosity is given by

$$L_\lambda = 4\pi M_D \kappa_D(\lambda) B_\lambda(T) \quad (2.16)$$

where $\kappa_D(\lambda)$ is the dust opacity, $B_\lambda(T)$ is the specific intensity of black-body radiation. Since this quantity is dependent on the dust temperature, a fully self-consistent calculation would require solving for the dust temperature given the joint spatial distributions of dust and interstellar radiation. Since our simulations likely do not resolve this structure, a completely self-consistent calculation of this quantity is impossible. Consequently, we present results for several temperatures that span a plausible range: 20, 40, 60K. As in Bouwens et al. [2020], we define the total infrared luminosity as $L_{\text{IR}} = \int_{8\mu\text{m}}^{1000\mu\text{m}} L_\lambda d\lambda$, and estimate the UV luminosity as $L_{\text{UV}} = L_{1500\text{\AA}}$, to calculate the infrared excess as $\text{IRX} \equiv L_{\text{IR}}/L_{\text{UV}}$.

2.3 Results

2.3.1 Predictions of Dust Model: Dependence on Dust Model Parameters

Fig. 2.7 shows the resulting dust-to-metal ratio and rates of individual dust creation and destruction physical processes for our default parameter values. We see that the dust production is initially dominated by supernovae ejecta, in which case the dust-to-metal ratio is set by the assumed supernova yield $y_{D,\text{SN}}$. Note that the destruction rate due to supernova remnants is much lower than the production rate, so that D/Z never falls significantly below $y_{D,\text{SN}}$, indicated with the dashed black line in the top panel.

At approximately 700 Myr, accretion increases rapidly and dominates the dust evolution thereafter. Consequently, as metals in the ISM accrete onto dust grains, the dust-to-metal ratio now increases from $\sim y_{D,\text{SN}}$, reaching a value of approximately 0.5 by the end of the simulation at $z = 5$, $t = 1.18\text{Gyr}$. Note that this is less than the maximum of $D/Z = f^{\text{dep}} = 0.7$. Despite also increasing, the rate of supernova remnant destruction always remains subdominant to ISM accretion. The contribution of dust from AGB stars is always negligible because they produce heavy metals at a rate approximately two orders-of-magnitude less than supernovae.

Below we explore how these predictions change with model parameter values.

Production: $y_{D,\text{SN}}$ and $y_{D,\text{AGB}}$

Fig. 2.10 explores the effect of varying the production yield y_D on D/Z and the evolution of D as a function of Z . Note that we use this to indicate the value for both $y_{D,\text{SN}}$ and $y_{D,\text{AGB}}$, which we keep the same in this figure. As shown in Fig. 2.7, AGB wind production is largely negligible at these redshifts because it produces far fewer metals, so these results are unchanged for any physically reasonable variations in $y_{D,\text{SN}}/y_{D,\text{AGB}}$ around 1. Values of $y_D = 0.01$ and $y_D = 0.4$ are compared with the default $y_D = 0.1$. In each case the value

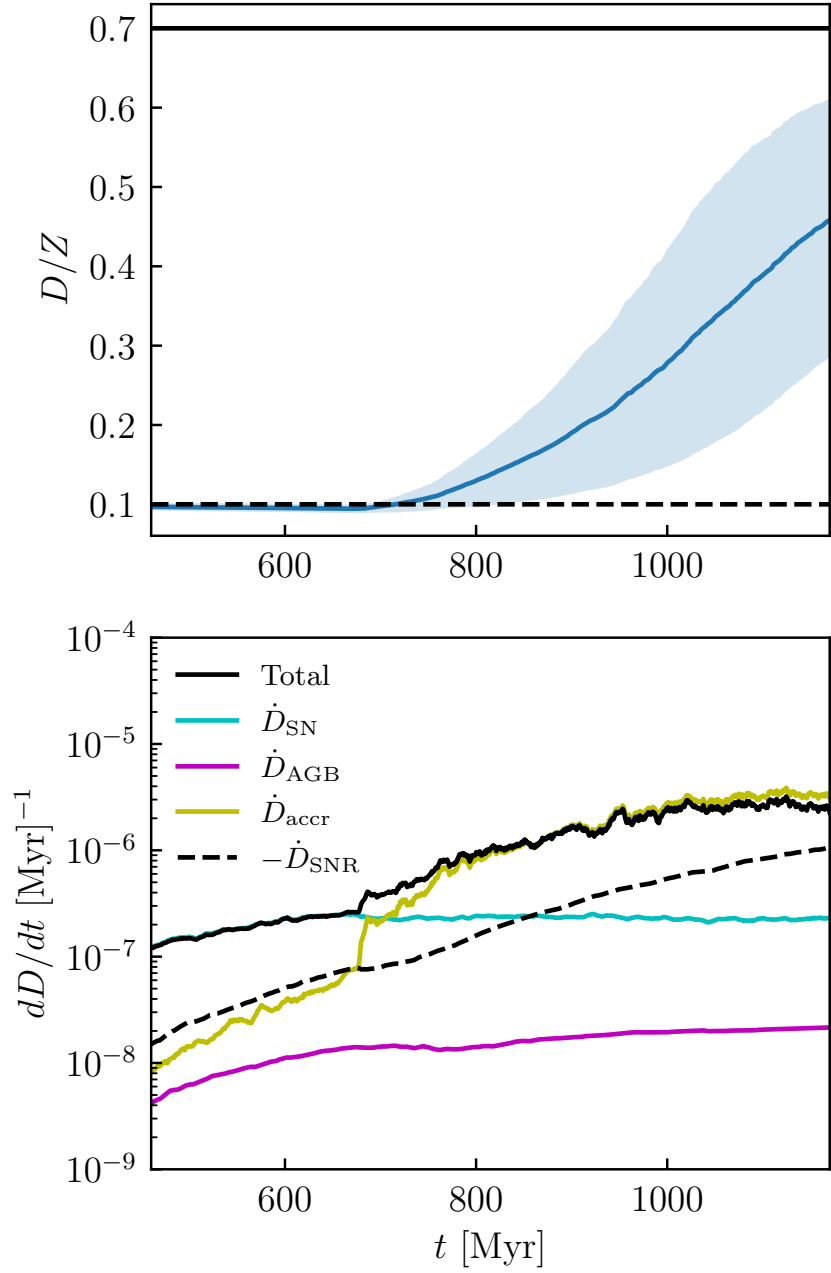


Figure 2.7: Dust-to-metal ratios (top panel) and the contributions of each process to dust growth with default parameters (bottom panel). Solid lines show mean values for all tracers, and the shaded region on the top panel bounds the 16th and 84th percentiles at each timestep. On the top panel, the solid black line shows f^{dep} and the dashed black line shows $y_{D,\text{SN}} = y_{D,\text{AGB}}$. The rapid variation in simulated ISM quantities sampled by the tracers (as shown in Figure 2.4) result in rapid variation of these rates, so for readability we have smoothed the lines on the bottom panel with a boxcar average of width 10 Myr.

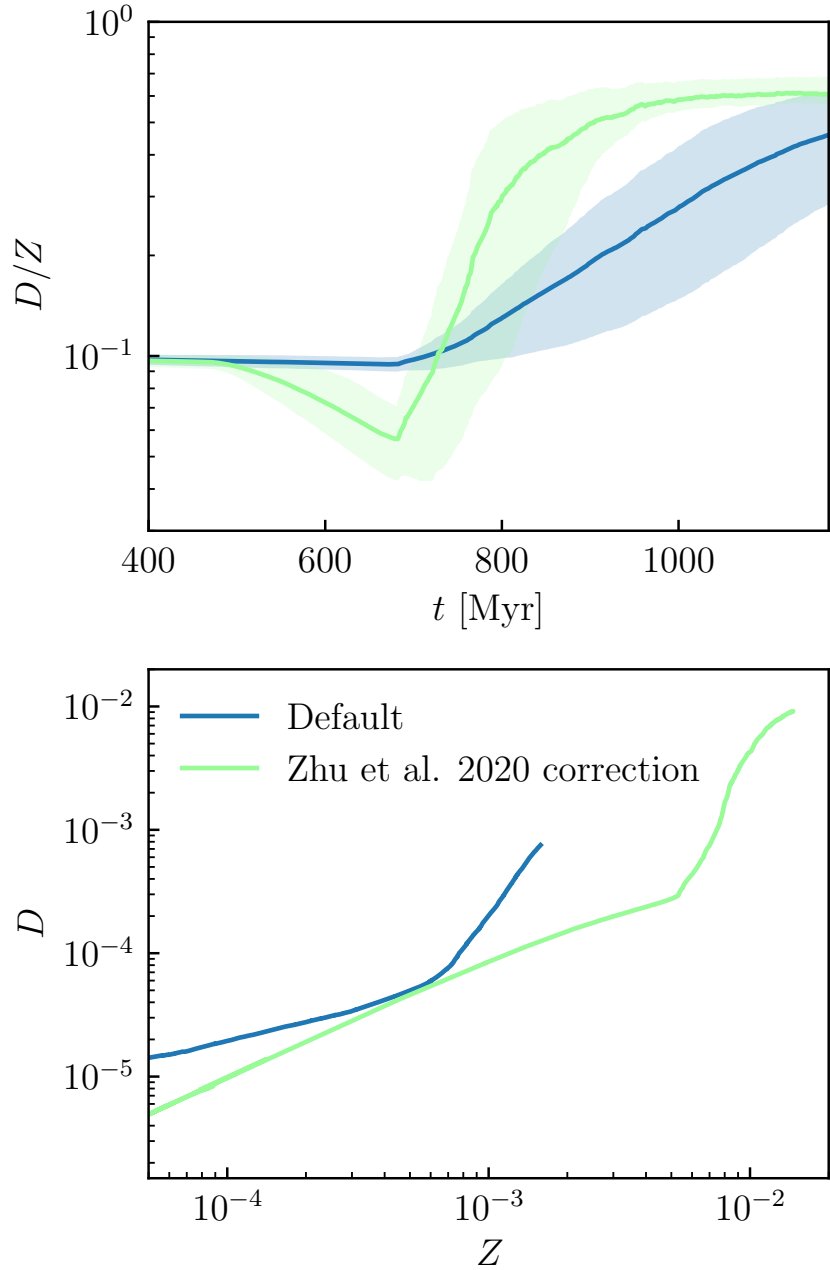


Figure 2.8: Effect of Zhu et al. [2020] correction for the SFR rate. D/Z is initially suppressed relative to the default value because of the increased destruction rate due to supernova remnants, but much more rapidly transitions to $\sim f^{\text{dep}}$ because of the enhanced ISM accretion rate due to higher metallicity.

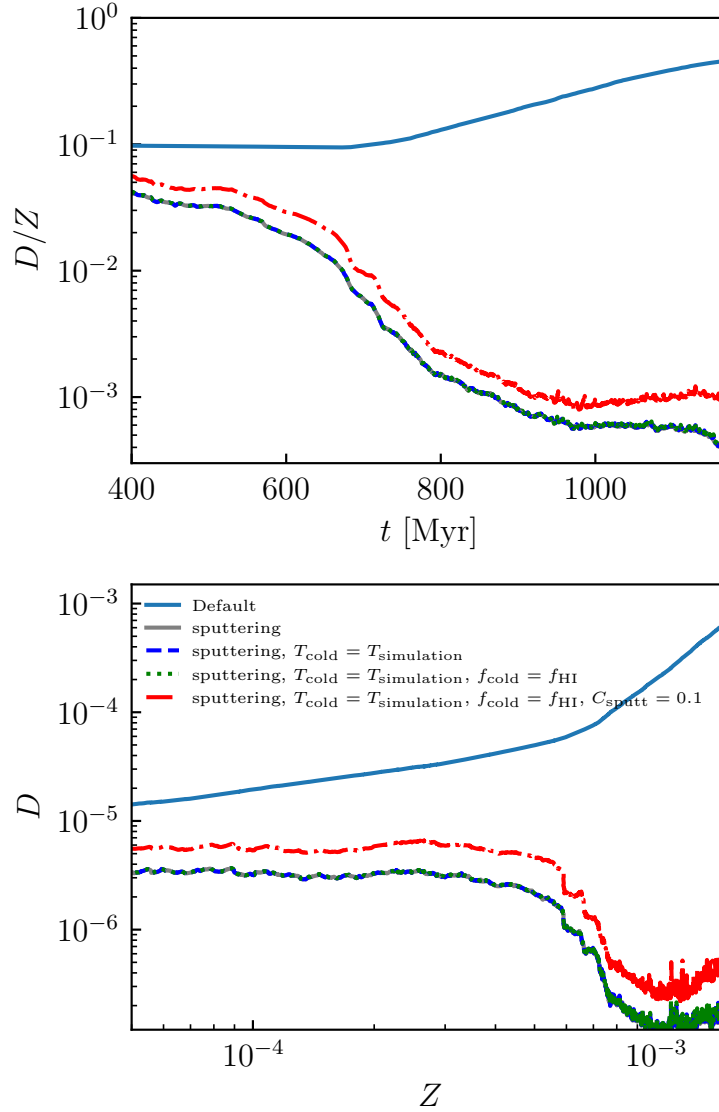


Figure 2.9: Effect of tying dust destruction rates to local ISM gas temperature. The grey line adopts sputtering destruction rates $\dot{D}_{\text{dest}} = \dot{D}_{\text{sputt}}$. This line is invisible because the dashed blue and dotted green lines – both attempts to increase the growth rate of the dust due to ISM accretion \dot{D}_{accr} (the former by setting the temperature of the cold gas in the accretion term to the simulation temperature, the latter by additionally setting the cold gas fraction to the neutral hydrogen fraction) – are visually indistinguishable. Thus no reasonable modification to the \dot{D}_{accr} overcomes the dominance of the thermal sputtering rate. This is true even if the sputtering is additionally decreased by a factor of 10, as shown with the red dot-dashed line.

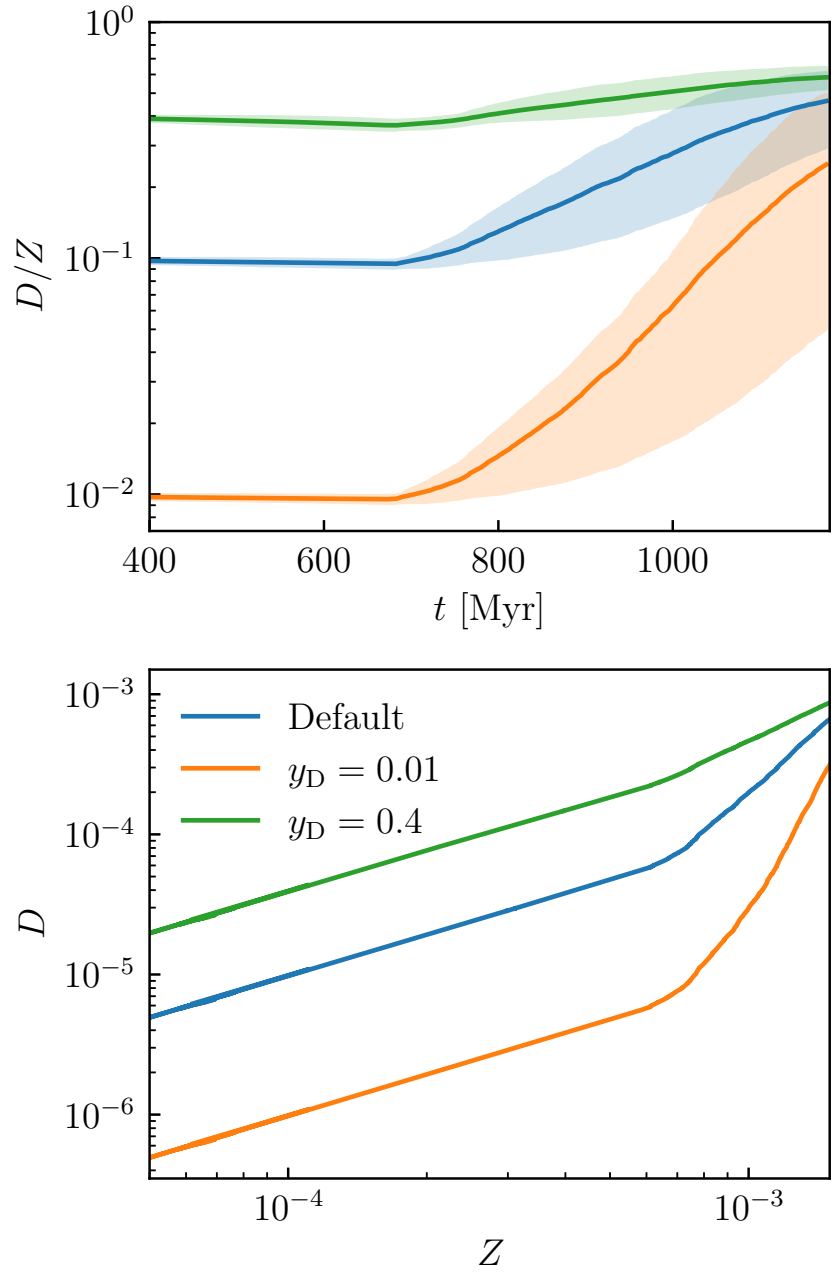


Figure 2.10: Effect of varying production yield $y_{D,\text{SN}} = y_{D,\text{AGB}} = y_D$ on dust evolution. Solid lines show mean values for all tracers, shaded regions encompass tracer 16th and 84th percentiles.

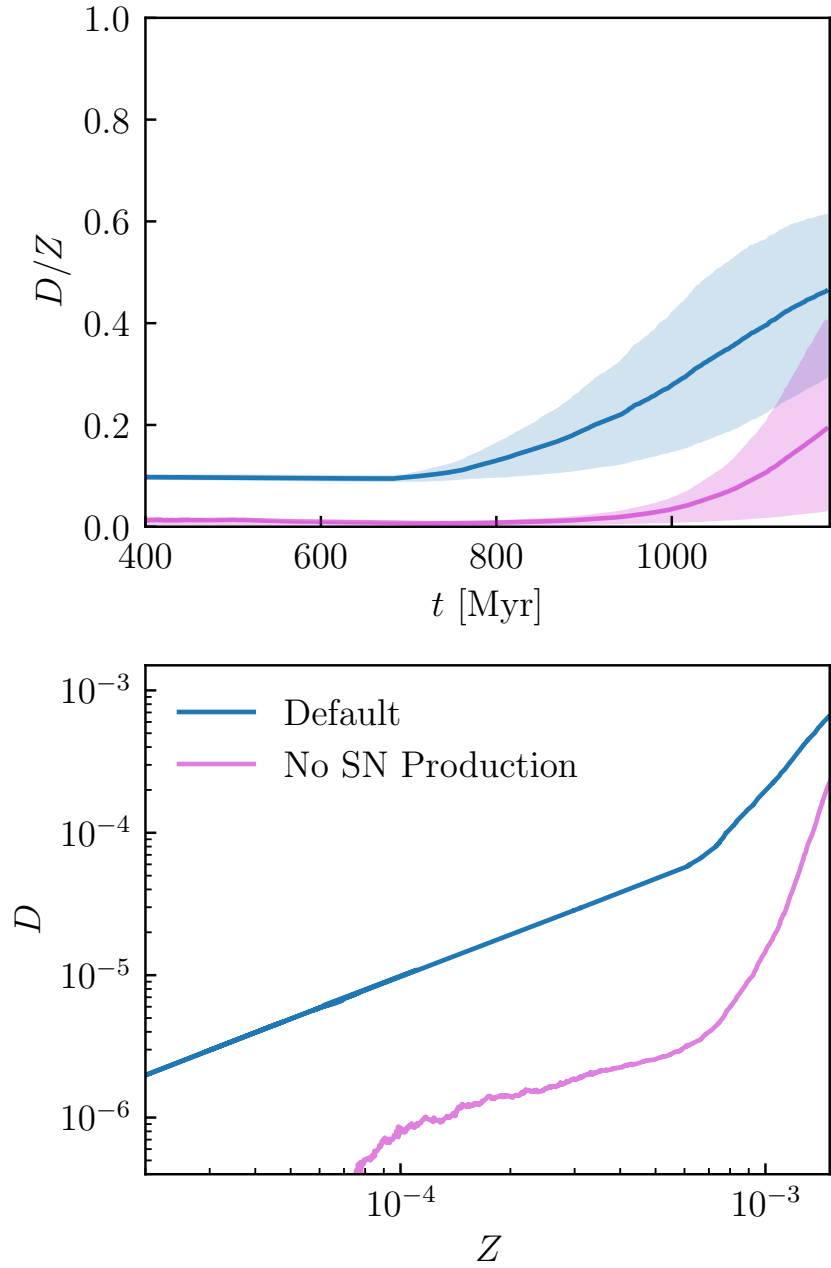


Figure 2.11: No SN dust production. The default value $y_{D,AGB} = 0.1$ is used in both cases, while the magenta lines show the predictions of the model when SN production is turned off completely $y_{D,SN} = 0$. Solid lines and shaded regions are defined in the same way as the previous figure.

of y_D entirely determines the dust-to-metal ratio prior to the onset of rapid accretion from the ISM. By setting the initial condition for this rapid accretion phase, y_D is positively correlated with the final D/Z ratio. However, note that the rapid accretion phase begins at exactly the same time, and therefore same metallicity, in each model. This is consistent with the finding of [Feldmann, 2015] that accretion becomes efficient at a critical metallicity which is independent of the production yield. Finally, note that because the supernova remnant destruction rate is $\propto D$ (eq. 2.10), destruction (with default parameters) remains unimportant even when the production yield is very small, and the D/Z ratio never goes significantly below y_D .

Fig. 2.11 shows the predicted dust content in the absence of dust production by supernovae, i.e. dust is assumed to be produced only from AGB star winds. While young local supernova remnants are observed to efficiently form dust, it remains an open question how much of this dust survives the reverse shock, motivating this parameter choice as an extreme scenario in which supernovae do not produce any dust grains. This figure shows that even with reasonable assumed AGB wind dust yield (10%) and ISM growth timescale, AGB production *alone* produces enough dust to allow efficient accretion of gas phase metals at late times in our simulations, resulting in $D/Z \sim 0.2$ by $z = 5$.

Gas-Phase Accretion: C_{accr} , T_{cold} , and f^{dep}

Figures 2.14 and 2.13 explore the effect of changes to gas-phase accretion parameters. Since $\dot{D}_{\text{accr}} \propto C_{\text{accr}} T_{\text{cold}}^{1/2}$ (eq. 2.5), we show various choices for both in Fig. 2.14. Fig. 2.13 explores variations in the maximum metal depletion fraction f^{dep} .

Fig. 2.14 shows three modifications to the accretion prescription in the default model: accretion turned off entirely $C_{\text{accr}} = 0$, accretion enhanced by an order-of-magnitude $C_{\text{accr}} = 10$, and setting the temperature of the “cold” phase in which accretion takes place to the local gas temperature of the simulation $T_{\text{cold}} = T_{\text{simulation}}$ (as opposed to assuming the

constant value of $T_{\text{cold}} = 50\text{K}$ as is our default). In the complete absence of ISM accretion, destruction due to supernova remnants is able to reduce the dust-to-metal ratio by $\sim 30\%$ compared to the production yield. Conversely, an order-of-magnitude enhancement in the accretion rate causes the dust mass to grow rapidly at earlier times and lower metallicities, saturating at $D/Z \approx f^{\text{dep}}$ well before the end of the simulation at $z = 5$.

We see that changing T_{cold} from a constant value of 50K to the gas temperature in the simulation sampled by each tracer has a similar but even slightly greater effect. Note that since we adopt $f_{\text{cold}} = f_{\text{H}_2}$, this is effectively the average temperature of the molecular phase predicted by the simulation. As shown in Fig. 2.4, the molecular-fraction-weighted average temperatures are $\gtrsim 5000$, and the accretion rate depends on the square-root of the ambient gas temperature, so $\sqrt{\langle T_{\text{H}_2} \rangle / 50\text{K}} \gtrsim 10$ is the expected enhancement. In this way the assumed average temperature of the cold phase is degenerate with the assumed timescale for grain growth due to gas-phase accretion, as long as T_{cold} does not exhibit any broad, significant trends on timescales of gigayears, as is the case even when we take the simulation value.

Destruction due to Thermal Sputtering: Local Supernova Rate or Gas Temperature

Figures 2.12 and 2.9 explore physics prescriptions and parameter choices related to the destruction rate of dust in the hot phase of the ISM due to thermal sputtering. Fig. 2.12 shows the predictions of the dust model assuming $\dot{D}_{\text{dest}} = \dot{D}_{\text{SNR}}$, which is our default. We display predictions for extreme variations in the efficiency of supernova remnant destruction – one where the destruction is turned off entirely ($C_{\text{dest}} = 0$) and another where it is enhanced by an order-of-magnitude $C_{\text{dest}} = 10$. The $C_{\text{dest}} = 0$ case corroborates the conclusion of Figure 2.7 that, with default parameters, supernova destruction plays a subdominant role in setting the dust content of this galaxy, as the destruction rate is always much lower than

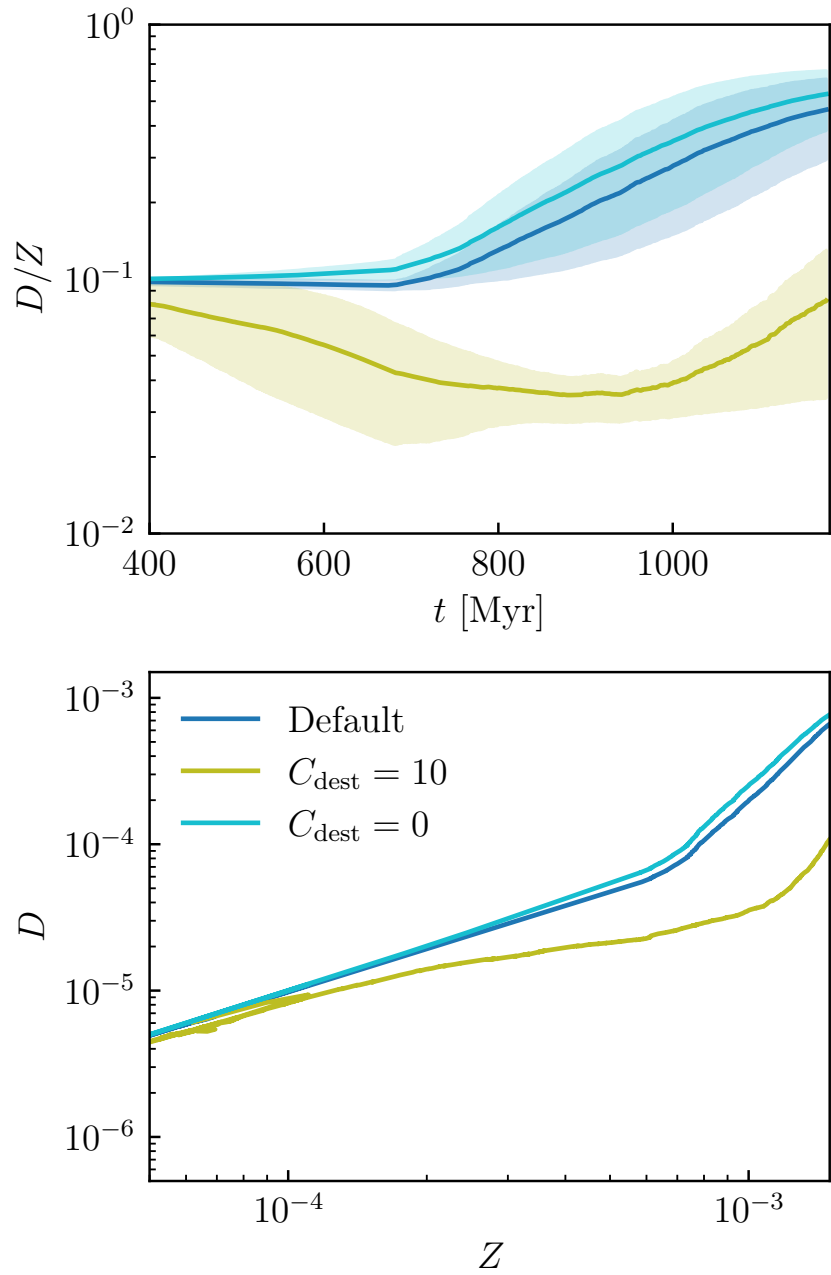


Figure 2.12: Effect of varying supernova remnant destruction efficiency C_{dest} .

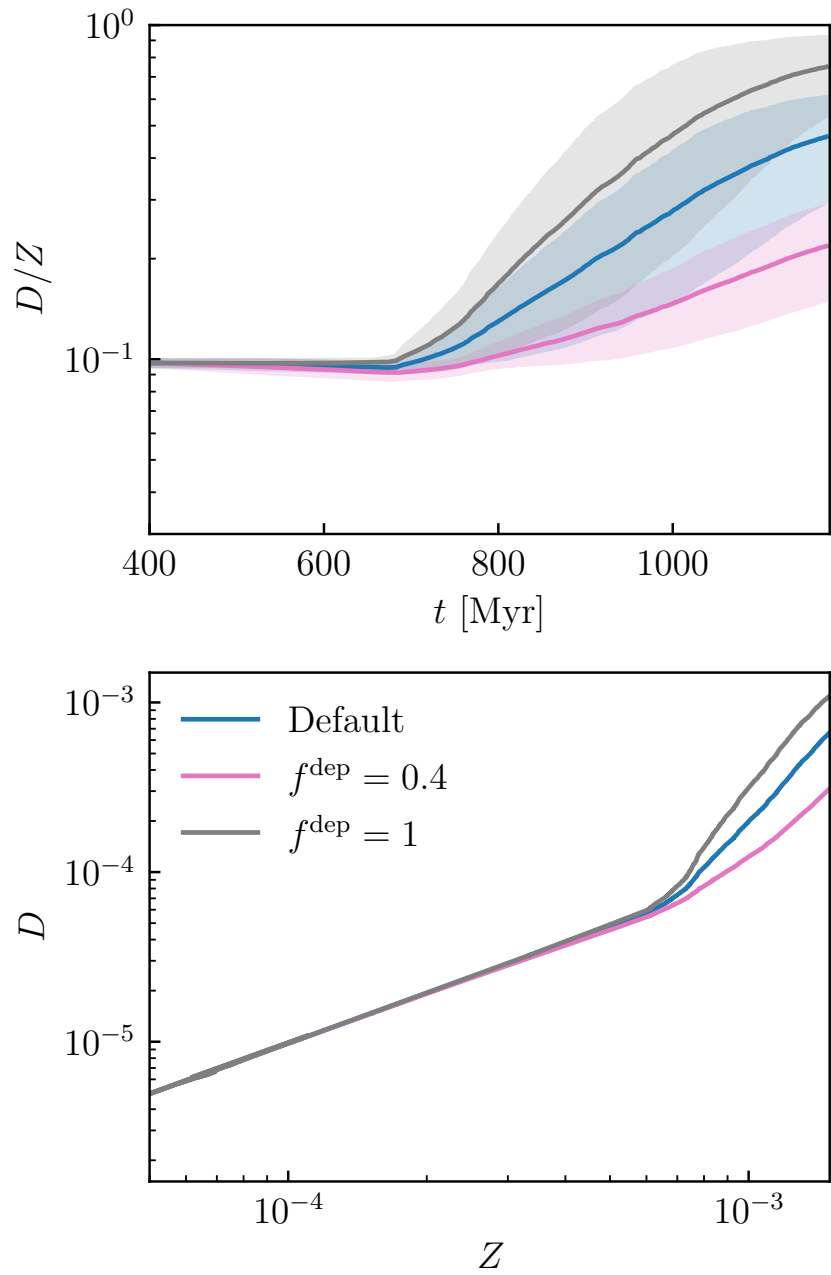


Figure 2.13: Effect of varying maximum ISM metal depletion fraction f^{dep} .

either the production or accretion rates. Therefore, turning off destruction entirely increases the dust-to-metal ratio by $\sim 10\%$ at most. However, enhancement in the SNR destruction rate by a factor of 10 is able to fully counterbalance ISM accretion and suppress D/Z to values less than y_D for most cosmological times in our simulation.

Fig.2.9 shows the result of an alternative choice where the destruction rate is tied explicitly to the sputtering rate predicted by the local gas density and temperature $\dot{D}_{\text{dest}} = \dot{D}_{\text{sputt}}$. As described in Sec. 2.2.3, this would be the more physical choice if the phase structure of the ISM were well resolved in our simulations. However, Sec. 2.2.1 presents evidence that this is not the case. Nonetheless, we wanted to explore the extent of the difference between a local sputtering rate prescription and the default based on local supernova rate. Fig. 2.9 demonstrates that the limited resolution coupled with the delayed-cooling supernova feedback prescription predicts high ISM temperatures and therefore high sputtering rates that dominate all other processes, regardless of the choices made for accretion. Even a reduction of the sputtering rate by an order-of-magnitude, as has been suggested by simulations of galaxy clusters [Gjergo et al., 2018, Vogelsberger et al., 2019], does not qualitatively change this conclusion.

Effect of SFR Correction

Finally we explore the effect of “correcting” the simulated galaxy star formation rates as would be necessary to reproduce the observed stellar-mass halo-mass relation. As described in Sec. 2.2.5, we multiply the star-formation-rate dependent terms – production and supernova rates – by a factor (Eq. 2.14) that was shown in Zhu et al. [2020] to correct the CROC simulated galaxy stellar masses to approximately agree with observations. This significantly increases these rates by roughly a factor of ten by the end of the simulation. We see that initially, the enhanced star formation rate leads to an enhanced supernova destruction rate that significantly reduces the dust-to-metal ratio. However, the increased metallicity result-

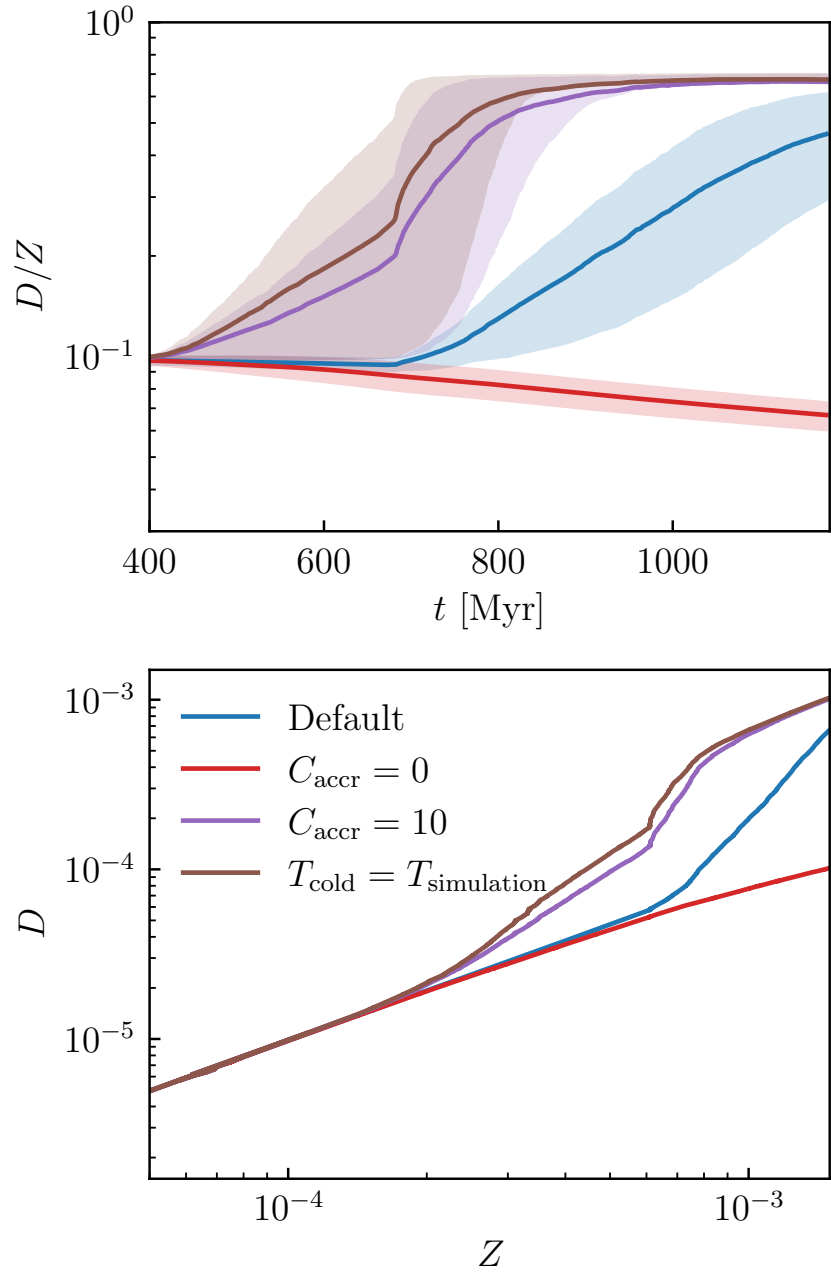


Figure 2.14: Effect of varying ISM accretion rate uncertainty/clumping factor C_{accr} and the cold phase gas temperature T_{cold} (which are degenerate, as explained in the text).

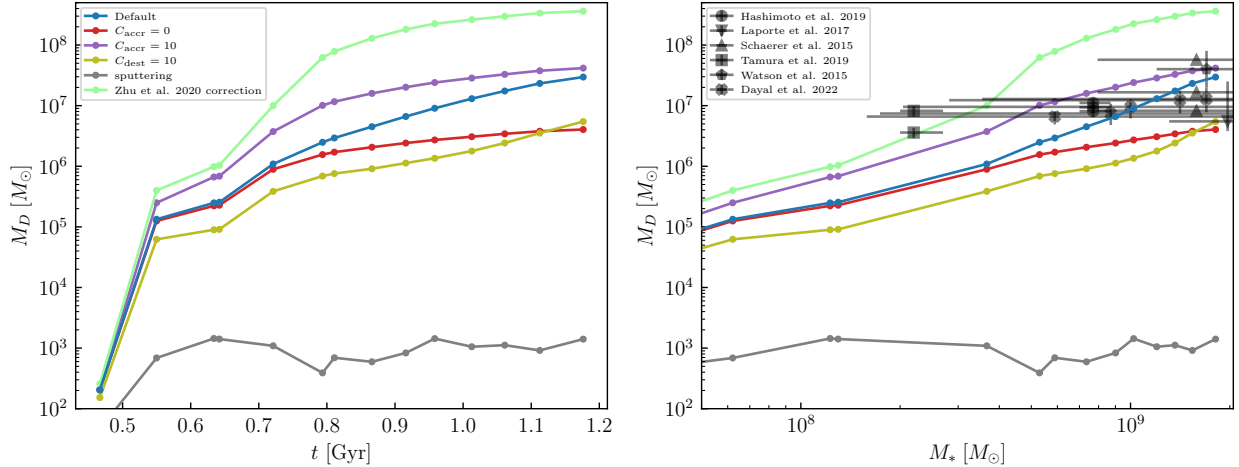


Figure 2.15: Dust mass for representative models as a function of cosmic time (left panel) and stellar mass (right panel). The right panel also contains observational data on the dust masses of galaxies at high redshift $z > 5$ from Hashimoto et al. [2019], Laporte et al. [2017], Schaerer et al. [2015], Tamura et al. [2019], Watson et al. [2015] and Dayal et al. [2022].

ing from the enhanced star formation causes growth by accretion to rapidly dominate and bring $D/Z \sim f_{\text{dep}}$ at earlier cosmic times.

2.3.2 Effect on Observable Quantities and Comparison to Data

Figure 2.15 shows the total dust mass for several representative parameter choices as a function of cosmic time and stellar mass. The stellar mass panel includes observational constraints from galaxies $z \gtrsim 5$. The uncertainties in the data and a lack of a statistically interesting sample of simulated galaxies preclude a quantitative comparison, but it is encouraging that the model predicts qualitatively similar values for the dust mass of this galaxy as is suggested in observations. As well, we note that even excluding the “Zhu et al. [2020] correction” (because it assumes a different star formation history) and “sputtering” (because we believe it is unphysical) models, the total dust mass in the simulated galaxy varies by approximately an order-of-magnitude with different model parameter choices. This suggests the potential of observational probes of galactic dust masses at these redshifts to constrain dust physics models.

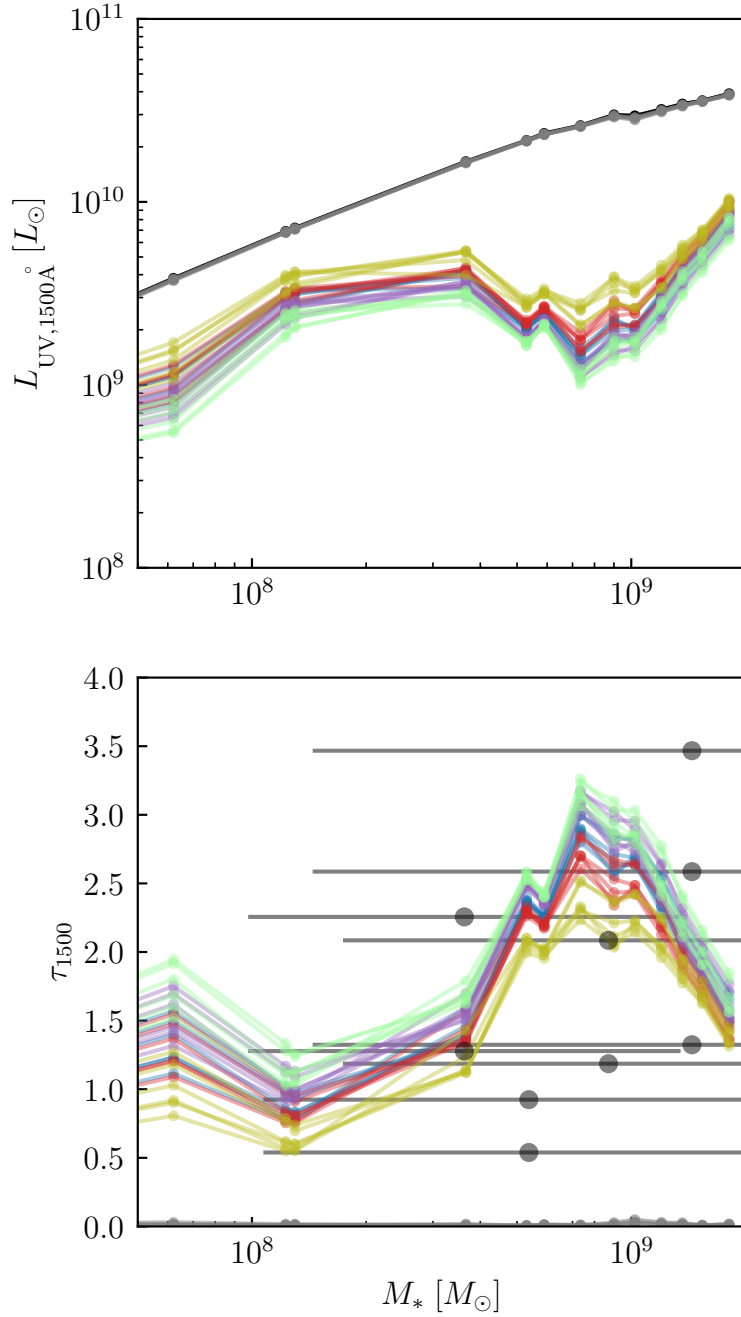


Figure 2.16: Ultraviolet 1500Å luminosities (top panel) and optical depths (bottom panel). Data in the bottom panel are from Ferrara et al. [2022]. Colors are the same as in Figure 2.15.

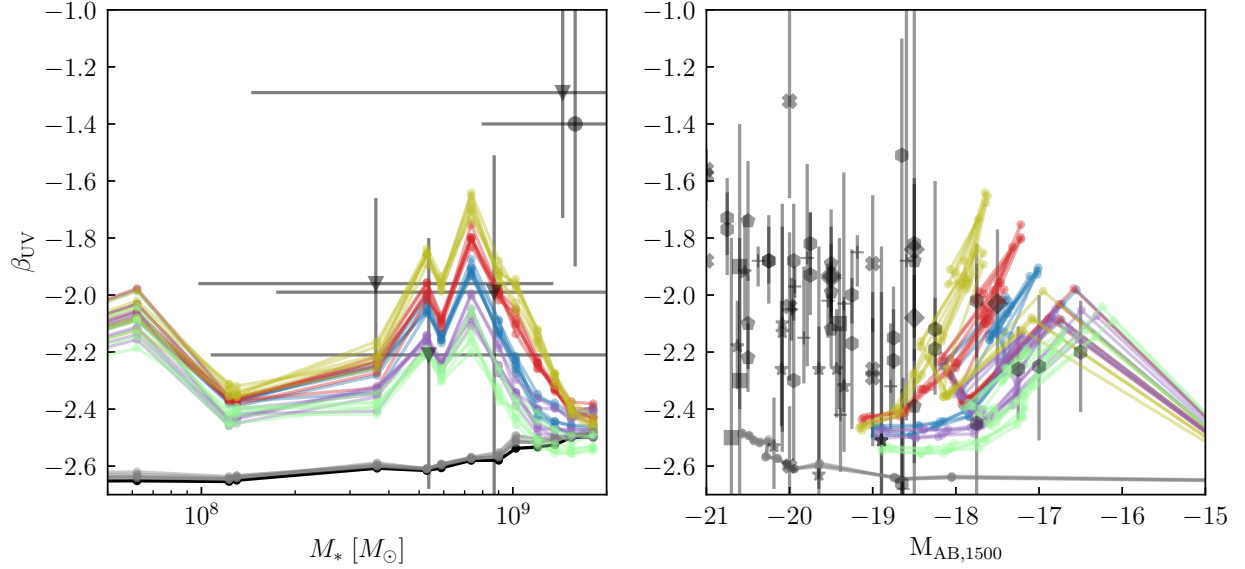


Figure 2.17: UV β slope as a function of stellar mass (left panel) and UV AB absolute magnitude (right panel). Grey points are a compilation of observational data for $z > 5$ galaxies from the literature: Schaerer et al. [2015, circles], Ferrara et al. [2022, downward triangles], Finkelstein et al. [2012, plus-signs], Bouwens et al. [2014, hexagons], Dunlop et al. [2013, diamonds], Bhatavdekar and Conselice [2021, stars], Wilkins et al. [2011, filled x], Dunlop et al. [2012, pentagons], and Wilkins et al. [2016, squares].

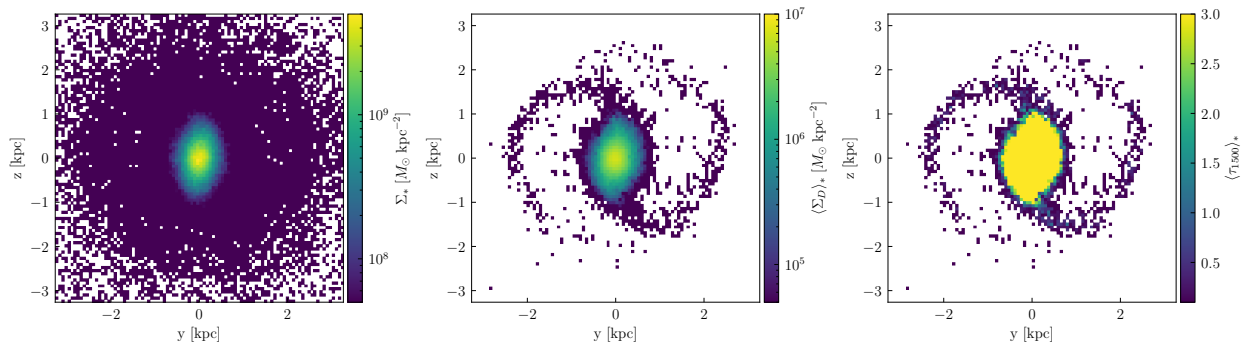


Figure 2.18: Maps of stellar surface density (left panel), average dust surface density (middle panel), and average stellar optical depth to dust (right panel) at $z = 5.2$. Quantities are projected along a random axis with respect to the galaxy (the coordinate z axis).

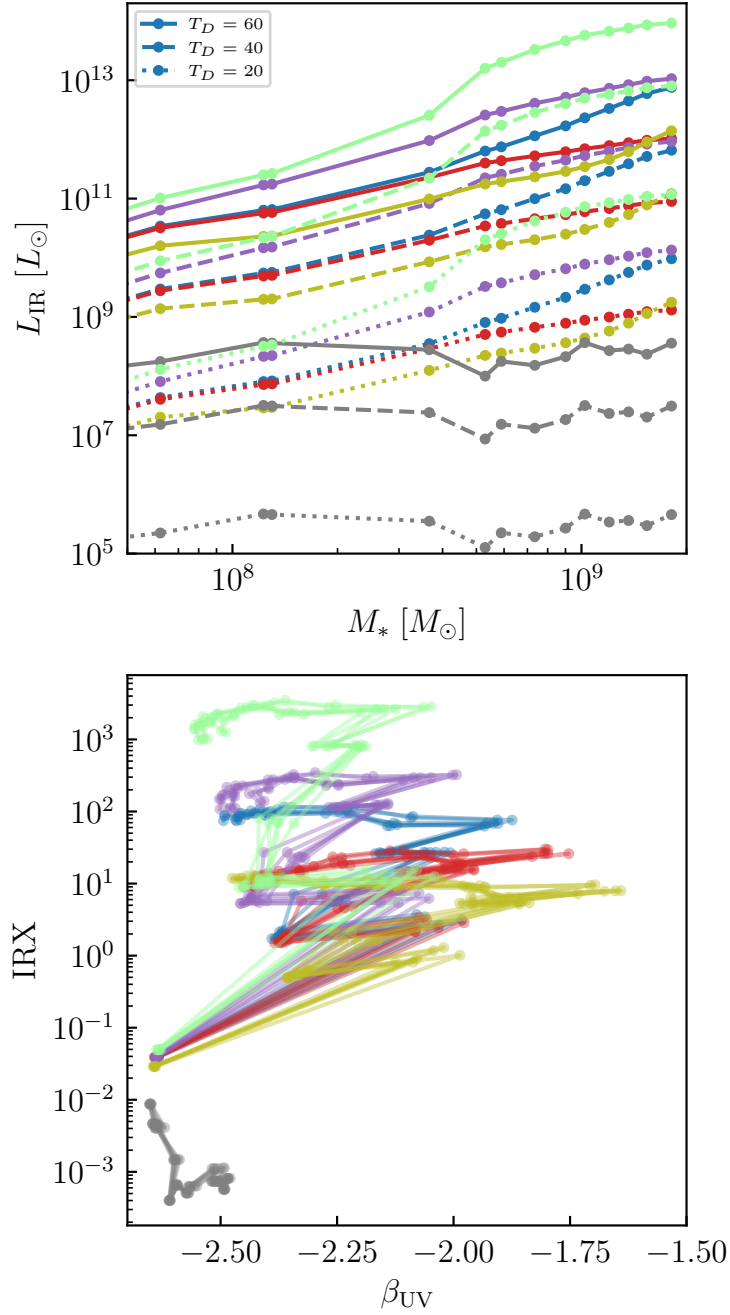


Figure 2.19: Infrared luminosity as a function of stellar mass (top panel) and IRX- β_{UV} relationship (bottom panel). Since we do not self-consistently calculate dust temperatures from the simulation, we show predictions for a reasonable range in the top panel. The bottom panel assumes $T_D = 40\text{K}$.

Figure 2.16 shows the attenuated ultraviolet $\lambda = 1500\text{\AA}$ luminosity of the simulated galaxy, and the corresponding optical depths. Colors correspond to the same dust model parameter choices as in Figure 2.15. Different lines of the same color indicate the same dust model observed from a different viewing angle – six viewing angles along the positive and negative coordinate axes are calculated. Data from Ferrara et al. [2022] are shown for comparison. Figure 2.17 shows the ultraviolet spectrum β slope as a function of stellar mass and attenuated AB absolute magnitude at 1500\AA , along with a compilation of $z > 5$ galaxy measurements from the literature. All dust models except explicit thermal sputtering predict observations qualitatively consistent with the data.

Counter-intuitively, for the non-sputtering models, the ultraviolet optical depth does not increase monotonically with increasing dust mass. This is due to the geometry of the dust distribution and consequent attenuation. Figure 2.18 shows the stellar mass and dust mass distributions, as well as average optical depth along the projection axis. While most of the stars in the galaxy are enshrouded in dust columns that are completely opaque, there exists an extended distribution of stars where there is effectively no dust. At late times, this component accounts for $\sim 10 - 30\%$ of the stellar mass, explaining the relatively low effective optical depths despite high column densities. This also explains the trend in Figure 2.17: the extinguished β_{UV} tends to the unextinguished value at late times because star particles are either completely extinguished due to opaque dust or they are unaffected by low dust columns.

Figure 2.19 shows the infrared luminosity as a function of stellar mass for the simulated galaxy and the IRX-beta relationship. We do not attempt to self-consistently calculate the dust temperature so we present predictions for a range of reasonable values. The direct $\propto M_D$ dependence on dust mass suggests that infrared observables might be better able to distinguish between different dust models, but also highlight the necessity of accurate dust temperature measurements in simulations and observations.

2.4 Discussion

2.4.1 Numerical Methods: Simulation Self-Consistency, Time-Stepping

A major caveat to our method for predicting the dust content of simulated galaxies is the post-processing nature of our particle tracer method. In principle, metals in the dust will impact the dynamics of the ISM very differently from those in the gas-phase: dust removes metals from the gas phase that contribute to high-temperature metal-line cooling, while dust also contributes different cooling mechanisms in the form of photoelectric heating and cooling due to the emission of thermal infrared radiation. Since we post-process the tracer particles after the simulation has been run, our simulations do not take these effects into account and are therefore not entirely self-consistent.

However, we do not think this entirely invalidates our conclusions for several reasons. The first is the fact that, because the phase structure of the ISM is not well resolved in these simulations and the star formation and supernova feedback prescriptions are therefore tuned [see Gnedin, 2014], it is likely that any change in the ISM dynamics by modified cooling and heating functions could be compensated for with changes to these tuned prescriptions. Moreover, the cooling and heating functions in ISM conditions are themselves uncertain by a factor 2-3 due to the uncertainties in the rates of various cooling and heating processes [Wiersma et al., 2009]. Therefore a fully coupled treatment of dust effects on cooling and heating in simulations of this resolution would not necessarily increase their physical realism.

Nonetheless, we emphasize that the present work is a first-step in a broader program to model dust in high-redshift galaxies. In future work we plan to implement a dust model that is fully coupled to the rest of the galaxy formation model and will enable self-consistency at simulation run-time. The model presented in this paper enables a larger exploration of the parameter space of dust physics uncertainties, so that a the calibration of a fully-coupled model will be computationally feasible.

Time cadence is another numerical issue. The choice of $\sim 0.2\text{Myr}$ interval between saved snapshots is somewhat arbitrary and is dictated by the balance between the available computational resources and the desire to fully resolve the time evolution of SN explosions from a single stellar population. We test the sensitivity of our results to this choice by down-sampling our simulation outputs by a factor of 2, i.e. removing every other output and using the remaining to calculate the dust content as described in the methods. This increases the cadence of simulation outputs to $\sim 0.4\text{Myr}$. We find that the predictions of the model under the default parameter assumptions are effectively unchanged. This is unsurprising given that average tracer quantities follow fairly smooth curves as a function of time (Fig. 2.4). Note that this does not necessarily mean fewer timesteps were taken by the ODE solver that integrates the dust equation – as described in the methods, this solver is allowed to take as many time-steps as necessary between simulation outputs (between which tracer quantities are linearly interpolated) based on the specified accuracy of the adaptive integration scheme.

2.4.2 The Physical Model: Comparison to Previous Efforts and Caveats

Several groups have recently implemented dust models similar to ours in galaxy formation simulations, either directly incorporated into the fluid-dynamical solver or in post-processing (as we do). Since this is primarily a methods paper, we will not present a comprehensive survey of these results and their comparison to ours, but instead highlight the main methodological differences between our model and others, and speculate on their effects.

Because of the uncertainties in dust physics described in the Introduction, most efforts to incorporate a fully-coupled dust model in a cosmological fluid-dynamical simulation of galaxy formation must necessarily explore some subset of the plausible dust model parameter space as calibration [e.g. Bekki, 2015, McKinnon et al., 2016, 2017, Gjergo et al., 2018, Li et al., 2019b, Granato et al., 2021, Parente et al., 2022]. However, an advantage of our method compared to these efforts is the relatively large model parameter space we have ex-

explored while simultaneously spatially resolving an individual galaxy. Figure 2.15 emphasizes how reasonable variations in uncertain parameters related to dust accretion in the ISM and destruction can lead to at least an order-of-magnitude difference in the predicted dust mass for the same galaxy. Consequently, absent a first-principles calculation or independent measurement of these parameters, the full range must be explored to honestly assess predictions in comparison to data. Of course, this also requires a statistically meaningful sample of simulated galaxies with a range of masses and formation histories to compare to the data, which we will present in forthcoming work.

This broader parameter exploration is enabled by our particle tracer post-processing method, which allows us to run the full gas-dynamical cosmological galaxy formation simulation only once and subsequently post-process with a range of dust model parameters, admittedly at the expense of some physical realism. While several studies have similarly post-processed simulations run with Lagrangian fluid dynamics solvers [Mancini et al., 2015, 2016, Hirashita and Aoyama, 2019, Huang et al., 2021], of these only Huang et al. [2021] perform a parameter variation to explore the predictions of their model. Given the different aims of that analysis (the investigation of the full grain-size distribution in Milky Way-mass galaxies), and their use of a very different galaxy formation simulation model [Weinberger et al., 2017, Pillepich et al., 2018], our findings are complementary. This post-processing technique naturally lends itself to the inclusion of increasingly complex physics, such as an accounting for the full grain-size distribution and multiple grain species, which we plan to investigate.

A main conclusion of our model development analysis is the importance of a carefully chosen dust destruction model. As emphasized in Figures 2.9 and 2.15, the destruction rate predicted due to supernova remnants (eq. 2.10) can be vastly different from that calculated from the thermal sputtering rate expected from the erosion of grains by collisions with high-temperature gas particles (eq. 2.9). This is likely due to the unresolved nature of the ISM

in our simulations coupled to the feedback prescription: delayed cooling feedback appears to produce an overly-hot ISM (see Figures 2.2 and 2.3) but fails to drive that hot ISM out in galactic winds. The strong temperature dependence expected of the sputtering rate therefore predicts unphysically high destruction rates that prevent the accumulation of dust in the galaxy ISM to anything close to observational constraints. Previous efforts do not appear to have seen this issue because of their fundamentally different feedback model that employs a pressurized equation of state ISM and wind particles [Springel and Hernquist, 2003]. In this model, the ISM gas remains at sufficiently low temperatures that thermal sputtering is never dominant and can be included along with SNR destruction without effective double-counting. One hopes that a more realistically thermodynamically structured ISM would result in eq. 2.10 and eq. 2.9 predicting more similar destruction rates – as most of the hot gas that results in sputtering is expected to come from SNRs.

An additional uncertainty in our destruction prescription is the effect of sputtering in high-temperature circumgalactic gas. Since this gas is not co-spatial with supernovae, it is unaccounted for in our default destruction prescription based on SNRs. Therefore tracers that sample dusty gas in the ISM but are blown out into the galactic halo will retain their dust even if the ambient temperatures are so high as to result in effective sputtering. In principle, this inaccuracy could be remedied by an on-the-fly, fully coupled treatment of dust physics in the simulation, which would allow for the instantaneous distinction between hot gas in the ISM due to delayed cooling (where sputtering would be over-predicted) and hot gas in the CGM where thermal sputtering should still be allowed by the dust evolution scheme. We plan to implement such a fully coupled model which will allow a quantification of this uncertainty, but this remains outside the scope of the current work.

2.4.3 Prospects for high- z Constraints

While figures 2.10 through 2.15 indicate the sensitivity of dust-to-metal ratio (and therefore total dust mass) on the assumed parameters of the dust model, Figures 2.16 and 2.17 indicate only modest effects on observable properties related to the produced UV radiation. This is because even the least-dust-rich models (save sputtering, which for reasons discussed above we consider unphysical), predict column densities that leave most of the central galaxy opaque. While this prediction could perhaps be sensitive to the spatial resolution of the ISM – a more multi-phase and inhomogeneous ISM might predict a wider distribution of column densities that could have low-value tail more sensitive to the dust content – at face-value this suggests that learning dust physics from observations that are sensitive to the rest-frame UV SED of high redshift galaxies will be inherently difficult.

Figure 2.19 gives some hope in that the infrared luminosity is monotonically related to the total dust mass and therefore in principle more sensitive to differences between models, this observable depends even more sensitively ($\sim T^4$) on the dust temperature. On top of both of these issues is the assumed dust opacity model [Weingartner and Draine, 2001], which is derived from very local galaxies and therefore might be inappropriate for the high-redshift systems we investigate here. All of this suggests that future theoretical efforts will have to contend with the details of simulated ISM physics, the dust temperature, and the dust size distribution to reliably translate observational data into dust physics constraints. However, all of these statements await more conclusive judgement with a larger sample of simulated galaxies.

2.5 Conclusions

- We present a method for the prediction of the dust content of high-redshift galaxies with the Cosmic Reionization On Computers (CROC) cosmological, fluid-dynamical simulations of galaxy formation.

- We use a particle tracer technique to integrate an ODE for the evolution of the dust-to-gas ratio along pathlines that sample the simulated ISM in post-processing.
- This ODE captures a physical model for the production, growth, and destruction of dust. Dust is assumed to be produced by supernovae and AGB stars, is allowed to grow due to the accretion of metals from the gas phase of the ISM, and is assumed to be destroyed by supernovae remnant shocks.
- Reproducing earlier work [Genel et al., 2013, Semenov et al., 2018], we find that the numerical method for calculating fluid flow pathlines with particle tracers in the simulation is important for fully sampling the gas distribution in the ISM at all times in the simulation.
- For simulations that do not resolve the phase structure of the ISM, different reasonable choices for grain destruction rates can predict very different predictions, especially when delayed cooling feedback is used. Delayed cooling feedback appears to produce an unrealistically warm/hot ISM, so explicitly calculating the destruction rate predicted from thermal sputtering is an over-prediction and effectively destroys all the dust. Instead, calculating the destruction rate based on the local supernova rate and assuming each remnant sweeps up a density-dependent mass of ISM, in which some fraction of dust is destroyed, produces more reasonable destruction rates. We adopt this for our default model.
- Our numerical implementation reproduces a “classical” result [see Hirashita, 2013, for a review] – the dust-to-gas ratio passes through two regimes determined by metallicity (for a given set of model parameters): the low metallicity D/Z is set by the production yields y_D , the high metallicity is set by the depletable fraction of metals in the ISM f^{dep} , and the transition regime is set primarily by the timescale for grain growth in the ISM τ_{accr} . With default parameters, supernovae are the dominant source of dust

production in these early cosmic epochs, but even absent supernova dust production, AGB stars alone provide enough dust that ISM accretion can bring the dust-to-metal ratio to large values (\sim tens of percent) by $z = 5$.

- We run this dust model on the single most massive galaxy in a $10 \text{ cMpc}h^{-1}$ box ($\sim 2 \times 10^9 M_\odot$ by $z = 5$). We find that the model is capable of reproducing dust masses and dust-sensitive observable quantities broadly consistent with existing data from high-redshift galaxies.
- The total dust mass in the simulated galaxy is somewhat sensitive to parameter choices for the dust model, since the effective growth timescale is comparable to the age of the universe at these redshifts. Consequently, observable quantities that can constrain galaxy dust mass at these epochs are potentially useful for placing constraints on dust physics in the ISM.
- However, due to the geometry of the dust distribution – which is so centrally concentrated that all viable models predict similar opacity distributions – dust-sensitive observables due to extinction in the UV vary little with changes in dust model parameters. Moreover, the most direct measure of total dust mass – the infrared luminosity L_{IR} – is strongly sensitive to the dust temperature, which will require more careful calculations to predict self-consistently.

CHAPTER 3

PREDICTIONS FOR THE $Z > 5$ GALAXY POPULATION AND COMPARISON TO OBSERVATIONS

3.1 Introduction

In the previous chapter, we presented a method for modelling the dust content of galaxies in cosmological simulations of the reionization era (up to and including $z = 5$, when the universe was 1.2 Gyr old). For purposes of computational feasibility, this method development was done using the single most-massive galaxy in a $10h^{-1}$ cMpc cosmological volume. However, because the initial conditions of large-scale structure are Gaussian random fields, galaxies form in dark matter halos with a wide range of masses and formation histories, which we know to fundamentally impact galaxy properties Behroozi et al. [see 2019, for contemporary constraints]. Theoretical efforts must therefore strive to make predictions for halos that sample the distributions of masses and formation histories as completely as possible, in order to make predictions for the galaxy population in the real universe.

This modelling is especially urgent given the recent onslaught of data from JWST, coupled with ambitious programs using radio telescope arrays such as ALMA, that are rapidly fleshing out the properties of the high-redshift galaxy population. Some of the most exciting and puzzling results from this recent revolution have implicated cosmic dust in a central role. While dependent on photometric candidate detections without spectroscopic confirmation and therefore subject to possible revision, claims of anomalously bright galaxies and a surprisingly high star formation rate density at $z > 10$ abound [see Bouwens et al., 2023, and references therein]. If confirmed, reconciling these with the concordance cosmology may present a challenge, and the many uncertainties of dust enrichment in the first galaxies have been invoked as possible explanations [Mirocha and Furlanetto, 2023, Mason et al., 2023, Ferrara et al., 2023]. Galaxies with spectroscopic confirmation rest on surer footing, and

thus far all show evidence for little dust attenuation $z \gtrsim 10$ [Roberts-Borsani et al., 2022b, Arrabal Haro et al., 2023b, Bunker et al., 2023, Curtis-Lake et al., 2023, Tacchella et al., 2023, Arrabal Haro et al., 2023a].

Nonetheless, the reionization epoch is anything but dust-free. ALMA programs REBELS [Bouwens et al., 2022b, Inami et al., 2022] and ALPINE [Le Fèvre et al., 2020] and others [Bowler et al., 2022] have detected thermal dust continuum emission that firmly establishes significant amounts of dust in at least some galaxies by $z = 5-7$ [Fudamoto et al., 2020, Pozzi et al., 2021, Algera et al., 2023, Barrufet et al., 2023]. These observations also hint at complicated dust morphologies with significant spatial displacement from the stellar component [Bowler et al., 2022, Inami et al., 2022]. As well, Rodighiero et al. [2023] present an analysis of JWST candidate detections that suggest significant dust obscuration at $8 < z < 13$. Overall, there is convincing evidence for the very rapid build-up of dust during the reionization epoch, especially in the most massive galaxies. Models of galaxy formation will therefore need to account for the physics of dust if they are to satisfactorily explain key observable constraints on cosmic dawn.

With this goal, in this Chapter we now extend our analysis by applying our dust modelling framework to a suite of 10 additional simulated galaxies from the same simulation volume, selected with approximately uniform logarithmic spacing in final halo mass $1.1 \times 10^9 M_\odot \leq M_{\text{vir}} \leq 5.0 \times 10^{11} M_\odot$, corresponding to stellar masses $3.7 \times 10^5 M_\odot \leq M_* \leq 1.9 \times 10^9 M_\odot$, allowing us to assess the dependence of our predicted dust properties on galaxy mass at a given cosmological time, which is not possible with just one galaxy. The observationally suggested paucity of dust at cosmic dawn motivates us to also explore a wider range of dust modelling choices than in the previous chapter, namely those that either produce less dust or destroy it more efficiently. Section 3.2 explains our simulated galaxy sample selection, notes small updates to the methodology presented in the previous Chapter, and presents the dust model variations explored in this analysis. Section 3.3 presents the galaxy mass-metallicity

relation predicted by the simulations (since this sets the normalization for dust contents) compared to existing high-redshift constraints, and results of the dust model applied to our simulated galaxy sample. We present both the predicted dust content and dust-sensitive observable quantities, which we compare to existing data. Section 3.4 discusses the agreements and discrepancies between our model predictions and observational constraints, and compares our work to other recent similar investigations in the literature. We conclude in Section 3.5.

3.2 Methods

The galaxy formation simulation model, halo identification, and galaxy definitions are identical to those described in the previous Chapter, to which we refer the reader. For this Chapter’s analysis, we select a total of 11 galaxies from a $10h^{-1}$ co-moving Megaparsec (cmMpc) cosmological volume with final $z = 5$ halo masses $1.1 \times 10^9 M_\odot \leq M_{\text{vir}} \leq 5.0 \times 10^{11} M_\odot$, corresponding to final stellar masses $3.7 \times 10^5 M_\odot \leq M_* \leq 1.9 \times 10^9 M_\odot$. These limits span the range of halo masses resolved in the simulation. The 11 halos are selected with approximately logarithmically uniform spacing in final halo mass. Since the galaxy scaling relations predicted by CROC have small scatter (see Zhu et al. [2020] and Noel et al. [2022]) and do not dramatically change slope on scales $\lesssim 0.5$ dex in halo mass, it is sufficient for the purposes of this analysis to sample one halo of a given mass with the average spacing of 0.24 dex provided by a total sample of 11. This simulation has the same initial conditions as the one used in the previous Chapter, so the most massive halo is the same.

As in the previous Chapter, we sample ISM conditions in these simulated galaxies along pathlines traced by Lagrangian tracer particles. These particles are initialized in random positions in the Lagrangian region of the halo and follow the fluid flow using the Monte-Carlo method introduced in Genel et al. [2013] and implemented in the ART code in Semenov et al. [2018]. The number of tracers per halo scales with halo mass such that the minimum

number of tracers for a given halo is above 100. For galaxies hosted in halos with final masses $M_{\text{vir}} > 10^{11} M_{\odot}$, we downsample to 10^4 particles for computational feasibility.

However, computational resource limitations prevent us from using enough tracers that all cells in each galaxy are sampled. Consequently, we must find a way to assign dust masses to cells in the galaxy which were not sampled by any tracer. To do this, we interpolate the D/Z vs Z relation for the tracers in each galaxy at every snapshot output. As shown in Figure 3.1, the dust-to-metal ratio scales regularly with metallicity, making this interpolation the best option for assigning dust masses to unsampled cells in a way that preserves the predictions of the dust model. We note that with some model choices even this relation exhibits significant scatter at a given tracer metallicity. Our correction therefore possibly underestimates the scatter in observable quantities impacted by the dust distribution.

We note that in Esmerian and Gnedin [2022] we had not yet realized this correction was necessary, and therefore the results in that paper underestimate the total dust mass and effect of dust on observable quantities. These effects are $\mathcal{O}(10\%)$ in the dust mass but can be order-unity for some observable quantities that depend sensitively on the dust distribution – particularly dust extinction of UV starlight – but do not change the qualitative conclusions of that paper. Otherwise, the methods used to calculate dust-dependant observables (the effective optical depth to dust at 1500\AA : τ_{1500} , the logarithmic spectral slope in the UV: β_{UV} , the infrared luminosity: L_{IR} and the infrared excess $\text{IRX} \equiv L_{\text{IR}}/L_{\text{UV}}$) are identical to the description in Section 2.6 of Esmerian and Gnedin [2022].

3.2.1 Dust Model Parameter Exploration

As in the previous Chapter, we run a suite of dust models with different parameter choices to explore their impact on the predicted dust content of high-redshift galaxies and dependent observables, now on a sample of multiple simulated galaxies. However, motivated

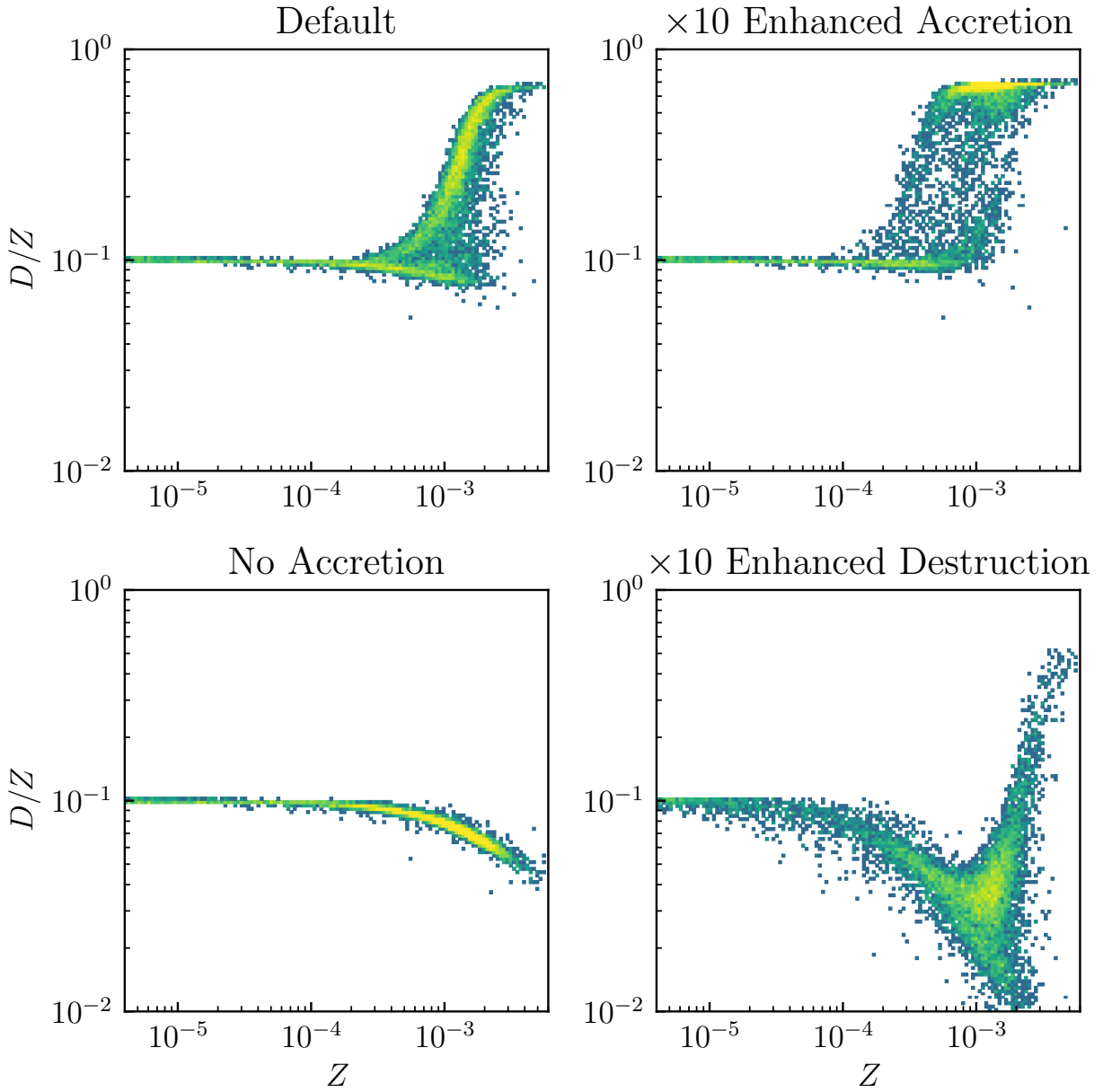











Figure 3.1: Spatially-resolved D/Z vs Z relations. Each panel shows the 2D pdf of mass for D/Z vs Z in the ISM of the most massive galaxy at the last snapshot. Different panels correspond to different dust models.

Table 3.1: Explored Parameter Combinations. Note that for each model, any parameter not listed under Key Parameters is the same as the Default model.

Model Name	Key Parameters	Description	Color in Figures
Default	$y_{D,SN} = y_{D,AGB} = 0.1,$ $\tau_{\text{accr}} = 3 \times 10^8 \text{yr}, C_{\text{dest}} = 1$	Default from Esmerian and Gnedin [2022], parameters based on Dwek [1998], Feldmann [2015].	
No Accretion	$\tau_{\text{accr}} = \infty$	No grain growth due to gas-phase accretion in cold ISM	
Enhanced Accretion	$\tau_{\text{accr}} = 10\tau_{\text{accr,Default}}$	Enhanced grain growth due to gas-phase accretion in cold ISM	
No Destruction	$C_{\text{dest}} = 0$	No grain destruction in hot gas due to SNRs	
Enhanced Destruction	$C_{\text{dest}} = 10C_{\text{dest,Default}}$	Enhanced grain destruction in hot gas due to SNRs	
Very Enhanced Destruction	$C_{\text{dest}} = 100C_{\text{dest,Default}}$	Very enhanced grain destruction in hot gas due to SNRs	
Low SN Production	$y_{D,SN} = 0.1y_{D,SN,Default}$	Suppressed dust yield from SN	
No SN Production	$y_{D,SN} = 0$	SN do not produce dust	
Very Low SN Production, No AGB Production	$y_{D,SN} = 0.1y_{D,SN,Default},$ $y_{D,AGB} = 0$	Very suppressed dust yield from SN, AGB do not produce dust	

by observations that increasingly point to minimal dust in the earliest galaxies [e.g. Roberts-Borsani et al., 2022b, Tacchella et al., 2023], we extended the set of parameter variations explored in Chapter 2 by introducing 3 new models that either increase the grain destruction rate in supernova remnants (**Very Enhanced Destruction**) or decrease grain production in SN and/or AGB (**No SN Production**, and **Very Low SN Production, No AGB Production**). The list of models explored in this Chapter are summarized in Table 3.1 and described below. Note that each model is assigned a unique color for Figures 3.4-3.9, which is shown in the right-most column of the table.

- **Default:** This is identical to the “Default” model explored in Esmerian and Gnedin [2022], for which parameters were chosen to be the same as successful similar physical models of dust evolution for local-universe galaxies [Dwek, 1998, Feldmann, 2015, Li et al., 2019b].
- **No Accretion:** This is identical to the “No Accretion” model in Esmerian and Gnedin [2022]. The parameters of this model are identical to **Default** except grain growth due to accretion of gas-phase metals in the cold molecular ISM is not allowed. This parameter choice is motivated by (simplified) arguments based on microphysical considerations of dust grain geometry that grain growth in the cold phase of the ISM should not be possible [Ferrara et al., 2016].

- **Enhanced Accretion:** This is identical to the “Enhanced Accretion” model in Esmerian and Gnedin [2022]. The parameters of this model are identical to **Default** except grain growth due to accretion of gas-phase metals in the cold molecular ISM is enhanced by an order of magnitude. This parameter choice is motivated both by uncertainties in the unresolved density distribution of the cold ISM in our simulations, where grain growth is expected to be most efficient, and to enable comparison to other works that adopt faster grain growth rates [Graziani et al., 2020, Lewis et al., 2023].
- **No Destruction:** This is identical to the “No Destruction” model in Esmerian and Gnedin [2022]. The parameters of this model are identical to **Default** except grain destruction in the hot gas of SNRs is not allowed. This parameter choice is motivated by indirect observational indications of inefficient dust destruction in high-temperature gas [Gall and Hjorth, 2018, Gjergo et al., 2018, Vogelsberger et al., 2019, Michałowski et al., 2019], as well as uncertainties in the unresolved ISM phase structure in our simulations.
- **Enhanced Destruction:** This is identical to the “Enhanced Destruction” model in Esmerian and Gnedin [2022]. The parameters of this model are identical to **Default** except grain destruction in the hot gas of SNRs is enhanced by an order of magnitude. This parameter choice is motivated by uncertainties in the destruction efficiency of individual supernova remnants both due to the microphysics of dust and unresolved ISM phase structure [McKee, 1989, Hu et al., 2019, Kirchschrager et al., 2022].
- **Very Enhanced Destruction:** The parameters of this model are identical to **Default** except grain destruction in the hot gas of SNRs is enhanced by two orders of magnitude. The motivation for this parameter choice is the same as for **Enhanced Destruction**, since the associated uncertainties are large, and also the increasing evidence for dust-free early galaxies as mentioned previously.

- **Low SN Production:** Identical to **Default** except the dust yield from supernova is suppressed by an order of magnitude (i.e. $y_{D,\text{SN}} = 0.01$). Note that we do not change the AGB yield $y_{D,\text{AGB}}$, and since the AGB metal production is about 10 times smaller than that of SN [see Esmerian and Gnedin, 2022, Figure 7], SN and AGB production are comparable with these parameters. This parameter choice is also motivated by the evidence for minimally dusty high-redshift galaxies, and uncertainties about the fraction of SN-produced dust that survives the reverse shock [see e.g. Bianchi and Schneider, 2007a, Micelotta et al., 2016, Slavin et al., 2020].
- **No SN Production:** Identical to **Default** but SN production is turned off – $y_{D,\text{SN}} = 0$. This choice is motivated by the extreme scenario in which no dust survives the reverse shock of any supernova.
- **Very Low SN Production, No AGB Production:** Identical to **Default** except the dust yield from supernova is suppressed by two orders of magnitude (i.e. $y_{D,\text{SN}} = 10^{-3}$) and AGB production is turned off ($y_{D,\text{AGB}} = 0$). This is motivated by the same considerations as for the previous two models, and the deep uncertainties around AGB dust production especially in the early universe [e.g. Valiante et al., 2009, Schneider et al., 2014, Dell’Agli et al., 2019, Tosi et al., 2023].

3.3 Results

3.3.1 The Mass-Metallicity Relation

The dust content of galaxies is normalized by their overall metal content, so we first examine the galaxy metallicities in the simulations. Figure 3.2 shows the mass-metallicity relation for our simulations, including existing data at relevant redshifts. While the data mainly overlap with only the highest-mass galaxies in our sample, where there is overlap we see fairly good agreement, albeit with some indications of systematically low metallicities in CROC.

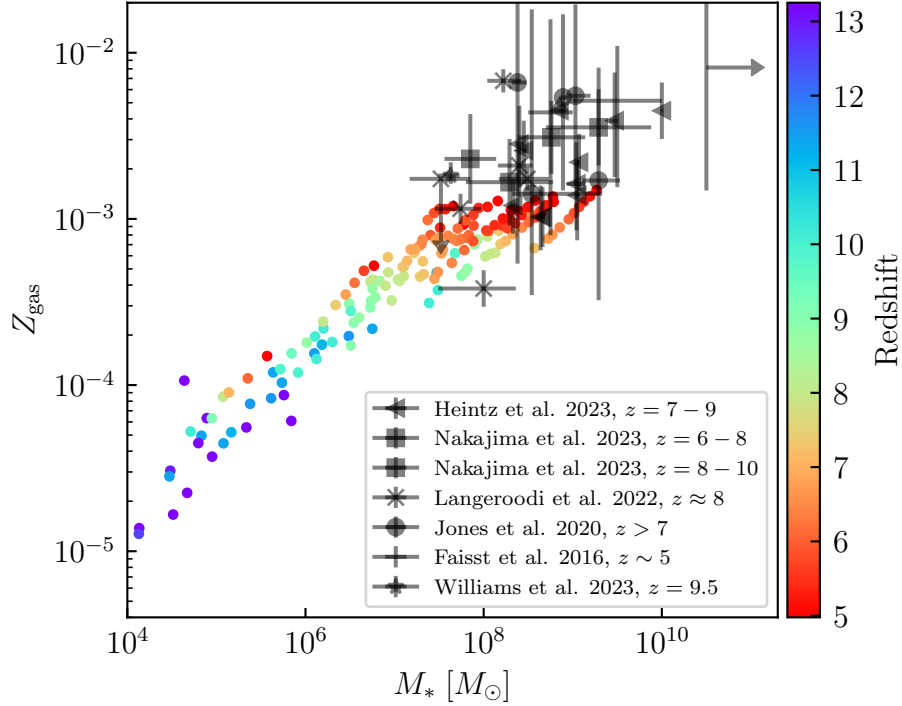


Figure 3.2: Mass-Metallicity Relation. The galaxy-averaged gas-phase metallicity is shown as a function of stellar mass. Each point represents an individual galaxy at an individual snapshot, colored by redshift. Observational data from galaxies at similar redshifts are from Faisst et al. [2016], Jones et al. [2020], Langeroodi et al. [2022], Nakajima et al. [2023], Heintz et al. [2022], and Williams et al. [2023] converted to mass fraction using $12 + [\text{O}/\text{H}]_{\odot} = 8.71$ and $Z_{\odot} = 0.02$ [Lodders, 2019]

The galaxy scaling relations of other quantities predicted by CROC have been thoroughly discussed and compared to existing data in Zhu et al. [2020]. We note that Noel et al. [2022] presented a more detailed analysis of the CROC mass-metallicity relation, but at the time these high-redshift data were not available for comparison, making this a new result.

3.3.2 *The Dust Content of High-Redshift Galaxies*

The dust content of our simulated galaxies predicted by the models described in Section 3.2.1 and Table 3.1 are summarized in Fig. 3.3, where we show the galaxy-averaged dust-to-metal ratio D/Z as a function of galaxy metallicity Z in mass-fraction units (i.e. in which solar metallicity is 0.02). The top row shows the default model and variations in the ISM grain growth accretion timescale. The middle row shows variations in the grain destruction efficiency of supernova remnants. And the bottom row shows variations in the assumed yields of dust production sources.

Broadly, we notice several trends. A well-established property of dust models similar to ours is the transition of dominant physical processes between low and high-metallicity regimes: the D/Z ratio at low metallicity ($Z \lesssim 4 \times 10^{-4} = 2 \times 10^{-2} Z_{\odot}$) is primarily set by the choice of source yields $y_{D,\text{SN/AGB}}$, while the ratio at high metallicity is determined by a competition between the timescale for grain growth due to accretion in the ISM, and the efficiency of grain destruction in the hot ionized medium. If grain growth dominates, (as in **Default**, **Enhanced Accretion**, **No Destruction**, **Low SN Production**, **No SN Production**, and **Very Low SN, No AGB**) the D/Z ratio rises with increasing metallicity, while when destruction dominates (**No Accretion**, **Enhanced Destruction**, **Very Enhanced Destruction**) the opposite scaling is observed.

However, we note that in some models there is substantial scatter between galaxies even at fixed metallicity, particularly for those models where accretion dominates at late times. The efficiency of grain growth via accretion must therefore depend on galaxy properties beyond

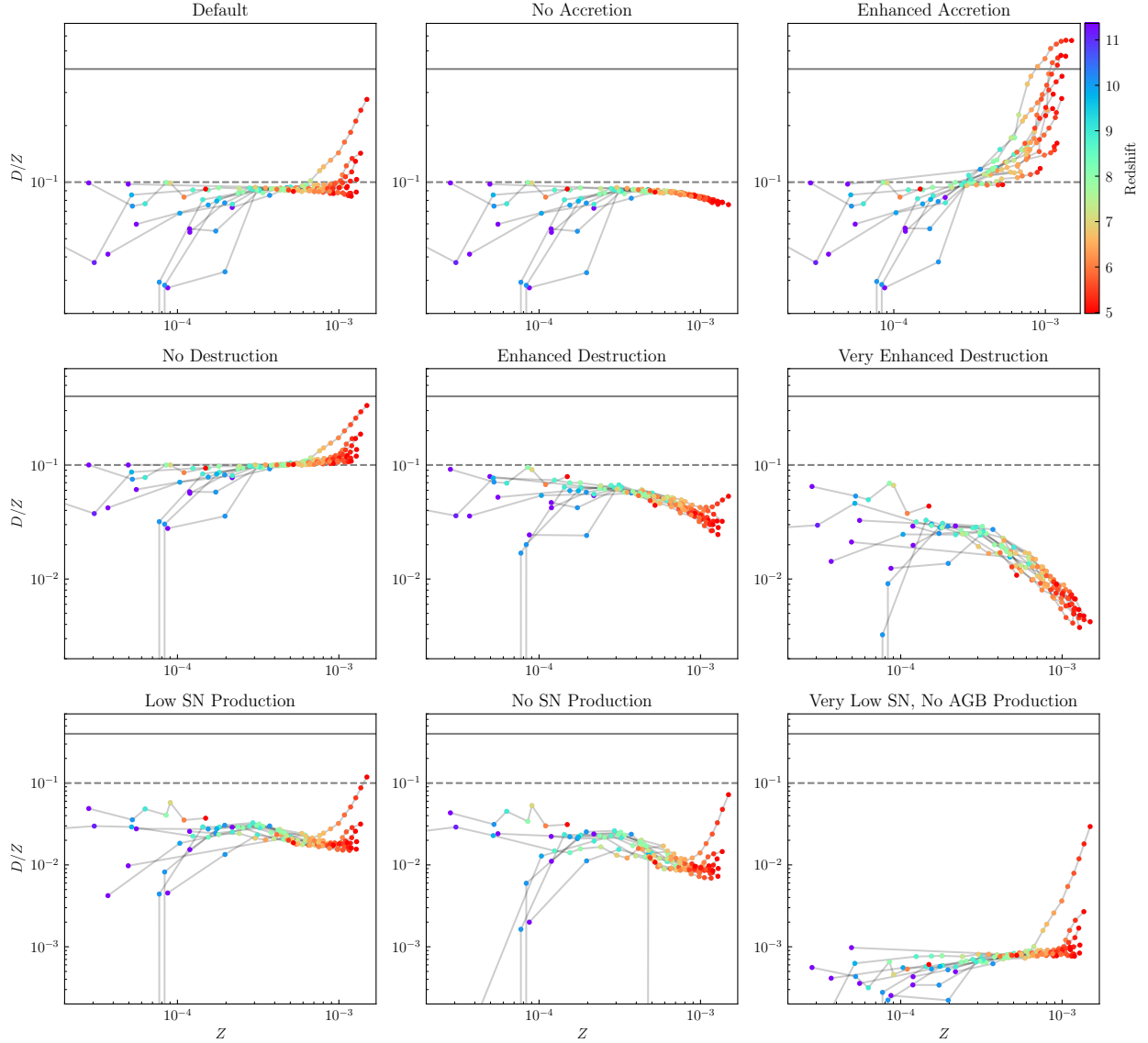


Figure 3.3: Galaxy-Averaged D/Z vs. Z relations. Each panel shows the evolution of the dust content in our simulated galaxies with a different set of assumed dust model parameters, as indicated by the titles. Each point corresponds to the average D/Z and Z values for an individual galaxy at an individual snapshot. Z is in physical (i.e. mass fraction) units. Points from the same galaxy are connected with grey lines, and colors indicate redshift. The dashed horizontal grey line indicates $D/Z = 0.1$, which is the default production yield in our model and the solid horizontal grey line indicates $D/Z = 0.4$, the value for the Milky Way and a common choice in post-processing analyses (see Discussion).

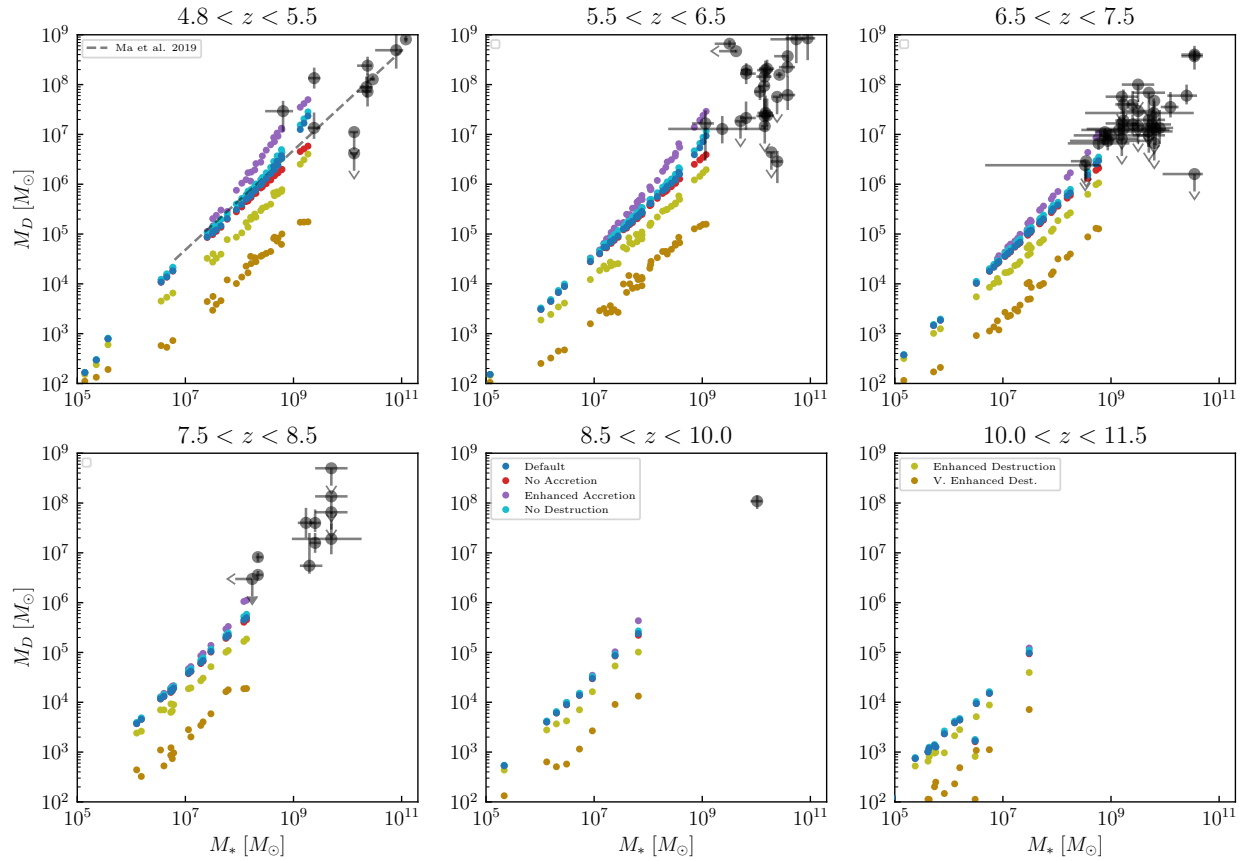


Figure 3.4: Dust mass-stellar mass relation. Colors indicate different dust models which include **Default** and those with varied growth or destruction parameters (i.e. the first two rows of those shown in Fig. 3.3). Each point is a single galaxy at a single redshift, and separate panels are redshift bins. Estimates based on observational data from Sommovigo et al. [2022], Dayal et al. [2022], Hashimoto et al. [2019], Knudsen et al. [2017], Schaerer et al. [2015], Watson et al. [2015], Laporte et al. [2017], Tamura et al. [2019], da Cunha et al. [2015], Marrone et al. [2018], Burgarella et al. [2020, with a redshift for ID27 from Aravena et al. [2016]], Pozzi et al. [2021, with stellar masses from Faisst et al. [2020]], Witstok et al. [2023], and Leńniewska and Michałowski [2019] are shown with the same redshift binning. The predictions of a simpler dust post-processing model on higher-resolution simulations presented in Ma et al. [2019] is shown in the dashed grey line.

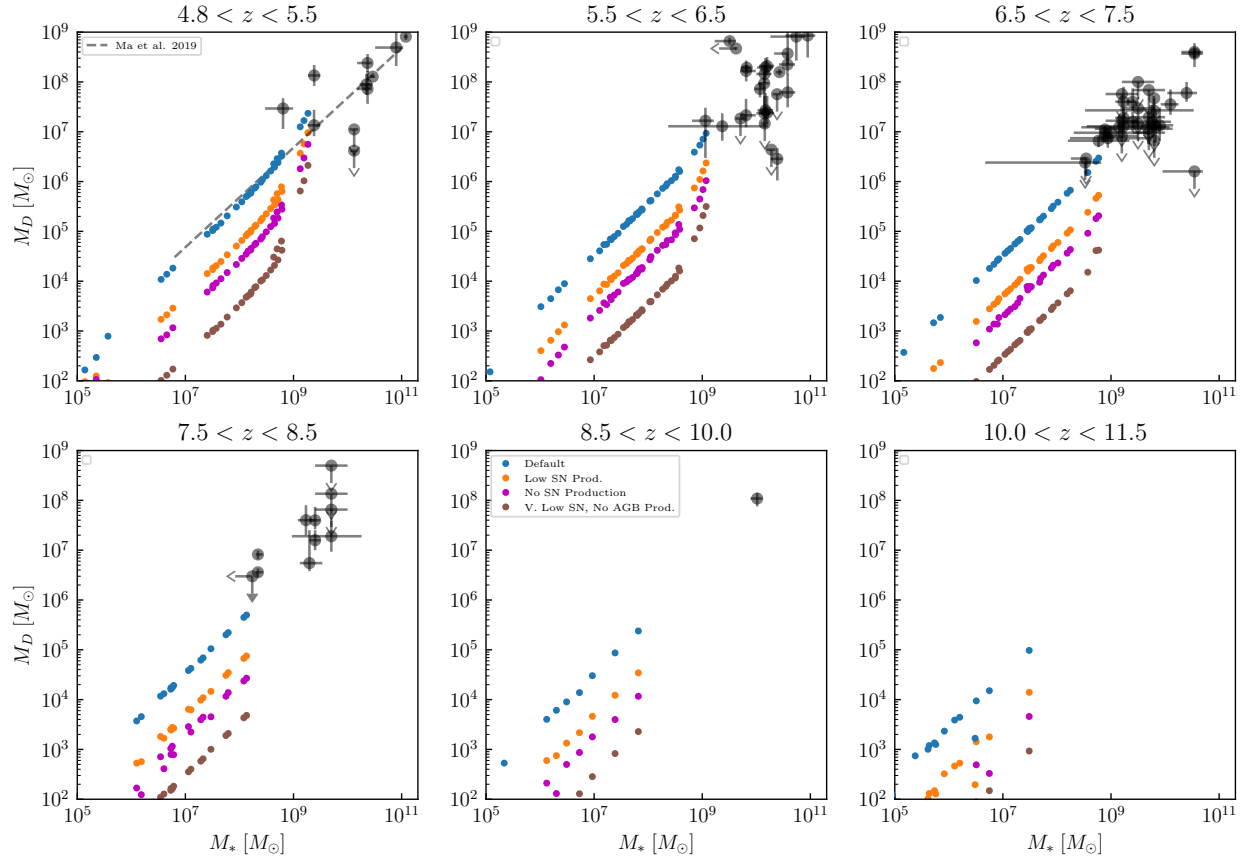


Figure 3.5: Dust-mass stellar-mass relation cont'd. Same as Fig. 3.4 but with **Default** and the dust models with varied yields (i.e. those in the third row shown in Fig. 3.3).

average metallicity, an effect not captured in simpler one-zone models [e.g. Feldmann, 2015]. For the **Default** and **Enhanced Accretion** models we notice substantial scatter in the metallicity at which each galaxy enters the growth-dominated regime of rising D/Z .

Indeed, we note that the most massive galaxy in our sample exhibits rising D/Z at high metallicities in all models except **No Accretion** (where $D/Z > y_D$ is physically impossible) and **Very Enhanced Destruction**. Even in the **Enhanced Destruction** scenario the D/Z ratio rises at late times (i.e. high metallicities) for this single galaxy but no others. This clearly indicates the importance of some combination of star formation history and ISM phase structure in setting the dominant dust regulating mechanisms. Precise determination of this cause would require more analysis beyond the scope of this work but would be interesting for future investigation.

Finally, we note that the significant scatter in D/Z at very low metallicities $Z \lesssim 10^{-4}$. As indicated by their redshift (indicated in color) and the stellar mass-metallicity relation in Figure 3.2, these low-metallicity galaxies are the highest-redshift and lowest-mass in our sample. Consequently, there are the most poorly-resolved and subject to the greatest stochasticity effects from the discreteness of enrichment from star particles and sampling by Lagrangian tracers. The latter would be amended by coupling the dust model explicitly to the simulation, and is therefore another motivation for more sophisticated modelling in future analyses. Nonetheless, this noise occurs at such low metallicities that its effect on the total dust mass, which is normalized by the metallicity, is minor and should not strongly impact our conclusions. As well, the existence of clear trends at late times/high metallicities indicates that the predictions are well resolved for the most massive galaxies, which are the most relevant for comparison to observational data.

In Figures 3.4 and 3.5 we examine the predicted dust masses of our simulated galaxies as a function of stellar mass at different redshifts for the different dust models. Figure 3.4 shows **Default** and models with variations in accretion and destruction rates (the first and

second rows of Figure 3.3), while Figure 3.5 shows models with varied production yields (third row of Figure 3.3. In all cases, the dust mass exhibits an approximately linear scaling with stellar mass, with varied normalization depending on assumed production yields and destruction efficiencies. This normalization spans two dex at a given stellar mass for the entire suite of models herein considered. There is also a general steepening of the relationship at higher masses ($M_* \sim 10^8 - 10^9 M_\odot$) in models where accretion becomes efficient. These relationships are sufficiently tight to be well-distinguished between different models in principle, although there is significant degeneracy between yield and destruction rates – **Very Enhanced Destruction** and **No SN Production** predict very similar values which the first achieves by destroying dust with high efficiency while the second produces little dust to begin with. As well, models with the same yield but different growth timescales (**Default**, **No Accretion**, **Enhanced Accretion**) are only distinguishable at high masses and late times, consistent with the results of Figure 3.3. In summary, different plausible parameter choices for the dust model can change dust masses by up to two orders of magnitude at a given stellar mass. This flexibility highlights the need for data to constrain the parameters.

We therefore compare these predictions with existing observational estimates of dust masses in high-redshift galaxies from Sommovigo et al. [2022], Dayal et al. [2022], Hashimoto et al. [2019], Knudsen et al. [2017], Schaerer et al. [2015], Watson et al. [2015], Laporte et al. [2017], Tamura et al. [2019], da Cunha et al. [2015], Marrone et al. [2018], Burgarella et al. [2020, with a redshift for ID27 from Aravena et al. [2016]], Pozzi et al. [2021, with stellar masses from Faisst et al. [2020]], Witstok et al. [2023], and Leńniewska and Michałowski [2019]. Because of the limited volume of our simulation, we do not capture unusually massive and therefore rare halos, limiting us to predictions at lower masses than almost all the existing data. Nonetheless, the data appear to favor those models with the highest dust masses – the data is always at the upper envelope of our simulation predictions wherever they overlap. Indeed, in both the $6.5 < z < 7.5$ and $7.5 < z < 8.5$ bins most of the data appear to lie

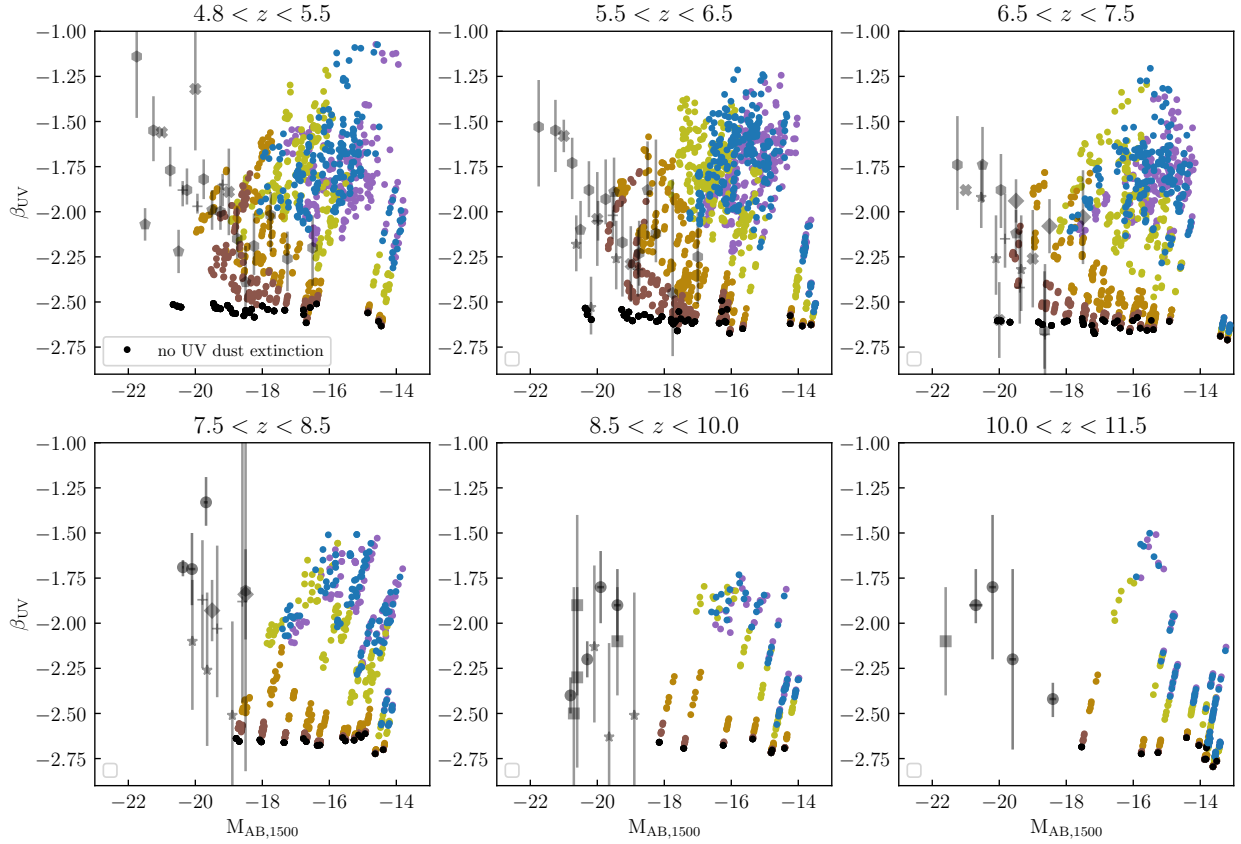


Figure 3.6: β_{UV} as a function of UV AB absolute magnitude. Different panels show data for different bins in redshift, different colors are different dust models, the black points indicate values predicted in the absence of dust, and the grey points are a compilation of observational measurements from the literature: Finkelstein et al. [2012, plus-signs], Bouwens et al. [2014, hexagons], Dunlop et al. [2013, diamonds], Bhatawdekar and Conselice [2021, stars], Wilkins et al. [2011, filled x], Dunlop et al. [2012, pentagons], and Wilkins et al. [2016, squares] show sample averages of multiple galaxies, while circles show measurements of individual galaxies with JWST from Roberts-Borsani et al. [2022a], Naidu et al. [2022b], Robertson et al. [2023], and Whitler et al. [2023].

on or above the scaling relation of the most dust-rich model **Enhanced Accretion** if it were extrapolated. This suggests that the data prefer models in which production yields are high and ISM grain growth is efficient at high masses. We also note that the data appear to exhibit greater scatter at a given stellar mass than any one set of dust model parameters predicts.

However, we emphasize that these conclusions are extremely tentative because of the minimal amount of data available for comparison, the mostly disjoint stellar mass ranges probed by our simulations vs. the observations, and especially the large systematic uncertainties in the observational constraints which are not captured in the statistical uncertainties on quoted errors: dust masses are derived from infrared luminosities, which depend on dust mass, the dust extinction coefficient, and strongly on the dust temperature. The latter two are highly uncertain in high redshift galaxies and difficult to independently constrain. Consequently, the most robust constraints will come from forward modelling of directly observable quantities.

3.3.3 Forward-Modeled Observable Quantities: Comparison to Data

For the remainder of our analysis we focus on a representative subset of the models discussed previously, each with a consistent color throughout the figures: **Default** (blue), **Enhanced Accretion** (purple), **Enhanced Destruction** (yellow), **Very Enhanced Destruction** (light brown), and **Very Low SN, No AGB Production** (dark brown).

Rest-Frame UV Observables: M_{AB} , β_{UV} , τ_{1500}

Figure 3.6 compares the predicted ultraviolet spectral slopes of our simulated galaxies with these dust models to observational data. We also show the predictions of the simulations absent dust extinction in black points. In contrast to the suggestions of Figures 3.4 and 3.5, the models with the lowest dust content – **Very Enhanced Destruction**, and **Very Low**

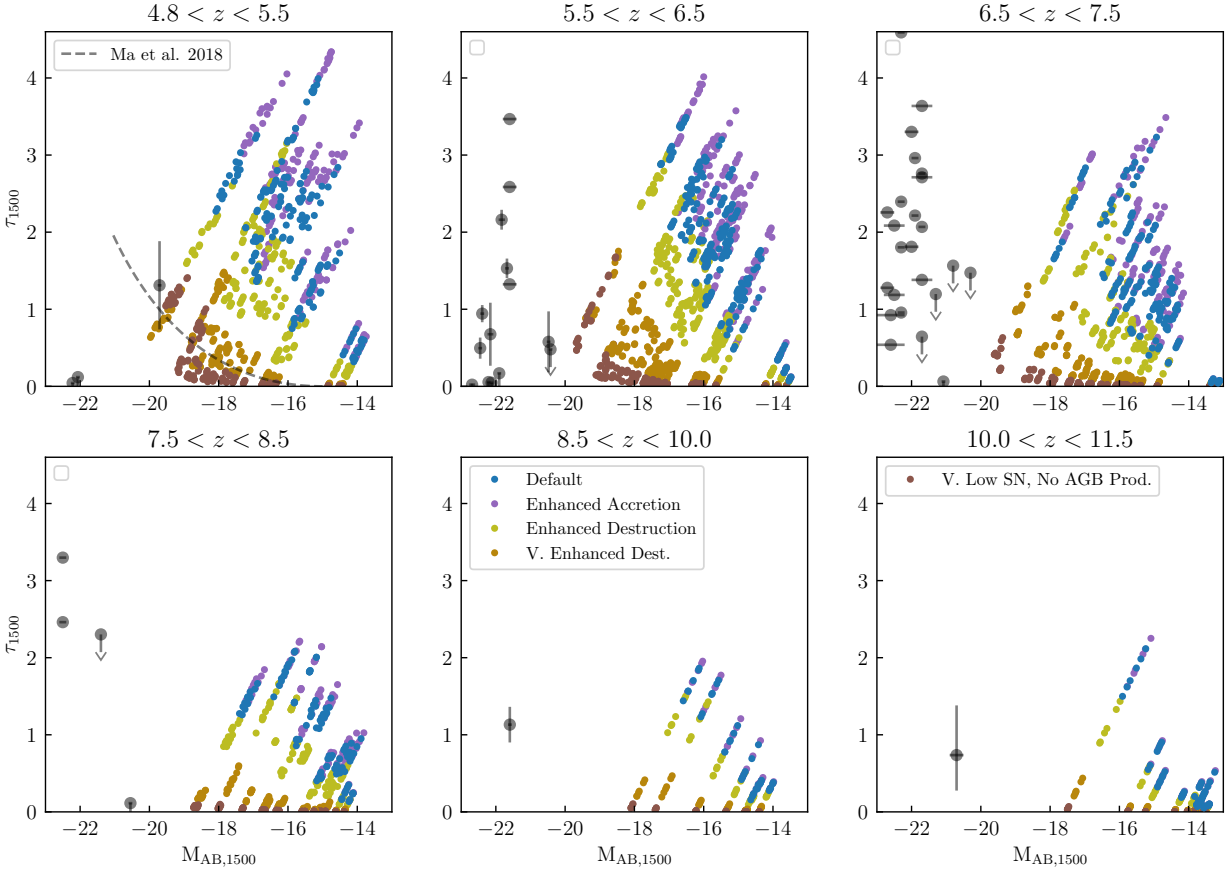


Figure 3.7: Dust optical depth in the UV vs. absolute UV magnitude. Observational upper constraints from Schaerer et al. [2015], Burgarella et al. [2020], Naidu et al. [2022b], and Ferrara et al. [2022, with absolute UV magnitudes taken from Bouwens et al. [2022b]] are shown. In the lowest redshift bin we also show the predictions from Ma et al. [2018] where high resolution galaxy simulations were post-processed with a simpler dust model. See the discussion for comparison.

SN, No AGB Production – agree best with the data, at all redshifts. It is not clear, however, if either model alone predicts as much scatter at a given luminosity as shown in the data.

In contrast, the more dust-rich models all predict similar β_{UV} values which fail to overlap with the observations at any redshift, and exhibit large scatter. This is because they predict very high ISM optical depths, as shown in Figure 3.7. For dust masses greater than or equal to those predicted by the **Enhanced Destruction** model, the dusty ISM is effectively opaque, so changes in dust content do not impact UV properties significantly. The scatter is then likely related – the comparatively fewer stars that are outside the dense ISM give rise to greater stochasticity in the observed UV properties. Finally, we note that while the data prefer the dust-poor models, they are inconsistent with entirely dust-free predictions, especially at later times.

Far-Infrared Observables: IRX- β Relation, L_{IR}

In Figure 3.8 we examine the IRX- β relationships predicted by our modeling, compared to observational constraints. Because infrared luminosity depends linearly on dust mass, models with distinctly different dust content are better separated in this parameter space. However, the predictions fail to match the data in two key ways: 1. No one model exhibits as much scatter as the observations, especially in the $5.5 < z < 6.5$ range, and 2. our simulations lack galaxies at low ($\lesssim 1$) IRX and high ($\gtrsim -1.5$) β_{UV} which are apparent in the data.

Some of the reason for these disagreements is illuminated by examining the predictions in L_{IR} vs. L_{UV} space, since these are the numerator and denominator of the IRX, respectively. This is shown in Figure 3.9, along with the same data as in Figure 3.8. While we predict reasonable L_{IR} especially at late times, all of the galaxies in this observational sample exhibit higher UV luminosities than ours. This helps to explain the lack of low IRX galaxies in

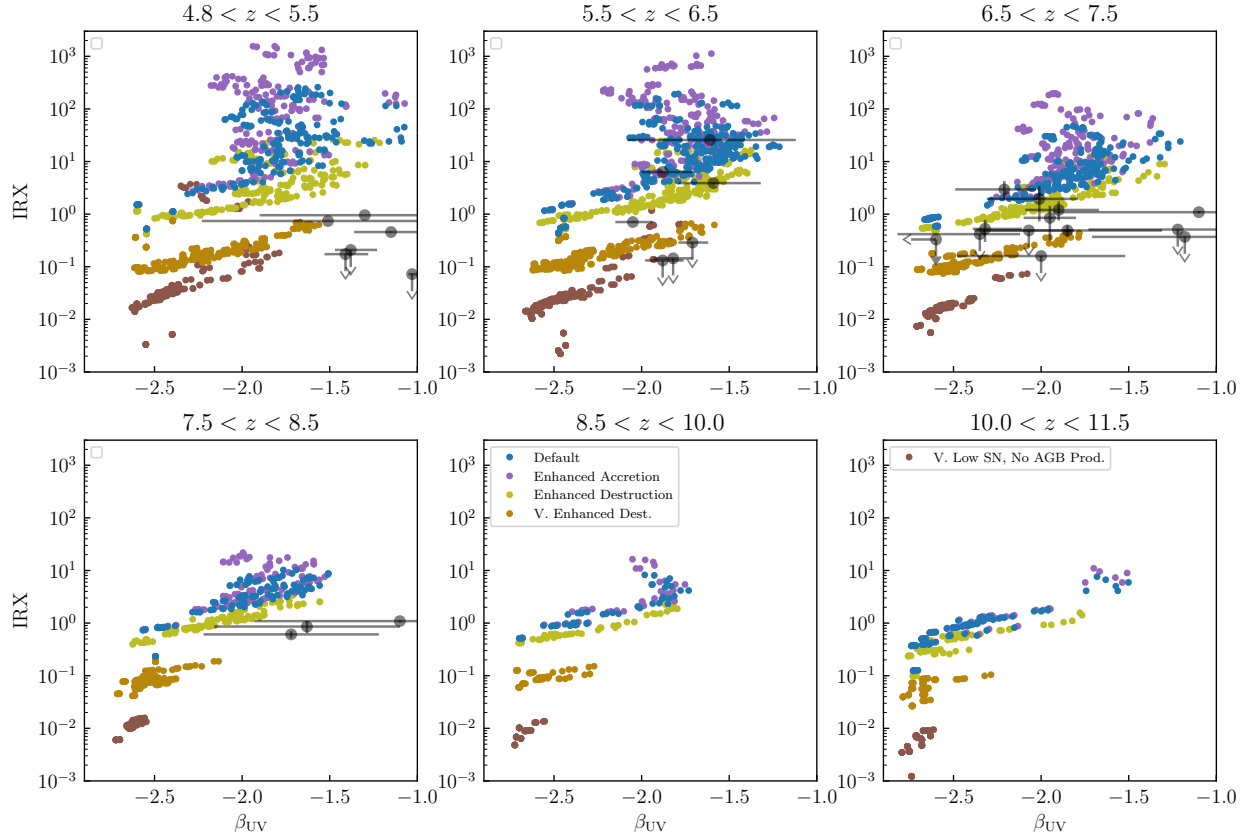


Figure 3.8: IRX- β_{UV} relation. Infrared-Excess (IRX) vs. ultraviolet spectral slope β_{UV} for our simulated galaxies in each dust model. Note that a constant dust temperature of $T_D = 40K$ was assumed in calculating all infrared luminosities. The colors and redshift bins are identical to Fig. 3.6. Data shown are from Barisic et al. [2017] [which includes data from Capak et al., 2015, Pavesi et al., 2016], the compilation from Hashimoto et al. [2019], and Bowler et al. [2022].

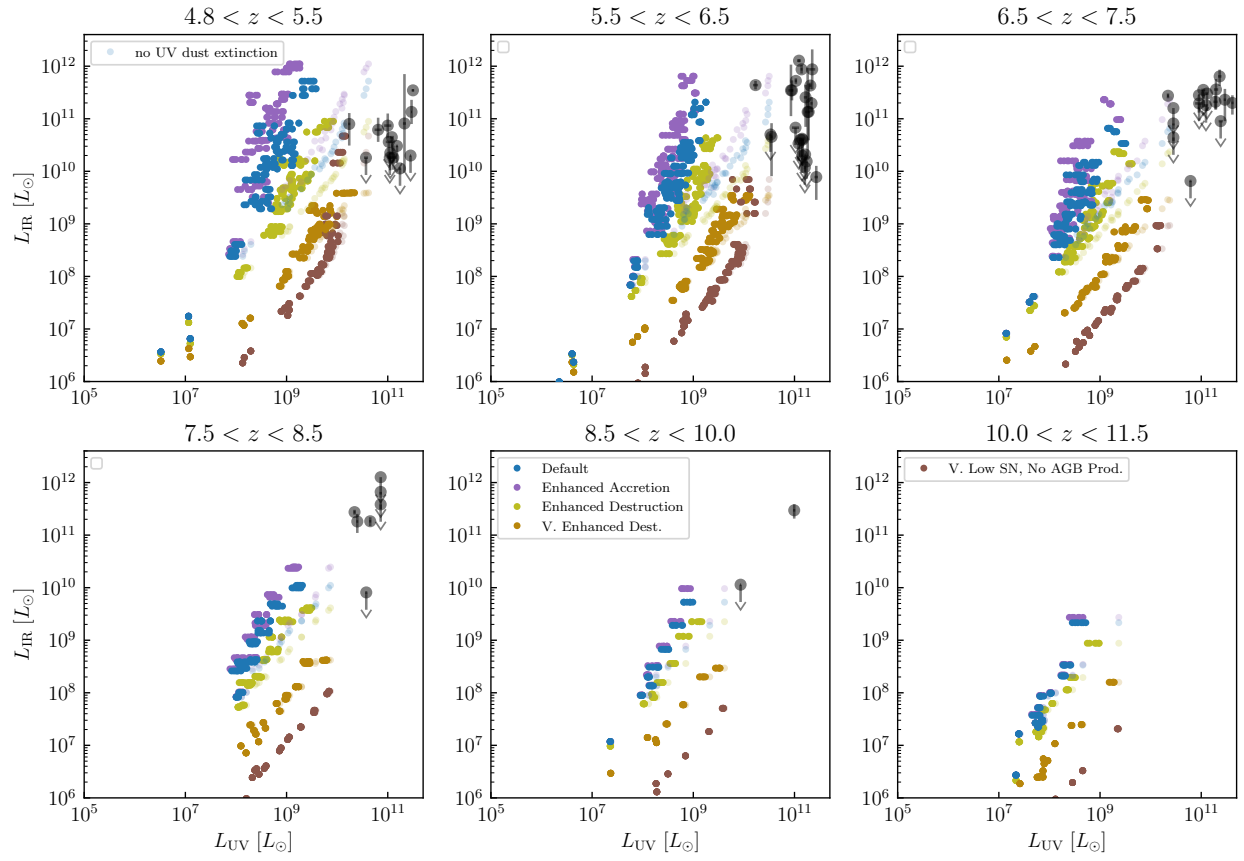


Figure 3.9: Infrared luminosity vs. UV luminosity. Colors and observational data are the same as Figure 3.8, with the addition of data from Burgarella et al. [2020]. Additionally, we show predictions without UV dust attenuation in transparent points. These are inconsistent with the simulation, but show the effect of reduced UV opacity with unchanged dust mass.

our predictions. This suggests that our models are predicting dust masses consistent with observations, but opacities that are too high, in agreement with the interpretations of Figures 3.4, 3.5 and 3.6. Indeed, in Figure 3.9 we show the predictions of our simulations without dust attenuation as transparent points, and they are in better agreement with the data. This experiment is nonphysical in that the two luminosities are inconsistently calculated. However, it suggests that real galaxies have similar dust content to our more dust-rich models, but that it is distributed so as to have a much lower effective optical depth.

The inability of any one dust model to reproduce the scatter in observed infrared luminosities could be due to our lack of self-consistently calculated dust temperatures – for simplicity and given the large modelling uncertainties involved, we assume a constant dust temperature of $T = 40\text{K}$ for these calculations [see Sommovigo et al., 2022]. Since $L_{\text{IR}} \propto T_D^4$ at fixed M_D , galaxy-galaxy scatter in T_D could significantly enhance the predicted range of IRX. As well, the lack of very massive galaxies in the limited cosmological volume of our simulation might also mean that we simply aren't sampling galaxies as massive as those in existing observational samples, and this may also be the cause of one or both of these discrepancies to some degree.

It is of course also possible that the dust dynamical quantities assumed as inputs into each model, such as the characteristic time for dust grain growth in the ISM or the supernova destruction efficiency – vary from galaxy to galaxy due to differences in ISM phase structure and dust content that our model is not sophisticated enough to capture. Infrared observables will therefore require significantly further theoretical efforts to be used as constraints on dust physics at high redshift.

3.4 Discussion

3.4.1 *Status of Dust Constraints*

We begin the discussion by assessing the success of our dust modeling efforts compared to current empirical constraints. There is no one model which appears to agree with all of the existing data. While the infrared luminosities (and therefore estimated dust masses) appear to be best reproduced by models with comparatively higher dust content from high production yields and efficient growth, the models with the lowest dust content are in best agreement with β_{UV} constraints. We also note that none of our dust models reproduces individually reproduces the scatter in L_{IR} seen in observations, which could be due to either the limited halo mass range of our simulation sample, the assumption of a fixed dust temperature for all galaxies, or the simplicity of our dust model. Together, these results suggest that while our model is capable of producing dust masses similar to those of real early-universe galaxies, doing so results in UV opacities that are too high. We speculate that this could be due to the spatial distribution of dust relative to stars – that our galaxies are too uniform compared to the very turbulent ISM of real reionization-era galaxies. We explore the spatial distributions predicted by our dust models in the following Chapter.

3.4.2 *Comparison to Similar Theoretical Work*

Lewis et al. [2023] recently presented results of an investigation with similar aims: they coupled an explicit model for dust very similar to ours to a galaxy formation simulation of cosmological reionization, and use this to predict the dust content and rest-frame UV observables of high redshift galaxies. They present predictions for a single choice of dust model parameters, in which they assume very low dust production yield $y_D = 10^{-3}$ and a much higher ISM growth accretion rate – they adopt a modestly shorter characteristic timescale (100 vs 300 Myr) and the expression has an additional factor of $1/Z \sim 10^3 - 10^4$.

Consequently their galaxies transition from production-dominated to accretion-dominated dust content at a lower galaxy stellar mass of roughly $10^6 M_\odot$ in contrast to $\gtrsim 10^7 M_\odot$ in all of our models.

Their dust masses are therefore most similar to our highest-dust-content models. However, their model predicts much milder UV dust attenuation than ours with similar dust masses, see their Figure 7. We speculate that this is due to differences in resolution: their maximum physical resolution is an order-of-magnitude poorer than ours, at ~ 1 kpc. Given the observed sizes of high redshift galaxies are $\lesssim 1$ kpc Bouwens et al. [2020], their galaxies cannot possibly be spatially resolved and are therefore likely artificially large. This spreads the same amount of dust over a larger surface area and consequently reduces their predicted optical depths.

Graziani et al. [2020] also recently conducted simulations of high-redshift galaxies with a coupled dust physics model. Again, they only present predictions for a single set of dust model parameters, which appear to make qualitatively similar predictions between our **Default** and **Enhanced Accretion** models: their Figure 4 indicates a production yield of $y_D \sim 0.1$, and a transition to accretion-dominated dust at $Z \sim 3 \times 10^{-2} Z_\odot \sim 6 \times 10^{-4}$. We note however that they adopt both a much shorter characteristic timescale of 2 Myr to our 300, and a somewhat different accretion rate scaling of $\dot{D} \propto DZ$ as opposed to our $\dot{D} \propto D(f^{\text{dep}}Z - D)$. The two expressions tend to the same value at low D (modulo f^{dep} factor which is order-unity), but will differ significantly at higher D – while ours will tend to zero as $D \rightarrow Z$, corresponding physically to all the available metals being locked in dust grains, theirs increases unbounded. This suggests that the plateau in D/Z at ≈ 0.4 with increasing Z exhibited by their model is due to enhanced destruction rates which regulate the dust content, whereas in our model the transition is set by the $Z - D$ term in the growth rate going to zero.

Moreover, the fact that their model transitions to accretion-dominated at similar Z to

ours despite a much higher growth-rate normalization suggests significant differences in the cold gas fractions or thermodynamics of the ISM in our simulations. We also note that their simulation accounts for dust dynamical effects at run time, which our post-processing model cannot. All of this suggests that 1. the predictions of these dust models are sensitive to the implementation details of cooling, star formation, and feedback in the ISM of high redshift galaxies, and/or 2. that the back-reaction of dust dynamics on the ISM might be significant.

We also consider recent analyses that predict the dust content of high-redshift galaxies with simpler post-processing physical dust models, but with much higher-resolution ($\sim 10\text{pc}$) simulations that can more realistically resolve ISM dynamics and phase structure. Ma et al. [2018, 2019] predict dust-sensitive quantities from high resolution simulations from the FIRE project [Hopkins et al., 2018] of galaxies at $z \geq 5$ by assuming a constant $D/Z = 0.4$. While their analysis predict similar dust masses to our more dust-rich models – see the dashed grey line in Figure 3.4, their predicted effective optical depths are most consistent with our least dusty models (see Figure 3.7). Interestingly, this is also the case with the results from a similar study [Mushtaq et al., 2023] using the FirstLight simulation suite [Ceverino et al., 2017] and an identical dust post-processing model – see Figures 1 and 5 in Mushtaq et al. [2023].

FIRE and FirstLight are different galaxy formation simulations of similarly high resolution, both significantly higher than ours. Consequently, they better capture the effects of feedback on the high-redshift interstellar medium, resulting in a more turbulent, porous gas distribution which we speculate has a broader column density distribution than ours – see Figure 4 of Ma et al. [2019] and Figure 1 of Ceverino et al. [2021], both of which exhibit large gas column density fluctuations on scales smaller than our 100 pc resolution. This results in lower effective optical depths at a given dust mass because there exist low-density column channels through which UV radiation can escape that are lacking in our simulation. We explore the spatial distribution of dust predicted in our models in Chapter 3.

3.5 Conclusion

We apply the dust post-processing model described in Esmerian and Gnedin [2022] to a suite of 11 simulated galaxies from the CROC project. We explore 9 different sets of dust parameters and quantify the effect of their variation on the dust content of high redshift galaxies. We then forward model observable properties of high-redshift galaxies and compare to existing data. Our conclusions are the following:

- Comparing our simulated galaxies to a compilation of recent constraints on the metallicities of reionization-era systems, we find general agreement, although CROC might slightly under-predict metallicity at a given stellar mass.
- We vary dust model parameters governing the rate of grain growth due to accretion in the ISM, the efficiency of grain destruction in supernova remnants, and the dust yields of production sources (supernova and AGB star winds), to determine their impact on the predicted dust contents of high-redshift galaxies. We qualitatively validate the results of Esmerian and Gnedin [2022]: the dust content of galaxies is set at early times/low metallicities primarily by the assumed production yields, while at higher metallicities/late times it is set by the competition between accretion and destruction, normalized by the initial condition set by production yields. The transition occurs around $Z \sim 2 - 4 \times 10^{-4} = 1 - 2 \times 10^{-2} Z_{\odot}$, with some dependence on assumed model parameters.
- However, we observe significant scatter between galaxies at a constant metallicity, especially at late times/higher metallicities for models in which growth via accretion becomes efficient. This indicates the existence of important secondary dependencies beyond metallicity that determine the dust content of galaxies, which is not captured by typical one-zone models [Feldmann, 2015, e.g.]. We speculate that this is driven by some combination of star formation history and ISM phase structure dependence,

evidenced by the particularly aggressive growth via accretion in the most massive galaxy compared to the other galaxies in our sample.

- We compare our total predicted dust masses as a function of stellar mass to observational constraints in the literature, and while our limited simulation size fails to sample galaxies as massive as most of those with observational constraints, where there is overlap we find our most dust-rich models – **Default** and **Enhanced Accretion** – appear to predict scaling relations consistent with current data. This suggests that the data prefer models in which production yields are high and ISM grain growth is efficient at high masses. The data also appear to exhibit larger scatter at a given stellar mass than predicted by any one of our models, but due to both large systematic uncertainties in the dust mass observational constraints and the disjoint range of stellar masses probed by our simulations vs. the observations, these conclusions are tentative.
- We forward model directly observable galaxy properties from our simulations to make more direct comparison to data, and find that we are unable to simultaneously match existing observational constraints with any one model. Specifically, the models which best match the observed spectral slope in the UV, β_{UV} , are the models with least dust content due to either low production yields or very high destruction rates. However, these models fail to predict sufficiently high infrared luminosities. Those that do predict IR luminosities consistent with observations have far too much dust extinction and thereby fail to agree with β_{UV} constraints. Finally, we note that no one of our models appears to predict as much scatter in these observable quantities as the data exhibit.
- We speculate that these deficiencies in our modelling are due to the inability of our galaxy formation model to capture the dynamics of the high-redshift ISM, causing it to predict gas distributions that are overly smooth. Likely, significantly higher-resolution simulations are needed to make progress on constraining the properties of

dust in reionization-era galaxies. Improved empirical constraints, especially for lower mass galaxies, will also be crucially informative.

CHAPTER 4

ANALYSIS OF THE PREDICTED SPATIAL DISTRIBUTION OF ULTRAVIOLET EMISSION, INFRARED EMISSION, AND ULTRAVIOLET COLOR

4.1 Introduction

To better understand the predictions of our dust models, and present a complete comparison to current data, we analyze the relative spatial distribution of stars and dust as probed by infrared (IR) and ultraviolet (UV) emission, as well as UV colors. This analysis is motivated by recent high-resolution observations of galaxies in the epoch of reionization which are beginning to spatially resolve their stellar and ISM components [e.g. Le Fèvre et al., 2020, Bouwens et al., 2022b, Bowler et al., 2022].

One particularly interesting finding of these programs which our models are uniquely poised to address is the prevalence of significant spatial offsets between locations of peak rest-frame optical/UV and IR emission in high redshift massive galaxies [Willott et al., 2015, Maiolino et al., 2015, Carniani et al., 2017, Le Fèvre et al., 2020, Bowler et al., 2022, Inami et al., 2022]. Excitingly, Bowler et al. [2022] has also reported rest-frame UV color gradients that appear aligned with these offsets. The relative morphology of these two components potentially provides information as to the fraction of starlight and star formation which is obscured by dust, the physical conditions and phase structure of the ISM of high-redshift galaxies, and the physical processes that shape their dust content and distribution.

Our analysis focuses on the sample from Inami et al. [2022], the largest to date. It contains galaxies with such offsets at $6.5 < z < 8.5$ with stellar masses $8.5 \lesssim \log_{10}(M_*/M_\odot) \lesssim 10$, gas masses $9.5 \lesssim \log_{10}(M_*/M_\odot) \lesssim 11$ and star formation rates $15 \lesssim \text{SFR}/(M_\odot \text{yr}^{-1}) \lesssim 200$. The magnitudes of these offsets have not been shown to correlate with any of these properties, though this may be due to the small sample size of existing data. We note that all galaxies

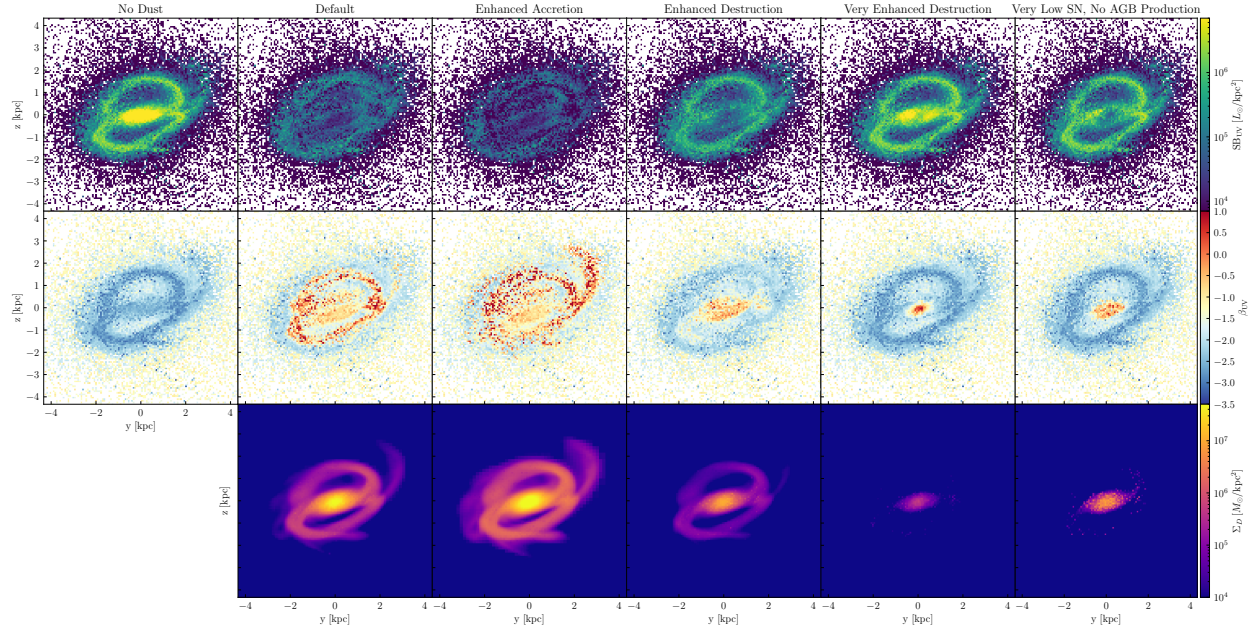


Figure 4.1: Images of the most massive galaxy in our box at $z = 5$ with different dust models. The top row shows the 1500\AA UV surface brightness, the middle row shows the spatially resolved UV beta slope (estimated using the 1500\AA and 2500\AA color) and bottom row shows the column density of dust mass (which is proportional to the IR surface brightness in the optically thin regime). Each column shows the predictions of a different set of dust model parameters, as well as the intrinsic UV emission on the leftmost column. Note that no smoothing has been applied to these images, and the pixelation is the result of the simulation grid

considered in this study were selected as targets for radio observation based on their rest-frame UV luminosity. This survey is therefore possibly biased to systems with the highest star formation rates (SFRs), and would miss systems of similar mass with lower SFR, or the same SFR if they were too heavily obscured. Nonetheless, these state-of-the-art data may provide unique constraints on our modelling because of their spatially resolved nature, motivating comparison.

4.2 Methods

We use the simulations and dust models presented in the previous chapter. We focus exclusively on the most massive galaxy in the simulation which attains a stellar mass of

$M_* = 1.3 \times 10^8 M_\odot$ by $z = 8$, $M_* = 7.1 \times 10^8 M_\odot$ by $z = 6.4$ and $M_* = 1.9 \times 10^9 M_\odot$ by $z = 5$. Our simulated galaxy is therefore well within the range of stellar masses probed by observations, justifying comparison because galaxy morphology is expected to depend on stellar mass [Pillepich et al., 2019]. However, we note that for these snapshots it has a much lower SFR of $\leq 5.2 M_\odot/\text{yr}$ than any galaxy in the observational sample. This may be due to the bias towards high SFR systems of these observations noted in the introduction, or the inability of the CROC model to produce such rapidly star-forming systems. Figure 6 of Zhu et al. [2020] shows that the CROC galaxies exhibit small scatter in the SFR-stellar mass relationship, suggesting that the discrepancy between our simulation’s SFR and those inferred from data results from a deficiency of the model and would not be alleviated by considering a larger number of simulated galaxies. This discrepancy provides further motivation to compare our simulations to data in a spatially resolved analysis as this may provide information about the cause of these discrepancies.

We present results for this simulation at 12 snapshots from $z = 8.5$ to $z = 5$. The upper bound in redshift is motivated by the upper bound on the observations, but we include snapshots lower than the observational lower bound of $z = 6.5$ to maximize the galaxy mass range probed by our analysis. We note that we have redone the analysis restricted to only snapshots within $6.4 < z < 8.5$, identical to the observations, and all of our conclusions are unchanged. We also note that based on visual inspection, the galaxy undergoes merging events at $z \approx 7.3$ and $z \approx 6$ which significantly disrupt its morphology. There are enough snapshots of the simulation that the galaxy morphology before, during, and after the merger event can be clearly distinguished. We therefore expect that our simulation data samples a sufficiently violent merger history with sufficiently high time resolution that our analysis accounts for the morphological effects of accretion history on high-redshift galaxies of the relevant masses.

We calculate ultraviolet emission as described in the first chapter, to which we refer

the reader, but we summarize here for convenience. Star particles are treated as single-age, single-metallicity stellar populations, and their spectra are calculated with the Flexible Stellar Population Synthesis code [Conroy and Gunn, 2010]. The spectrum of each star particle is then attenuated by $e^{-\tau}$ where τ is the optical depth due to intervening dust along a given line-of-sight using the wavelength-dependent dust opacity from the “SMC bar” model of Weingartner and Draine [2001], Draine et al. [2007]. We note that this procedure does not account for the effects of light scattered into the line-of-sight, but we expect this effect to be negligible and (in the case of our simulations) possibly unrealistic due to the unrealistically spatially smooth dust distribution because of simulation resolution.

UV quantities are calculated along 6 lines of sight corresponding to the positive and negative coordinate axes so as to sample the effect of different viewing angles on the same galaxy. UV colors are determined based on the finite difference between luminosities at 1500Å and 2500Å as follows

$$\beta_{\text{UV}} = \frac{\log_{10}(f_{2500\text{\AA}}/f_{1500\text{\AA}})}{\log_{10}(2500\text{\AA}/1500\text{\AA})} \quad (4.1)$$

again on an individual star particle basis. We note that this is not identical to the calculation of β_{UV} in the previous chapters, in which a least-squares fit performed on this portion of the UV spectrum to determine a power-law slope. This finite difference method is adopted for computational ease, and we have checked that it reproduces the least-squares fitting results very accurately.

We use dust column density Σ_D , computed from the galaxy dust mass distribution calculation described in Chapter 1, as a proxy for infrared continuum emission. The two are directly proportional because the dust distribution is optically thin in the infrared.

To account for the effect of finite observational resolution, we smooth with a Gaussian kernel with variance $\sigma^2 = \frac{\Delta x_{\text{FWHM}}^2}{8 \ln 2}$ where Δx_{FWHM} is the physical distance at the simulation snapshot redshift corresponding to the angular Full-Width Half-Max (FWHM) of

the observation. We explore Δx_{FWHM} values of 0.2 and 0.8 arcsec, which for the redshift range of our simulations $11.4 \geq z \geq 5.0$ corresponds to a physical size of 0.33 – 0.55kpc and 1.32 – 2.19kpc, respectively.

4.3 Results

Figure 4.1 shows the predicted UV (1500Å), UV color β_{UV} , and dust column density (which is proportional to the IR emission) for different dust models. Consistent with the results of Chapter 2, all of our dust models predict significant extinction and reddening, but the amount and spatial distribution vary markedly between the different models. The most dust-rich models show large amounts of reddening and extinction throughout the galactic disk, while those with less dust have effects that are more centrally concentrated. However, even those models with the least dust exhibit substantial attenuation and reddening in the center. This is because even the **Very Enhanced Destruction** model predicts dust column densities in excess of $\Sigma_D = 10^5 M_{\odot}/\text{kpc}^2 \approx 10^{-5} \text{g}/\text{cm}^2$ which, for our assumed dust opacity which is $\approx 10^5 \text{cm}^2/\text{g}$ at 1500Å results in unity optical depth, and $\beta \gtrsim 0$ colors. The increasing severity of extinction at smaller projected galactocentric radii gives the UV emission a ring-like morphology in all but the least dusty model. Color is strongly correlated with IR emission though not perfectly – for example, both Default and Enhanced Accretion models exhibit reddest colors in the disk outskirts / tidal tails, while the IR emission is highest in the center.

All but the **Very Enhanced Destruction** dust model show offsets in the location of maximum UV and IR emission on the order of 1 kpc for the same reason: the regions of highest IR emission are totally opaque to UV light. Note that this is despite the fact that the unattenuated UV light and dust are largely co-spatial. Figure 4.2 shows the measured offsets in projected distance between locations of maximum UV and IR brightness for the same models, at all simulated redshifts, sampling 6 lines-of-sight per snapshot. The top

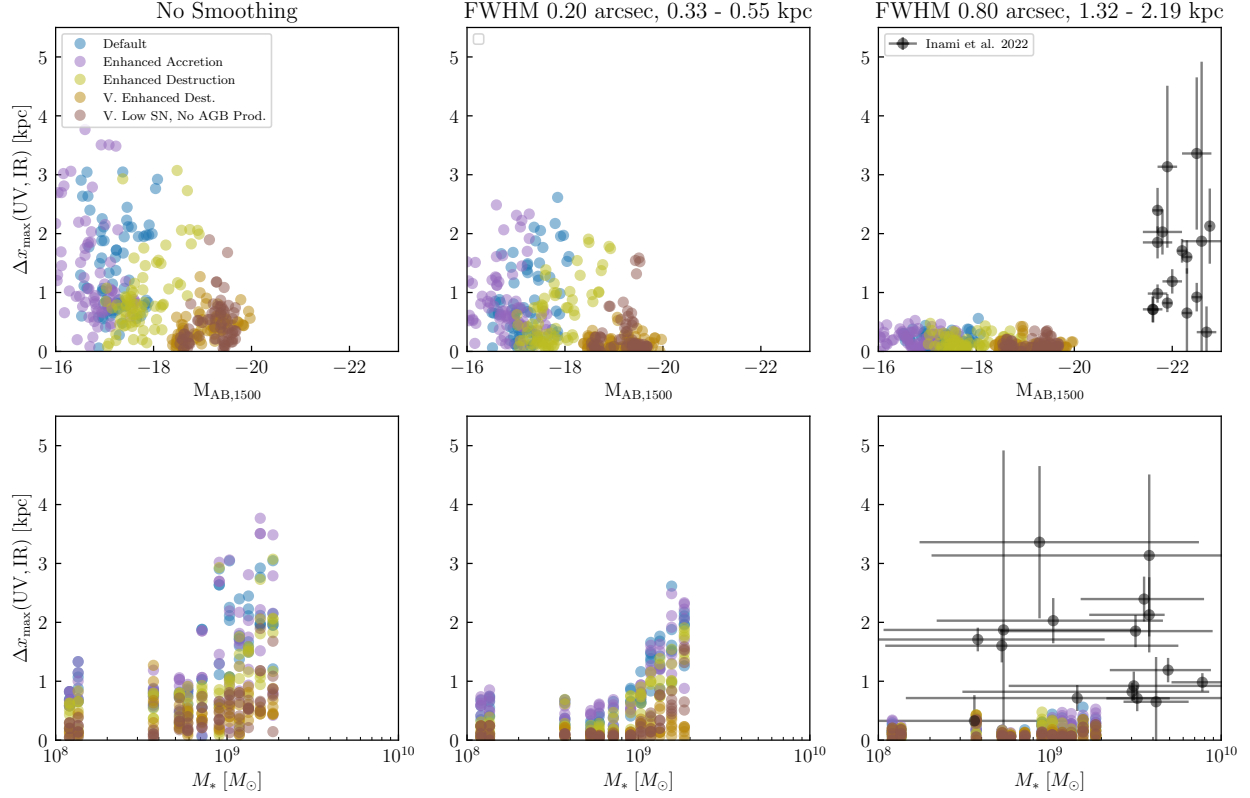


Figure 4.2: UV and IR peak emission offsets. The projected physical distance between the maximum UV emission (accounting for dust attenuation) and the maximum IR emission (as determined by the dust surface density), as a function of UV absolute magnitude (top row) and stellar mass (bottom row). Each point is one of six lines-of-sight for a each snapshot. Data for the most massive galaxy in our box $5 < z < 8.5$ is shown. Different colors correspond to different dust models. Each panel shows different levels of smoothing to capture the effect of observational resolution. Data on the right-most plot are from Table 4 of Inami et al. [2022, with stellar masses from Bouwens et al. [2022b] and Schouws et al. [2022]], whose observations have approximately 0.8 arcsecond resolution in both the IR and UV [McCracken et al., 2012].

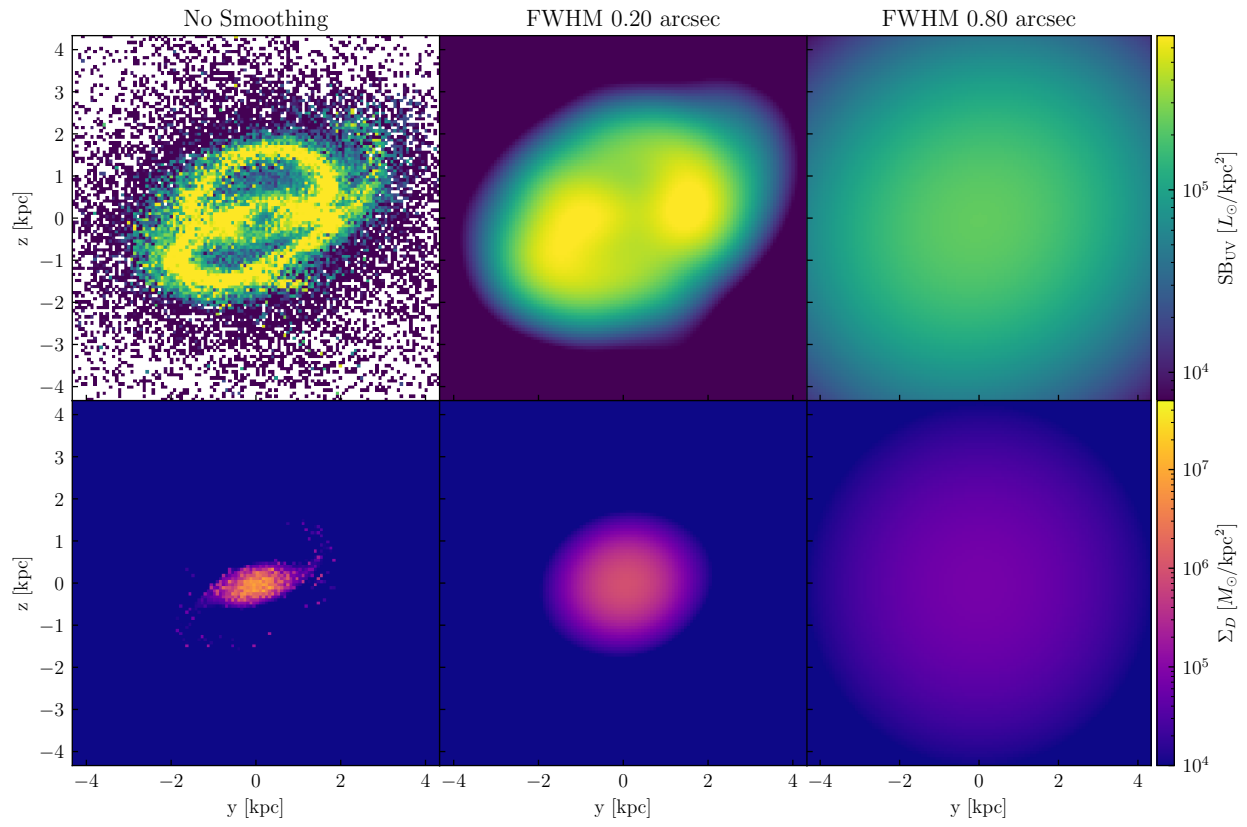


Figure 4.3: Effect of observation resolution on UV and IR morphologies.

panels show these offsets as a function of absolute UV magnitude, on the bottom panels as a function of stellar mass. The left-most panel of this figure is consistent with the trends noticed in Figure 4.1. Larger dust masses result in larger projected regions in which the dust is totally opaque to UV light. The maximum UV emission thereby happens at the larger projected radii where dust becomes optically thin, while the peak IR emission is always in the galactic center.

The middle and right panels show the results for the same images smoothed by a Gaussian beam of FWHM 0.2 and 0.8 arcseconds, respectively. The physical scale of the smoothing therefore depends on the snapshot redshift, and corresponds to 0.33 (1.32) kpc at $z = 11.4$ and 0.55 (2.19) kpc at $z = 5$ for a FWHM of 0.02 (0.08) respectively. The numbers were chosen to approximately match the resolutions of space-telescope (such as HST or JWST) observations and ground-based (e.g. ALMA and UltraVISTA) observations, respectively. On the right-most panel we show data from Inami et al. [2022] of UV-bright $z \sim 6 - 7$ galaxies for which dust continua was observed with ALMA and rest-frame UV (observation-frame near-IR) was observed as part of the UltraVISTA survey, both of which have approximately 0.8 arsec FWHM resolution [McCracken et al., 2012]. While these galaxies are clearly much brighter in the UV than ours, some exhibit very large UV-IR offsets that our simulated galaxy fails to exhibit when smoothed appropriately for comparison.

Indeed, we see that increased smoothing monotonically reduces the peak emission offset. Figure 4.3 demonstrates why: the angular symmetry of both the stellar and dust distributions result in a ring-like morphology of the UV emission at projected galactocentric distances where the dust becomes optically thin. While the offset of UV and IR maxima at infinite observational resolution is approximately the radius of this ring, at smoothing scales comparable to this radius the UV light is maximized in the center, co-spatial with the peak IR emission. The fact that this holds true for all sightlines in all snapshots for every dust model indicates that the UV-IR morphologies are similar in all cases. Peak UV and IR emission

are never asymmetrically offset in a way that is preserved with degrading resolution. We have confirmed with a visual inspection of all snapshots that these conclusions are generic to our simulation at all relevant cosmological times. This generality leads us to strongly suspect that it would hold for higher-mass galaxies simulated with CROC physics and our dust model. This is especially the case since more massive galaxies would be expected to have greater dust masses (see Figures 3.5 and 3.6).

4.4 Discussion and Conclusion

We have conducted an analysis of the predicted UV, IR and UV color morphology of the most massive galaxy in our simulation under the assumption of different dust model parameters. We find that all models predict significant dust attenuation in the central region of the galaxy, resulting in red $\beta \gtrsim -1$ colors and in all but the model with the least dust ring-like morphology for the UV emission. This is because the dust contents predicted by our models are generally optically thick in a region that is approximately symmetrical about the galactic center, so the UV emission is dominated by the smallest radii at which dust becomes optically thin. Color is also strongly correlated with dust column, which we use as a proxy for IR emission.

Since IR emission peaks in the center of the galaxy, there are \sim kpc-scale offsets between the points of maximal UV and IR surface brightness when “observed” with infinite resolution, but degrading image resolution on scales similar to existing observational capabilities causes the UV emission to peak in the center due to its symmetric distribution, resulting in no offset between peak brightness in UV and IR. While existing observations only probe galaxies brighter in the UV than the most massive in our sample, they do exhibit much larger offsets that are suggestive of more complicated morphologies than the ones predicted by our modeling efforts, see Figure 2 of Bowler et al. [2022] and Figure 7 of Inami et al. [2022]. Indeed, Figure 3 of Bowler et al. [2022] displays UV color gradients much less symmetric

than any of those predicted by our dust modelling.

We note that the analysis of the 3rd chapter would lead us to expect that the distributions of UV and IR emission predicted by our models would be overly smooth and symmetrical, given our inability to simultaneously match observed dust masses and optical depths. We interpreted this as evidence that our simulations fail to reproduce a sufficiently dynamic ISM and consequently the full distribution of dust column densities, the lower tail of which could allow for significantly enhanced UV emission without decreased dust mass. The results of this chapter provide evidence in favor of this interpretation given the inability of our modelling to reproduce the asymmetric morphologies seen in data of galaxies with similar stellar masses.

Simulation resolution and feedback prescription are the two most important numerical components of a fluid-dynamical galaxy formation model for determining the structure and dynamics of the ISM, and therefore one or both of these is likely implicated in our modelling failures. At a spatial resolution of 100pc, our simulations do not resolve the disk scale-height and therefore cannot capture fully three-dimensional structures that characterize the ISM phase structure like molecular clouds and supernova feedback “super-bubbles”. As a consequence, the delayed cooling feedback prescription utilized in CROC appears to be incapable of driving large-scale galactic winds – we have watched movies of the tracer particles used in this analysis and they are never removed from the galaxy ISM, indicating a negligible mass flux from the ISM into the circumgalactic medium. This is in stark contrast to most other modern galaxy formation models in which galaxies of the relevant mass range drive strongly mass-loaded winds, especially at early cosmological times [e.g. Muratov et al., 2015, Pandya et al., 2021]. A feedback prescription that successfully launches winds would reduce the gas mass and therefore dust mass in our galaxies, possibly reducing the high opacities of our most dust-rich models. These winds might also carve out low column density sight-lines with minimal dust extinction.

Ma et al. [2018], Ma et al. [2019], and Liang et al. [2021] thoroughly explored the UV-to-

IR observable properties of reionization era galaxies predicted by the FIRE-2 simulations, which are significantly higher resolution than ours ($\sim 10\text{pc}$) and have been demonstrated to drive galactic winds. While they do not explicitly quantify any offsets between predicted UV and IR emission in their simulations, we see suggestions from their analysis of the dynamic, asymmetric ISM seen in observations and lacking in our simulations. Figure 4 of Ma et al. [2019] shows images of UV light and dust column density for two of their simulated galaxies, which both display a much more disturbed morphology than anything we find in our analysis. Close inspection reveals that the regions of brightest UV surface brightness correspond to holes in the dust surface density which appear to be blown out by strong feedback. However, we note that the spatial offsets between peak UV and IR emission do not visually appear to be much larger than 1 kpc, but firm conclusions cannot be drawn from images of just two galaxies each at a single snapshot. Figure 12 of Liang et al. [2021] does explicitly show a galaxy with $> 1\text{kpc}$ offset between maximum UV and IR surface brightness, due to a highly perturbed and asymmetric distribution of gas with respect to stars (though we note that this galaxy is significantly more massive than those in our analysis). They also find that the effective UV optical depth does not correlate with dust mass at all at high redshift $z = 6$ because of large variations in the star-dust geometry predicted by their simulations. All of this suggests that higher resolution simulations with a feedback model that drives galactic winds may be better able to match the asymmetric UV/IR morphologies seen in observations.

The SERRA project is another suite of high-resolution cosmological simulations of galaxies at $z > 6$. These simulations are higher resolution than ours by about a factor of 3 with minimum cell sizes of $\sim 30\text{pc}$, and consequently have different star formation and feedback prescriptions, more similar to those in FIRE-2 [Behrens et al., 2018, Pallottini et al., 2022]. In contrast to our work and similar to FIRE, they find a clumpy morphology for both stars and dust, which in some cases leads to spatial offsets [Pallottini et al., 2022]. They also find

that this clumpiness results in low effective optical depths due to dust, although star-forming regions can locally exhibit very high extinctions [Behrens et al., 2018]. It is interesting to note that Figure 4 of Behrens et al. [2018] does appear to exhibit a ring-like morphology in the galaxy’s central UV emission, suggesting this effect might persist to higher-resolution simulations. Nonetheless, the relative UV and IR properties of these galaxies are strongly influenced by the presence of dusty, star forming clumps which our simulations could not resolve, suggesting resolution is a main issue for our theoretical predictions.

Our results therefore provide strong motivation for the development of dust models such as the ones presented in this Dissertation in higher-resolution simulations of galaxy formation with more realistic feedback resulting in a manifestly multiphase ISM, as this appears to be essential to capturing the effects to which observations are most sensitive.

CHAPTER 5

CONCLUSION

In this dissertation we have presented the development and predictions of a model for cosmic dust in a simulation of reionization-era galaxy formation. Our physical model is based on successful efforts to predict the dust content of low-redshift galaxies in simple one-zone models of galaxy formation [e.g. Dwek, 1998, Feldmann, 2015] by accounting for the production of dust in evolved stellar remnants, the growth of dust grains due to accretion of heavy elements from the gas phase in the cold molecular ISM, and the destruction of dust due to sputtering in shock-heated gas. Given the profound theoretical uncertainties and lack of independent empirical constraints on all three of these key processes, we develop a flexible post-processing method that allows us to explore an unprecedentedly wide region of dust model parameter space in three-dimensional, spatially-resolved simulations of galaxy formation. We use this flexibility to explore the dependence of predicted reionization-era cosmic dust content on the uncertain parameters of the dust model. Despite a thorough parameter exploration and the self-consistent comparison of observable quantities to our simulations, we are unable to simultaneously match all existing observational constraints. Specifically, our dust models that produce adequate total dust masses to satisfy observations of infrared emission from high redshift galaxies predict far too much extinction in the ultraviolet. As well, an analysis of the spatial distribution of dust in our models indicates that they fail to reproduce the morphological complexity apparent in high resolution observations.

Specifically, in Chapter 2 we presented the model methodology – both its assumed physics and numerical implementation, quantified the relative contributions of different processes for determining the dust contents of a single massive high-redshift galaxy, and demonstrated how these contributions change with varied dust model parameters. We show that the dust content is sensitive to these parameter choices, motivating further efforts to determine if these differences are observable.

To do this, in Chapter 3 we apply our model to a suite of 10 additional galaxies that span the mass range resolved in our simulations. We use 9 different dust model combinations to calculate their dust contents, allowing us to assess the impact of parameter uncertainties. We confirm classic results that the dust contents of galaxies at early times/low metallicities is determined primarily by the assumed dust yields of production sources – supernova and AGB stars – while the dust content at late times/high metallicities is set by the competition between grain growth due to accretion in the ISM and grain destruction due to supernova remnants, normalized by the initial condition set by production yields. We compare predicted dust masses to observational constraints from the literature, and find that our most dust-rich models, due to high production yields and efficient ISM accretion, best reproduce the dust-mass vs. stellar-mass relation seen in data. However, we caution that uncertainties in the observational constraints makes this conclusion tentative.

To enable more direct comparison with observational data, we then forward model directly observable quantities of our simulated galaxies which are sensitive to dust. In the rest-frame UV this is the logarithmic slope of the continuum spectrum, and in the rest-frame IR this is the IR luminosity and the IR-to-UV luminosity excess. We find that our models with the least dust (due to low production yields) best match the UV slopes, but that these models lack sufficient dust mass to reproduce observed IR luminosities, consistent with the dust mass comparison. We also note that no one of our models appears to predict as much scatter in any observable quantity as is seen in data.

We speculate that these deficiencies are due to issues with the spatial distribution of dust relative to stars in our simulations, which may be overly smooth. To assess this hypothesis, in Chapter 4, we compare our simulations to spatially resolved observations of rest-frame UV emission and dust continuum, between which some galaxies show large spatial offsets, indicative of a highly dynamic ISM. We compare galaxies of similar estimated stellar mass to our most massive system, and find that all of our models fail to predict offsets as large

as observed, lending evidence to the idea that our galaxies fail to capture the dynamic complexity of the high-redshift ISM, which is necessary to reproduce observations.

Ours is neither the first model to model cosmic dust processes in a spatially resolved fluid-dynamical cosmological galaxy formation simulation [e.g. Bekki, 2015, McKinnon et al., 2016, 2017, Aoyama et al., 2018, Gjergeric et al., 2018, Hou et al., 2019, Vogelsberger et al., 2019, Davé et al., 2019, Li et al., 2019b, Graziani et al., 2020, Li et al., 2021, Granato et al., 2021, Trebitsch et al., 2021, Parente et al., 2022, Kannan et al., 2022, Lower et al., 2022, Lewis et al., 2023], the first to do so specifically focused on reionization-era galaxies [Wu et al., 2020, Graziani et al., 2020, Trebitsch et al., 2021, Kannan et al., 2022, Lower et al., 2022, Lewis et al., 2023], nor the first to systematically vary dust model parameters to assess their effect on predictions [Bekki, 2015, McKinnon et al., 2016, 2017, Gjergeric et al., 2018, Vogelsberger et al., 2019, Li et al., 2019b, Granato et al., 2021, Parente et al., 2022]. However, to our knowledge we are the first to do all three of these in a single study. Ours is also the most thorough comparison among these studies to observational data for dust in high redshift galaxies, as it considers both rest-frame UV and IR observables as well as morphology, enabled by pioneering works using ALMA [e.g. Le Fèvre et al., 2020, Bouwens et al., 2022b, Bowler et al., 2022] and JWST Roberts-Borsani et al. [e.g. 2022a], Naidu et al. [e.g. 2022b], Robertson et al. [e.g. 2023], Whitler et al. [e.g. 2023]. Since no other dust physics modelling study presents as complete a comparison to observational data on reionization-era galaxies, we are unable to say whether they fare any better. But given the similarities between these models and their comparable (or poorer) resolution, it is not obvious why they would.

We thereby conclude that our current best efforts are inadequate and we still lack a model that fundamentally captures the nature of cosmic dust in high-redshift galaxies, revealing the necessity of greater sophistication in our theoretical efforts. This is an important conclusion in the era of JWST and ALMA, which are causing an explosion in the amount

and quality of empirical constraints on the high-redshift galaxy population (see Chapter 1 and the introductions to Chapters 2 and 3). *All* observations of reionization-era galaxies with these state-of-the-art facilities are impacted by the cosmic dust in these systems. This groundbreaking data will therefore require a better understanding of dust physics processes in the ISM for fruitful physical interpretation, making this an especially urgent theoretical issue.

Obvious opportunities to improve the state of theoretical dust modelling in high-redshift galaxies include the self-consistent coupling of dust dynamical effects to the gas dynamics in galaxy formation simulations, increased simulation resolution so as to better capture the phase structure and dynamics of the chaotic high-redshift ISM, evolving the full grain size distribution and multiple grain species, and carefully calculated grain temperatures for more realistic IR emission predictions. Specifically, we have emphasized that a key failing of our models is their inability to realistically capture large-scale inhomogeneities in the high-redshift ISM, and the effect of radiation pressure on dust is a particularly promising source of feedback through which this might be accomplished [Ziparo et al., 2023]. Efforts to improve galaxy-scale cosmic dust modelling will also be aided by any ability to independently constrain the physical processes governing dust evolution in the ISM, such as from laboratory experiments or molecular-level calculations of individual grain properties [e.g. Potapov et al., 2020], or improved observational and theoretical constraints on the yields of dust production sources [Slavin et al., 2020, Tosi et al., 2022, Dell’Agli et al., 2016]. Given the centrality of dust to the observational properties of galaxies across the electromagnetic spectrum and throughout cosmic time, the stakes are no less than the astrophysical problem of galaxy formation as a whole.

REFERENCES

- Atomic weights and isotopic compositions with relative atomic masses. <https://www.nist.gov/pml/atomic-weights-and-isotopic-compositions-relative-atomic-masses>. Accessed: 2020-12-01.
- Oscar Agertz and Andrey V. Kravtsov. On the Interplay between Star Formation and Feedback in Galaxy Formation Simulations. , 804(1):18, May 2015. doi:10.1088/0004-637X/804/1/18.
- Oscar Agertz, Florent Renaud, Sofia Feltzing, Justin I. Read, Nils Ryde, Eric P. Andersson, Martin P. Rey, Thomas Bensby, and Diane K. Feuillet. VINTERGATAN - I. The origins of chemically, kinematically, and structurally distinct discs in a simulated Milky Way-mass galaxy. , 503(4):5826–5845, June 2021. doi:10.1093/mnras/stab322.
- Hiddo S. B. Algera, Hanae Inami, Pascal A. Oesch, Laura Sommovigo, Rychard J. Bouwens, Michael W. Topping, Sander Schouws, Mauro Stefanon, Daniel P. Stark, Manuel Aravena, Laia Barrufet, Elisabete da Cunha, Pratika Dayal, Ryan Endsley, Andrea Ferrara, Yoshinobu Fudamoto, Valentino Gonzalez, Luca Graziani, Jacqueline A. Hodge, Alexander P. S. Hygate, Ilse de Looze, Themiya Nanayakkara, Raffaella Schneider, and Paul P. van der Werf. The ALMA REBELS survey: the dust-obscured cosmic star formation rate density at redshift 7. , 518(4):6142–6157, February 2023. doi:10.1093/mnras/stac3195.
- G. Aniano, B. T. Draine, L. K. Hunt, K. Sandstrom, D. Calzetti, R. C. Kennicutt, D. A. Dale, M. Galametz, K. D. Gordon, A. K. Leroy, J. D. T. Smith, H. Roussel, M. Sauvage, F. Walter, L. Armus, A. D. Bolatto, M. Boquien, A. Crocker, I. De Looze, J. Donovan Meyer, G. Helou, J. Hinz, B. D. Johnson, J. Koda, A. Miller, E. Montiel, E. J. Murphy, M. Relaño, H. W. Rix, E. Schinnerer, R. Skibba, M. G. Wolfire, and C. W. Engelbracht. Modeling Dust and Starlight in Galaxies Observed by Spitzer and Herschel: The KINGFISH Sample. , 889(2):150, February 2020. doi:10.3847/1538-4357/ab5fdb.
- Shohei Aoyama, Kuan-Chou Hou, Hiroyuki Hirashita, Kentaro Nagamine, and Ikkoh Shimizu. Cosmological simulation with dust formation and destruction. , 478(4):4905–4921, August 2018. doi:10.1093/mnras/sty1431.
- M. Aravena, R. Decarli, F. Walter, R. Bouwens, P. A. Oesch, C. L. Carilli, F. E. Bauer, E. Da Cunha, E. Daddi, J. González-López, R. J. Ivison, D. A. Riechers, I. Smail, A. M. Swinbank, A. Weiss, T. Anguita, R. Bacon, E. Bell, F. Bertoldi, P. Cortes, P. Cox, J. Hodge, E. Ibar, H. Inami, L. Infante, A. Karim, B. Magnelli, K. Ota, G. Popping, P. van der Werf, J. Wagg, and Y. Fudamoto. The ALMA Spectroscopic Survey in the Hubble Ultra Deep Field: Search for [CII] Line and Dust Emission in 6. , 833(1):71, December 2016. doi:10.3847/1538-4357/833/1/71.
- Pablo Arrabal Haro, Mark Dickinson, Steven L. Finkelstein, Seiji Fujimoto, Vital Fernández, Jeyhan S. Kartaltepe, Intae Jung, Justin W. Cole, Denis Burgarella, Katherine Chworowsky, Taylor A. Hutchison, Alexa M. Morales, Casey Papovich, Raymond C.

- Simons, Ricardo O. Amorín, Bren E. Backhaus, Micaela B. Bagley, Laura Bisigello, Antonello Calabrò, Marco Castellano, Nikko J. Cleri, Romeel Davé, Avishai Dekel, Henry C. Ferguson, Adriano Fontana, Eric Gawiser, Mauro Giavalisco, Santosh Harish, Nimish P. Hathi, Michaela Hirschmann, Benne W. Holwerda, Marc Huertas-Company, Anton M. Koekemoer, Rebecca L. Larson, Ray A. Lucas, Bahram Mobasher, Pablo G. Pérez-González, Nor Pirzkal, Caitlin Rose, Paola Santini, Jonathan R. Trump, Alexander de la Vega, Xin Wang, Benjamin J. Weiner, Stephen M. Wilkins, Guang Yang, L. Y. Aaron Yung, and Jorge A. Zavala. Spectroscopic confirmation of CEERS NIRCам-selected galaxies at $z \simeq 8 - 10$. *arXiv e-prints*, art. arXiv:2304.05378, April 2023a. doi:10.48550/arXiv.2304.05378.
- Pablo Arrabal Haro, Mark Dickinson, Steven L. Finkelstein, Jeyhan S. Kartaltepe, Callum T. Donnan, Denis Burgarella, Adam Carnall, Fergus Cullen, James S. Dunlop, Vital Fernández, Seiji Fujimoto, Intae Jung, Melanie Krips, Rebecca L. Larson, Casey Papovich, Pablo G. Pérez-González, Ricardo O. Amorín, Micaela B. Bagley, Véronique Buat, Caitlin M. Casey, Katherine Chworowsky, Seth H. Cohen, Henry C. Ferguson, Mauro Giavalisco, Marc Huertas-Company, Taylor A. Hutchison, Dale D. Kocevski, Anton M. Koekemoer, Ray A. Lucas, Derek J. McLeod, Ross J. McLure, Norbert Pirzkal, Jonathan R. Trump, Benjamin J. Weiner, Stephen M. Wilkins, and Jorge A. Zavala. Spectroscopic verification of very luminous galaxy candidates in the early universe. *arXiv e-prints*, art. arXiv:2303.15431, March 2023b. doi:10.48550/arXiv.2303.15431.
- Martin Asplund, Nicolas Grevesse, A. Jacques Sauval, and Pat Scott. The Chemical Composition of the Sun. *Astronomical Journal*, 47(1):481–522, September 2009. doi:10.1146/annurev.astro.46.060407.145222.
- Tom J. L. C. Bakx, Yoichi Tamura, Takuya Hashimoto, Akio K. Inoue, Minju M. Lee, Ken Mawatari, Kazuaki Ota, Hideki Umehata, Erik Zackrisson, Bunyo Hatsukade, Kotaro Kohno, Yuichi Matsuda, Hiroshi Matsuo, Takashi Okamoto, Takatoshi Shibuya, Ikkoh Shimizu, Yoshiaki Taniguchi, and Naoki Yoshida. ALMA uncovers the [C II] emission and warm dust continuum in a $z = 8.31$ Lyman break galaxy. *MNRAS*, 493(3):4294–4307, April 2020. doi:10.1093/mnras/staa509.
- Tom J. L. C. Bakx, Jorge A. Zavala, Ikki Mitsuhashi, Tommaso Treu, Adriano Fontana, Ken-ichi Tadaki, Caitlin M. Casey, Marco Castellano, Karl Glazebrook, Masato Hagiwara, Ryota Ikeda, Tucker Jones, Nicha Leethochawalit, Charlotte Mason, Takahiro Morishita, Themiya Nanayakkara, Laura Pentericci, Guido Roberts-Borsani, Paola Santini, Stephen Serjeant, Yoichi Tamura, Michele Trenti, and Eros Vanzella. Deep ALMA redshift search of a $z \sim 12$ GLASS-JWST galaxy candidate. *MNRAS*, 519(4):5076–5085, March 2023. doi:10.1093/mnras/stac3723.
- I. Barisic, A. L. Faisst, P. L. Capak, R. Pavesi, D. A. Riechers, N. Z. Scoville, K. Cooke, J. S. Kartaltepe, C. M. Casey, and V. Smolcic. Dust Properties of C II Detected $z \sim 5.5$ Galaxies: New HST/WFC3 Near-IR Observations. *Astronomical Journal*, 845(1):41, August 2017. doi:10.3847/1538-4357/aa7eda.

- L. Barrufet, P. A. Oesch, R. Bouwens, H. Inami, L. Sommovigo, H. Algera, E. da Cunha, M. Aravena, P. Dayal, A. Ferrara, Y. Fudamoto, V. Gonzalez, L. Graziani, A. P. S. Hygate, I. de Looze, T. Nanayakkara, A. Pallottini, R. Schneider, M. Stefanon, M. Topping, and P. van der Werf. The ALMA REBELS Survey: the first infrared luminosity function measurement at $z \sim 7$. , 522(3):3926–3934, July 2023. doi:10.1093/mnras/stad1259.
- C. Behrens, A. Pallottini, A. Ferrara, S. Gallerani, and L. Vallini. Dusty galaxies in the Epoch of Reionization: simulations. , 477(1):552–565, June 2018. doi:10.1093/mnras/sty552.
- Peter Behroozi, Risa H. Wechsler, Andrew P. Hearin, and Charlie Conroy. UNIVERSEMACHINE: The correlation between galaxy growth and dark matter halo assembly from $z = 0-10$. , 488(3):3143–3194, September 2019. doi:10.1093/mnras/stz1182.
- Peter Behroozi, Andrew Hearin, and Benjamin P. Moster. Observational measures of halo properties beyond mass. , 509(2):2800–2824, January 2022. doi:10.1093/mnras/stab3193.
- Peter S. Behroozi, Risa H. Wechsler, and Hao-Yi Wu. The ROCKSTAR Phase-space Temporal Halo Finder and the Velocity Offsets of Cluster Cores. , 762(2):109, January 2013. doi:10.1088/0004-637X/762/2/109.
- Kenji Bekki. Cosmic Evolution of Dust in Galaxies: Methods and Preliminary Results. , 799(2):166, February 2015. doi:10.1088/0004-637X/799/2/166.
- F. Bertoldi, C. L. Carilli, P. Cox, X. Fan, M. A. Strauss, A. Beelen, A. Omont, and R. Zylka. Dust emission from the most distant quasars. , 406:L55–L58, July 2003. doi:10.1051/0004-6361:20030710.
- Rachana Bhatawdekar and Christopher J. Conselice. UV Spectral Slopes at $z = 6-9$ in the Hubble Frontier Fields: Lack of Evidence for Unusual or Population III Stellar Populations. , 909(2):144, March 2021. doi:10.3847/1538-4357/abdd3f.
- S. Bianchi, P. De Vis, S. Viaene, A. Nersesian, A. V. Mosenkov, E. M. Xilouris, M. Baes, V. Casasola, L. P. Cassarà, C. J. R. Clark, J. I. Davies, I. De Looze, W. Dobbels, M. Galametz, F. Galliano, A. P. Jones, S. Lianou, S. C. Madden, and A. Trčka. Fraction of bolometric luminosity absorbed by dust in DustPedia galaxies. , 620:A112, December 2018. doi:10.1051/0004-6361/201833699.
- Simone Bianchi and Raffaella Schneider. Dust formation and survival in supernova ejecta. , 378(3):973–982, July 2007a. doi:10.1111/j.1365-2966.2007.11829.x.
- Simone Bianchi and Raffaella Schneider. Dust formation and survival in supernova ejecta. , 378(3):973–982, July 2007b. doi:10.1111/j.1365-2966.2007.11829.x.
- R. J. Bouwens, G. D. Illingworth, P. A. Oesch, M. Franx, I. Labbé, M. Trenti, P. van Dokkum, C. M. Carollo, V. González, R. Smit, and D. Magee. UV-continuum Slopes at $z \sim 4-7$ from the HUDF09+ERS+CANDELS Observations: Discovery of a Well-defined UV Color-Magnitude Relationship for $z \geq 4$ Star-forming Galaxies. , 754(2):83, August 2012. doi:10.1088/0004-637X/754/2/83.

- R. J. Bouwens, G. D. Illingworth, P. A. Oesch, I. Labbé, P. G. van Dokkum, M. Trenti, M. Franx, R. Smit, V. Gonzalez, and D. Magee. UV-continuum Slopes of >4000 $z \sim 4-8$ Galaxies from the HUDF/XDF, HUDF09, ERS, CANDELS-South, and CANDELS-North Fields. , 793(2):115, October 2014. doi:10.1088/0004-637X/793/2/115.
- R. J. Bouwens, G. D. Illingworth, P. G. van Dokkum, P. A. Oesch, M. Stefanon, and B. Ribeiro. Sizes of Lensed Lower-luminosity $z = 4-8$ Galaxies from the Hubble Frontier Field Program. , 927(1):81, March 2022a. doi:10.3847/1538-4357/ac4791.
- R. J. Bouwens, R. Smit, S. Schouws, M. Stefanon, R. Bowler, R. Endsley, V. Gonzalez, H. Inami, D. Stark, P. Oesch, J. Hodge, M. Aravena, E. da Cunha, P. Dayal, I. de Looze, A. Ferrara, Y. Fudamoto, L. Graziani, C. Li, T. Nanayakkara, A. Pallottini, R. Schneider, L. Sommovigo, M. Topping, P. van der Werf, H. Algera, L. Barrufet, A. Hygate, I. Labbé, D. Riechers, and J. Witstok. Reionization Era Bright Emission Line Survey: Selection and Characterization of Luminous Interstellar Medium Reservoirs in the $z > 6.5$ Universe. , 931(2):160, June 2022b. doi:10.3847/1538-4357/ac5a4a.
- Rychard Bouwens, Jorge González-López, Manuel Aravena, Roberto Decarli, Mladen Novak, Mauro Stefanon, Fabian Walter, Leindert Boogaard, Chris Carilli, Ugnė Dudzevičiūtė, Ian Smail, Emanuele Daddi, Elisabete da Cunha, Rob Ivison, Themiya Nanayakkara, Paulo Cortes, Pierre Cox, Hanae Inami, Pascal Oesch, Gergő Popping, Dominik Riechers, Paul van der Werf, Axel Weiss, Yoshi Fudamoto, and Jeff Wagg. The ALMA Spectroscopic Survey Large Program: The Infrared Excess of $z = 1.5-10$ UV-selected Galaxies and the Implied High-redshift Star Formation History. , 902(2):112, October 2020. doi:10.3847/1538-4357/abb830.
- Rychard Bouwens, Garth Illingworth, Pascal Oesch, Mauro Stefanon, Rohan Naidu, Ivana van Leeuwen, and Dan Magee. UV luminosity density results at $z > 8$ from the first JWST/NIRCam fields: limitations of early data sets and the need for spectroscopy. , 523(1):1009–1035, July 2023. doi:10.1093/mnras/stad1014.
- R. A. A. Bowler, F. Cullen, R. J. McLure, J. S. Dunlop, and A. Avison. The discovery of rest-frame UV colour gradients and a diversity of dust morphologies in bright $z \sim 7$ Lyman-break galaxies. , 510(4):5088–5101, March 2022. doi:10.1093/mnras/stab3744.
- Maruša Bradač, Diego Garcia-Appadoo, Kuang-Han Huang, Livia Vallini, Emily Quinn Finney, Austin Hoag, Brian C. Lemaux, Kasper Borello Schmidt, Tommaso Treu, Chris Carilli, Mark Dijkstra, Andrea Ferrara, Adriano Fontana, Tucker Jones, Russell Ryan, Jeff Wagg, and Anthony H. Gonzalez. ALMA [C II] $158 \mu\text{m}$ Detection of a Redshift 7 Lensed Galaxy behind RXJ1347.1-1145. , 836(1):L2, February 2017. doi:10.3847/2041-8213/836/1/L2.
- Greg L. Bryan and Michael L. Norman. Statistical Properties of X-Ray Clusters: Analytic and Numerical Comparisons. , 495(1):80–99, March 1998. doi:10.1086/305262.

- Andrew J. Bunker, Aayush Saxena, Alex J. Cameron, Chris J. Willott, Emma Curtis-Lake, Peter Jakobsen, Stefano Carniani, Renske Smit, Roberto Maiolino, Joris Witstok, Mirko Curti, Francesco D'Eugenio, Gareth C. Jones, Pierre Ferruit, Santiago Arribas, Stephane Charlot, Jacopo Chevallard, Giovanna Giardino, Anna de Graaff, Tobias J. Looser, Nora Luetzgendorf, Michael V. Maseda, Tim Rawle, Hans-Walter Rix, Bruno Rodriguez Del Pino, Stacey Alberts, Eiichi Egami, Daniel J. Eisenstein, Ryan Endsley, Kevin Hainline, Ryan Hausen, Benjamin D. Johnson, George Rieke, Marcia Rieke, Brant E. Robertson, Irene Shivaee, Daniel P. Stark, Fengwu Sun, Sandro Tacchella, Mengtao Tang, Christina C. Williams, Christopher N. A. Willmer, William M. Baker, Stefi Baum, Rachana Bhatawdekar, Rebecca Bowler, Kristan Boyett, Zuyi Chen, Chiara Circosta, Jakob M. Helton, Zhiyuan Ji, Jianwei Lyu, Erica Nelson, Eleonora Parlanti, Michele Perna, Lester Sandles, Jan Scholtz, Katherine A. Suess, Michael W. Topping, Hannah Uebler, Imaan E. B. Wallace, and Lily Whitler. JADES NIRSpec Spectroscopy of GN-z11: Lyman- α emission and possible enhanced nitrogen abundance in a $z = 10.60$ luminous galaxy. *arXiv e-prints*, art. arXiv:2302.07256, February 2023. doi:10.48550/arXiv.2302.07256.
- D. Burgarella, A. Nanni, H. Hirashita, P. Theulé, A. K. Inoue, and T. T. Takeuchi. Observational and theoretical constraints on the formation and early evolution of the first dust grains in galaxies at $5 < z < 10$. , 637:A32, May 2020. doi:10.1051/0004-6361/201937143.
- Daniela Calzetti, Anne L. Kinney, and Thaisa Storchi-Bergmann. Dust Extinction of the Stellar Continuum in Starburst Galaxies: The Ultraviolet and Optical Extinction Law. , 429:582, July 1994. doi:10.1086/174346.
- P. L. Capak, C. Carilli, G. Jones, C. M. Casey, D. Riechers, K. Sheth, C. M. Carollo, O. Ilbert, A. Karim, O. Lefevre, S. Lilly, N. Scoville, V. Smolcic, and L. Yan. Galaxies at redshifts 5 to 6 with systematically low dust content and high [C II] emission. , 522 (7557):455–458, June 2015. doi:10.1038/nature14500.
- S. Carniani, R. Maiolino, A. Pallottini, L. Vallini, L. Pentericci, A. Ferrara, M. Castellano, E. Vanzella, A. Grazian, S. Gallerani, P. Santini, J. Wagg, and A. Fontana. Extended ionised and clumpy gas in a normal galaxy at $z = 7.1$ revealed by ALMA. , 605:A42, September 2017. doi:10.1051/0004-6361/201630366.
- Daniel Ceverino, Simon C. O. Glover, and Ralf S. Klessen. Introducing the FirstLight project: UV luminosity function and scaling relations of primeval galaxies. , 470(3):2791–2798, September 2017. doi:10.1093/mnras/stx1386.
- Daniel Ceverino, Michaela Hirschmann, Ralf S. Klessen, Simon C. O. Glover, Stéphane Charlot, and Anna Feltre. FirstLight IV: diversity in sub- L_* galaxies at cosmic dawn. , 504(3):4472–4480, July 2021. doi:10.1093/mnras/stab1206.
- Mélanie Chevance, J. M. Diederik Kruijssen, Alexander P. S. Hygate, Andreas Schrubba, Steven N. Longmore, Brent Groves, Jonathan D. Henshaw, Cinthya N. Herrera, Annie Hughes, Sarah M. R. Jeffreson, Philipp Lang, Adam K. Leroy, Sharon E. Meidt, Jérôme Pety, Alessandro Razza, Erik Rosolowsky, Eva Schinnerer, Frank Bigiel, Guillermo A.

- Blanc, Eric Emsellem, Christopher M. Faesi, Simon C. O. Glover, Daniel T. Haydon, I. Ting Ho, Kathryn Kreckel, Janice C. Lee, Daizhong Liu, Miguel Querejeta, Toshiki Saito, Jiayi Sun, Antonio Usero, and Dyas Utomo. The lifecycle of molecular clouds in nearby star-forming disc galaxies. , 493(2):2872–2909, April 2020. doi:10.1093/mnras/stz3525.
- Caleb R. Choban, Dušan Kereš, Philip F. Hopkins, Karin M. Sandstrom, Christopher C. Hayward, and Claude-André Faucher-Giguère. The galactic dust-up: modelling dust evolution in FIRE. , 514(3):4506–4534, August 2022. doi:10.1093/mnras/stac1542.
- Charlie Conroy and James E. Gunn. The Propagation of Uncertainties in Stellar Population Synthesis Modeling. III. Model Calibration, Comparison, and Evaluation. , 712(2):833–857, April 2010. doi:10.1088/0004-637X/712/2/833.
- Asantha Cooray, Jae Calanog, Julie L. Wardlow, J. Bock, C. Bridge, D. Burgarella, R. S. Bussmann, C. M. Casey, D. Clements, A. Conley, D. Farrah, H. Fu, R. Gavazzi, R. J. Ivison, N. La Porte, B. Lo Faro, Brian Ma, G. Magdis, S. J. Oliver, W. A. Osage, I. Pérez-Fournon, D. Riechers, D. Rigopoulou, Douglas Scott, M. Viero, and D. Watson. HerMES: The Rest-frame UV Emission and a Lensing Model for the $z = 6.34$ Luminous Dusty Starburst Galaxy HFLS3. , 790(1):40, July 2014. doi:10.1088/0004-637X/790/1/40.
- Emma Curtis-Lake, Stefano Carniani, Alex Cameron, Stephane Charlot, Peter Jakobsen, Roberto Maiolino, Andrew Bunker, Joris Witstok, Renske Smit, Jacopo Chevallard, Chris Willott, Pierre Ferruit, Santiago Arribas, Nina Bonaventura, Mirko Curti, Francesco D’Eugenio, Marijn Franx, Giovanna Giardino, Tobias J. Looser, Nora Lützgendorf, Michael V. Maseda, Tim Rawle, Hans-Walter Rix, Bruno Rodríguez del Pino, Hannah Übler, Marco Sirianni, Alan Dressler, Eiichi Egami, Daniel J. Eisenstein, Ryan Endsley, Kevin Hainline, Ryan Hausen, Benjamin D. Johnson, Marcia Rieke, Brant Robertson, Irene Shivaiei, Daniel P. Stark, Sandro Tacchella, Christina C. Williams, Christopher N. A. Willmer, Rachana Bhatawdekar, Rebecca Bowler, Kristan Boyett, Zuyi Chen, Anna de Graaff, Jakob M. Helton, Raphael E. Hviding, Gareth C. Jones, Nimisha Kumari, Jianwei Lyu, Erica Nelson, Michele Perna, Lester Sandles, Aayush Saxena, Katherine A. Suess, Fengwu Sun, Michael W. Topping, Imaan E. B. Wallace, and Lily Whitler. Spectroscopic confirmation of four metal-poor galaxies at $z = 10.3$ - 13.2 . *Nature Astronomy*, 7:622–632, May 2023. doi:10.1038/s41550-023-01918-w.
- E. da Cunha, F. Walter, I. R. Smail, A. M. Swinbank, J. M. Simpson, R. Decarli, J. A. Hodge, A. Weiss, P. P. van der Werf, F. Bertoldi, S. C. Chapman, P. Cox, A. L. R. Danielson, H. Dannerbauer, T. R. Greve, R. J. Ivison, A. Karim, and A. Thomson. An ALMA Survey of Sub-millimeter Galaxies in the Extended Chandra Deep Field South: Physical Properties Derived from Ultraviolet-to-radio Modeling. , 806(1):110, June 2015. doi:10.1088/0004-637X/806/1/110.
- Romeel Davé, Daniel Anglés-Alcázar, Desika Narayanan, Qi Li, Mika H. Rafieferantsoa, and Sarah Appleby. SIMBA: Cosmological simulations with black hole growth and feedback. , 486(2):2827–2849, June 2019. doi:10.1093/mnras/stz937.

- P. Dayal, A. Ferrara, L. Sommovigo, R. Bouwens, P. A. Oesch, R. Smit, V. Gonzalez, S. Schouws, M. Stefanon, C. Kobayashi, J. Bremer, H. S. B. Algera, M. Aravena, R. A. A. Bowler, E. da Cunha, Y. Fudamoto, L. Graziani, J. Hodge, H. Inami, I. De Looze, A. Pallottini, D. Riechers, R. Schneider, D. Stark, and R. Endsley. The ALMA REBELS survey: the dust content of $z \sim 7$ Lyman break galaxies. , 512(1):989–1002, May 2022. doi:10.1093/mnras/stac537.
- I. De Looze, M. J. Barlow, B. M. Swinyard, J. Rho, H. L. Gomez, M. Matsuura, and R. Wesson. The dust mass in Cassiopeia A from a spatially resolved Herschel analysis. , 465(3):3309–3342, March 2017. doi:10.1093/mnras/stw2837.
- P. De Vis, S. J. Maddox, H. L. Gomez, A. P. Jones, and L. Dunne. BEDE: Bayesian estimates of dust evolution for nearby galaxies. , 505(3):3228–3246, August 2021. doi:10.1093/mnras/stab1604.
- R. Decarli, F. Walter, B. P. Venemans, E. Bañados, F. Bertoldi, C. Carilli, X. Fan, E. P. Farina, C. Mazzucchelli, D. Riechers, H. W. Rix, M. A. Strauss, R. Wang, and Y. Yang. Rapidly star-forming galaxies adjacent to quasars at redshifts exceeding 6. , 545(7655):457–461, May 2017. doi:10.1038/nature22358.
- Avishai Dekel and Yuval Birnboim. Galaxy bimodality due to cold flows and shock heating. , 368(1):2–20, May 2006. doi:10.1111/j.1365-2966.2006.10145.x.
- F. Dell’Agli, M. Di Criscienzo, M. L. Boyer, and D. A. García-Hernández. Evolved stars in the Local Group galaxies - I. AGB evolution and dust production in IC 1613. , 460(4):4230–4241, August 2016. doi:10.1093/mnras/stw1276.
- F. Dell’Agli, R. Valiante, D. Kamath, P. Ventura, and D. A. García-Hernández. AGB dust and gas ejecta in extremely metal-poor environments. , 486(4):4738–4752, July 2019. doi:10.1093/mnras/stz1164.
- M. Dessauges-Zavadsky, M. Zamojski, W. Rujopakarn, J. Richard, P. Sklias, D. Schaerer, F. Combes, H. Ebeling, T. D. Rawle, E. Egami, F. Boone, B. Clément, J. P. Kneib, K. Nyland, and G. Walth. Molecular gas properties of a lensed star-forming galaxy at $z \sim 3.6$: a case study. , 605:A81, September 2017. doi:10.1051/0004-6361/201628513.
- Benedikt Diemer. COLOSSUS: A Python Toolkit for Cosmology, Large-scale Structure, and Dark Matter Halos. , 239(2):35, Dec 2018. doi:10.3847/1538-4365/aee8c.
- Olivier Doré, Michael W. Werner, Matt Ashby, Pancha Banerjee, Nick Battaglia, James Bauer, Robert A. Benjamin, Lindsey E. Bleem, Jamie Bock, Adwin Boogert, Philip Bull, Peter Capak, Tzu-Ching Chang, Jean Chiar, Seth H. Cohen, Asantha Cooray, Brendan Crill, Michael Cushing, Roland de Putter, Simon P. Driver, Tim Eifler, Chang Feng, Simone Ferraro, Douglas Finkbeiner, B. Scott Gaudi, Tom Greene, Lynne Hillenbrand, Peter A. Höflich, Eric Hsiao, Kevin Huffenberger, Rolf A. Jansen, Woong-Seob Jeong, Bhavin Joshi, Duho Kim, Minjin Kim, J. Davy Kirkpatrick, Phil Korngut, Elisabeth Krause,

Mariska Kriek, Boris Leistedt, Aigen Li, Carey M. Lisse, Phil Maukopf, Matt Mechtley, Gary Melnick, Joseph Mohr, Jeremiah Murphy, Abraham Neben, David Neufeld, Hien Nguyen, Elena Pierpaoli, Jeonghyun Pyo, Jason Rhodes, Karin Sandstrom, Emmanuel Schaan, Kevin C. Schlaufman, John Silverman, Kate Su, Keivan Stassun, Daniel Stevens, Michael A. Strauss, Xander Tielens, Chao-Wei Tsai, Volker Tolls, Stephen Unwin, Marco Viero, Rogier A. Windhorst, and Michael Zemcov. Science Impacts of the SPHEREx All-Sky Optical to Near-Infrared Spectral Survey: Report of a Community Workshop Examining Extragalactic, Galactic, Stellar and Planetary Science. *arXiv e-prints*, art. arXiv:1606.07039, June 2016.

- B. T. Draine. Interstellar Dust Grains. , 41:241–289, January 2003. doi:10.1146/annurev.astro.41.011802.094840.
- B. T. Draine and Brandon S. Hensley. The Dielectric Function of “Astrodust” and Predictions for Polarization in the 3.4 and 10 μm Features. , 909(1):94, March 2021. doi:10.3847/1538-4357/abd6c6.
- B. T. Draine and H. M. Lee. Optical Properties of Interstellar Graphite and Silicate Grains. , 285:89, October 1984. doi:10.1086/162480.
- B. T. Draine and E. E. Salpeter. On the physics of dust grains in hot gas. , 231:77–94, July 1979a. doi:10.1086/157165.
- B. T. Draine and E. E. Salpeter. Destruction mechanisms for interstellar dust. , 231:438–455, July 1979b. doi:10.1086/157206.
- B. T. Draine, D. A. Dale, G. Bendo, K. D. Gordon, J. D. T. Smith, L. Armus, C. W. Engelbracht, G. Helou, Jr. Kennicutt, R. C., A. Li, H. Roussel, F. Walter, D. Calzetti, J. Moustakas, E. J. Murphy, G. H. Rieke, C. Bot, D. J. Hollenbach, K. Sheth, and H. I. Teplitz. Dust Masses, PAH Abundances, and Starlight Intensities in the SINGS Galaxy Sample. , 663(2):866–894, July 2007. doi:10.1086/518306.
- Bruce T. Draine. Evolution of interstellar dust. In Leo Blitz, editor, *The Evolution of the Interstellar Medium*, volume 12 of *Astronomical Society of the Pacific Conference Series*, pages 193–205, January 1990.
- Bruce T. Draine. *Physics of the Interstellar and Intergalactic Medium*. 2011.
- Yohan Dubois, Sébastien Peirani, Christophe Pichon, Julien Devriendt, Raphaël Gavazzi, Charlotte Welker, and Marta Volonteri. The HORIZON-AGN simulation: morphological diversity of galaxies promoted by AGN feedback. , 463(4):3948–3964, December 2016. doi:10.1093/mnras/stw2265.
- J. S. Dunlop, R. J. McLure, B. E. Robertson, R. S. Ellis, D. P. Stark, M. Cirasuolo, and L. de Ravel. A critical analysis of the ultraviolet continuum slopes (β) of high-redshift galaxies: no evidence (yet) for extreme stellar populations at $z > 6$. , 420(1):901–912, February 2012. doi:10.1111/j.1365-2966.2011.20102.x.

- J. S. Dunlop, A. B. Rogers, R. J. McLure, R. S. Ellis, B. E. Robertson, A. Koekemoer, P. Dayal, E. Curtis-Lake, V. Wild, S. Charlot, R. A. A. Bowler, M. A. Schenker, M. Ouchi, Y. Ono, M. Cirasuolo, S. R. Furlanetto, D. P. Stark, T. A. Targett, and E. Schneider. The UV continua and inferred stellar populations of galaxies at $z \sim 7-9$ revealed by the Hubble Ultra-Deep Field 2012 campaign. , 432(4):3520–3533, July 2013. doi:10.1093/mnras/stt702.
- Loretta Dunne, Stephen Eales, Rob Ivison, Haley Morgan, and Mike Edmunds. Type II supernovae as a significant source of interstellar dust. , 424(6946):285–287, July 2003. doi:10.1038/nature01792.
- Eli Dwek. The Evolution of the Elemental Abundances in the Gas and Dust Phases of the Galaxy. , 501:643, July 1998. doi:10.1086/305829.
- Clarke J. Esmerian and Nickolay Y. Gnedin. Modeling Dust Production, Growth, and Destruction in Reionization-era Galaxies with the CROC Simulations: Methods and Parameter Exploration. , 940(1):74, November 2022. doi:10.3847/1538-4357/ac9612.
- A. L. Faisst, P. L. Capak, I. Davidzon, M. Salvato, C. Laigle, O. Ilbert, M. Onodera, G. Hasinger, Y. Kakazu, D. Masters, H. J. McCracken, B. Mobasher, D. Sanders, J. D. Silverman, L. Yan, and N. Z. Scoville. Rest-UV Absorption Lines as Metallicity Estimator: The Metal Content of Star-forming Galaxies at $z \sim 5$. , 822(1):29, May 2016. doi:10.3847/0004-637X/822/1/29.
- A. L. Faisst, D. Schaerer, B. C. Lemaux, P. A. Oesch, Y. Fudamoto, P. Cassata, M. Béthermin, P. L. Capak, O. Le Fèvre, J. D. Silverman, L. Yan, M. Ginolfi, A. M. Koekemoer, L. Morselli, R. Amorín, S. Bardelli, M. Boquien, G. Brammer, A. Cimatti, M. Dessauges-Zavadsky, S. Fujimoto, C. Gruppioni, N. P. Hathi, S. Hemmati, E. Ibar, G. C. Jones, Y. Khusanova, F. Loiacono, F. Pozzi, M. Talia, L. A. M. Tasca, D. A. Riechers, G. Rodighiero, M. Romano, N. Scoville, S. Toft, L. Vallini, D. Vergani, G. Zamorani, and E. Zucca. The ALPINE-ALMA [C II] Survey: Multiwavelength Ancillary Data and Basic Physical Measurements. , 247(2):61, April 2020. doi:10.3847/1538-4365/ab7ccd.
- Claude-André Faucher-Giguère. Recent progress in simulating galaxy formation from the largest to the smallest scales. *Nature Astronomy*, 2:368–373, April 2018. doi:10.1038/s41550-018-0427-y.
- Robert Feldmann. 2014.
- Robert Feldmann. The equilibrium view on dust and metals in galaxies: Galactic outflows drive low dust-to-metal ratios in dwarf galaxies. , 449(3):3274–3292, May 2015. doi:10.1093/mnras/stv552.
- A. Ferrara, S. Viti, and C. Ceccarelli. The problematic growth of dust in high-redshift galaxies. , 463(1):L112–L116, November 2016. doi:10.1093/mnrasl/slw165.

- A. Ferrara, L. Sommovigo, P. Dayal, A. Pallottini, R. J. Bouwens, V. Gonzalez, H. Inami, R. Smit, R. A. A. Bowler, R. Endsley, P. Oesch, S. Schouws, D. Stark, M. Stefanon, M. Aravena, E. da Cunha, I. De Looze, Y. Fudamoto, L. Graziani, J. Hodge, D. Riechers, R. Schneider, H. S. B. Algera, L. Barrufet, A. P. S. Hygate, I. Labbé, C. Li, T. Nanayakkara, M. Topping, and P. van der Werf. The ALMA REBELS Survey. Epoch of Reionization giants: Properties of dusty galaxies at $z \sim 7$. , 512(1):58–72, May 2022. doi:10.1093/mnras/stac460.
- Andrea Ferrara, Andrea Pallottini, and Pratika Dayal. On the stunning abundance of super-early, luminous galaxies revealed by JWST. , 522(3):3986–3991, July 2023. doi:10.1093/mnras/stad1095.
- A. S. Ferrarotti and H. P. Gail. Composition and quantities of dust produced by AGB-stars and returned to the interstellar medium. , 447(2):553–576, February 2006. doi:10.1051/0004-6361:20041198.
- Steven L. Finkelstein, Casey Papovich, Brett Salmon, Kristian Finlator, Mark Dickinson, Henry C. Ferguson, Mauro Giavalisco, Anton M. Koekemoer, Naveen A. Reddy, Robert Bassett, Christopher J. Conselice, James S. Dunlop, S. M. Faber, Norman A. Grogin, Nimish P. Hathi, Dale D. Kocevski, Kamson Lai, Kyoung-Soo Lee, Ross J. McLure, Bahram Mobasher, and Jeffrey A. Newman. Candels: The Evolution of Galaxy Rest-frame Ultraviolet Colors from $z = 8$ to 4. , 756(2):164, September 2012. doi:10.1088/0004-637X/756/2/164.
- Y. Fudamoto, P. A. Oesch, A. Faisst, M. Béthermin, M. Ginolfi, Y. Khusanova, F. Loiacono, O. Le Fèvre, P. Capak, D. Schaerer, J. D. Silverman, P. Cassata, L. Yan, R. Amorin, S. Bardelli, M. Boquien, A. Cimatti, M. Dessauges-Zavadsky, S. Fujimoto, C. Gruppioni, N. P. Hathi, E. Ibar, G. C. Jones, A. M. Koekemoer, G. Lagache, B. C. Lemaux, R. Maiolino, D. Narayanan, F. Pozzi, D. A. Riechers, G. Rodighiero, M. Talia, S. Toft, L. Vallini, D. Vergani, G. Zamorani, and E. Zucca. The ALPINE-ALMA [CII] survey. Dust attenuation properties and obscured star formation at $z \sim 4.4$ -5.8. , 643:A4, November 2020. doi:10.1051/0004-6361/202038163.
- Y. Fudamoto, P. A. Oesch, S. Schouws, M. Stefanon, R. Smit, R. J. Bouwens, R. A. A. Bowler, R. Endsley, V. Gonzalez, H. Inami, I. Labbe, D. Stark, M. Aravena, L. Barrufet, E. da Cunha, P. Dayal, A. Ferrara, L. Graziani, J. Hodge, A. Hutter, Y. Li, I. De Looze, T. Nanayakkara, A. Pallottini, D. Riechers, R. Schneider, G. Ucci, P. van der Werf, and C. White. Normal, dust-obscured galaxies in the epoch of reionization. , 597(7877):489–492, September 2021. doi:10.1038/s41586-021-03846-z.
- C. Gall and J. Hjorth. Maximally Dusty Star-forming Galaxies: Supernova Dust Production and Recycling in Local Group and High-redshift Galaxies. , 868(1):62, November 2018. doi:10.3847/1538-4357/aae520.
- Frédéric Galliano, Maud Galametz, and Anthony P. Jones. The Interstellar Dust Properties

- of Nearby Galaxies. , 56:673–713, September 2018. doi:10.1146/annurev-astro-081817-051900.
- Frédéric Galliano, Angelos Nersesian, Simone Bianchi, Ilse De Looze, Sambit Roychowdhury, Maarten Baes, Viviana Casasola, Letizia P. Cassarà, Wouter Dobbels, Jacopo Fritz, Maud Galametz, Anthony P. Jones, Suzanne C. Madden, Aleksandr Mosenkov, Emmanuel M. Xilouris, and Nathalie Ysard. A nearby galaxy perspective on dust evolution. Scaling relations and constraints on the dust build-up in galaxies with the DustPedia and DGS samples. , 649:A18, May 2021. doi:10.1051/0004-6361/202039701.
- Elena Gavagnin, Andreas Bleuler, Joakim Rosdahl, and Romain Teyssier. Star cluster formation in a turbulent molecular cloud self-regulated by photoionization feedback. , 472(4):4155–4172, December 2017. doi:10.1093/mnras/stx2222.
- Shy Genel, Mark Vogelsberger, Dylan Nelson, Debora Sijacki, Volker Springel, and Lars Hernquist. Following the flow: tracer particles in astrophysical fluid simulations. , 435(2):1426–1442, October 2013. doi:10.1093/mnras/stt1383.
- Eda Gjergo, Gian Luigi Granato, Giuseppe Murante, Cinthia Ragonè-Figueroa, Luca Tornatore, and Stefano Borgani. Dust evolution in galaxy cluster simulations. , 479(2):2588–2606, September 2018. doi:10.1093/mnras/sty1564.
- Nickolay Y. Gnedin. Cosmic Reionization on Computers. I. Design and Calibration of Simulations. , 793(1):29, September 2014. doi:10.1088/0004-637X/793/1/29.
- Nickolay Y. Gnedin. Cosmic Reionization on Computers: Numerical and Physical Convergence. , 821(1):50, April 2016. doi:10.3847/0004-637X/821/1/50.
- Nickolay Y. Gnedin and Tom Abel. Multi-dimensional cosmological radiative transfer with a Variable Eddington Tensor formalism. , 6(7):437–455, October 2001. doi:10.1016/S1384-1076(01)00068-9.
- Nickolay Y. Gnedin and Bruce T. Draine. Line Overlap and Self-Shielding of Molecular Hydrogen in Galaxies. , 795(1):37, November 2014. doi:10.1088/0004-637X/795/1/37.
- Nickolay Y. Gnedin and Nicholas Hollon. Cooling and Heating Functions of Photoionized Gas. , 202(2):13, October 2012. doi:10.1088/0067-0049/202/2/13.
- Nickolay Y. Gnedin and Alexander A. Kaurov. Cosmic Reionization on Computers. II. Reionization History and Its Back-reaction on Early Galaxies. , 793(1):30, September 2014. doi:10.1088/0004-637X/793/1/30.
- Nickolay Y. Gnedin and Andrey V. Kravtsov. Environmental Dependence of the Kennicutt-Schmidt Relation in Galaxies. , 728(2):88, February 2011. doi:10.1088/0004-637X/728/2/88.

- Nickolay Y. Gnedin, Andrey V. Kravtsov, and Douglas H. Rudd. Implementing the DC Mode in Cosmological Simulations with Supercomoving Variables. , 194(2):46, June 2011. doi:10.1088/0067-0049/194/2/46.
- H. L. Gomez, O. Krause, M. J. Barlow, B. M. Swinyard, P. J. Owen, C. J. R. Clark, M. Matsuura, E. L. Gomez, J. Rho, M. A. Besel, J. Bouwman, W. K. Gear, Th. Henning, R. J. Ivison, E. T. Polehampton, and B. Sibthorpe. A Cool Dust Factory in the Crab Nebula: A Herschel Study of the Filaments. , 760(1):96, November 2012. doi:10.1088/0004-637X/760/1/96.
- Gian Luigi Granato, Cinthia Ragone-Figueroa, Antonela Taverna, Laura Silva, Milena Valentini, Stefano Borgani, Pierluigi Monaco, Giuseppe Murante, and Luca Tornatore. Dust evolution in zoom-in cosmological simulations of galaxy formation. , 503(1):511–532, May 2021. doi:10.1093/mnras/stab362.
- Robert J. J. Grand, Facundo A. Gómez, Federico Marinacci, Rüdiger Pakmor, Volker Springel, David J. R. Campbell, Carlos S. Frenk, Adrian Jenkins, and Simon D. M. White. The Auriga Project: the properties and formation mechanisms of disc galaxies across cosmic time. , 467(1):179–207, May 2017. doi:10.1093/mnras/stx071.
- L. Graziani, R. Schneider, M. Ginolfi, L. K. Hunt, U. Maio, M. Glatzle, and B. Ciardi. The assembly of dusty galaxies at $z \geq 4$: statistical properties. , 494(1):1071–1088, May 2020. doi:10.1093/mnras/staa796.
- Michael Y. Grudić, Dávid Guszejnov, Stella S. R. Offner, Anna L. Rosen, Aman N. Raju, Claude-André Faucher-Giguère, and Philip F. Hopkins. The dynamics and outcome of star formation with jets, radiation, winds, and supernovae in concert. , 512(1):216–232, May 2022. doi:10.1093/mnras/stac526.
- Takuya Hashimoto, Akio K. Inoue, Ken Mawatari, Yoichi Tamura, Hiroshi Matsuo, Hisanori Furusawa, Yuichi Harikane, Takatoshi Shibuya, Kirsten K. Knudsen, Kotaro Kohno, Yoshiaki Ono, Erik Zackrisson, Takashi Okamoto, Nobunari Kashikawa, Pascal A. Oesch, Masami Ouchi, Kazuaki Ota, Ikkoh Shimizu, Yoshiaki Taniguchi, Hideki Umehata, and Darach Watson. Big Three Dragons: A $z = 7.15$ Lyman-break galaxy detected in [O III] $88 \mu\text{m}$, [C II] $158 \mu\text{m}$, and dust continuum with ALMA. , 71(4):71, August 2019. doi:10.1093/pasj/psz049.
- Kasper E. Heintz, Gabriel B. Brammer, Clara Giménez-Arteaga, Victoria B. Strait, Claudia del P. Lagos, Aswin P. Vijayan, Jorryt Matthee, Darach Watson, Charlotte A. Mason, Anne Hutter, Sune Toft, Johan P. U. Fynbo, and Pascal A. Oesch. Dilution of chemical enrichment in galaxies 600 Myr after the Big Bang. *arXiv e-prints*, art. arXiv:2212.02890, December 2022. doi:10.48550/arXiv.2212.02890.
- H. Hirashita. Dust-to-gas ratio and phase transition of interstellar medium. , 344:L87–L89, April 1999a.

- H. Hirashita. Dust Processing in the Interstellar Medium. In *Proceedings of The Life Cycle of Dust in the Universe: Observations*, page 27, January 2013.
- Hiroyuki Hirashita. Global Law for the Dust-to-Gas Ratio of Spiral Galaxies. , 510(2): L99–L102, January 1999b. doi:10.1086/311806.
- Hiroyuki Hirashita. Dust Growth Timescale and Mass Function of Molecular Clouds in the Galaxy. , 52:585–588, August 2000. doi:10.1093/pasj/52.4.585.
- Hiroyuki Hirashita and Shohei Aoyama. Remodelling the evolution of grain size distribution in galaxies. , 482(2):2555–2572, January 2019. doi:10.1093/mnras/sty2838.
- Thiem Hoang. Rotational Disruption of Astrophysical Dust and Ice—Theory and Applications. *Galaxies*, 8(3):52, July 2020. doi:10.3390/galaxies8030052.
- Susanne Höfner and Hans Olofsson. Mass loss of stars on the asymptotic giant branch. Mechanisms, models and measurements. , 26(1):1, January 2018. doi:10.1007/s00159-017-0106-5.
- Philip F. Hopkins, Andrew Wetzel, Dušan Kereš, Claude-André Faucher-Giguère, Eliot Quataert, Michael Boylan-Kolchin, Norman Murray, Christopher C. Hayward, Shea Garrison-Kimmel, Cameron Hummels, Robert Feldmann, Paul Torrey, Xiangcheng Ma, Daniel Anglés-Alcázar, Kung-Yi Su, Matthew Orr, Denise Schmitz, Ivanna Escala, Robyn Sanderson, Michael Y. Grudić, Zachary Hafen, Ji-Hoon Kim, Alex Fitts, James S. Bullock, Coral Wheeler, T. K. Chan, Oliver D. Elbert, and Desika Narayanan. FIRE-2 simulations: physics versus numerics in galaxy formation. , 480(1):800–863, October 2018. doi:10.1093/mnras/sty1690.
- Kuan-Chou Hou, Shohei Aoyama, Hiroyuki Hirashita, Kentaro Nagamine, and Ikkoh Shimizu. Dust scaling relations in a cosmological simulation. , 485(2):1727–1744, May 2019. doi:10.1093/mnras/stz121.
- Chia-Yu Hu, Svitlana Zhukovska, Rachel S. Somerville, and Thorsten Naab. Thermal and non-thermal dust sputtering in hydrodynamical simulations of the multiphase interstellar medium. , 487(3):3252–3269, August 2019. doi:10.1093/mnras/stz1481.
- Chia-Yu Hu, Amiel Sternberg, and Ewine F. van Dishoeck. Co-evolution of Dust and Chemistry in Galaxy Simulations with a Resolved Interstellar Medium. *arXiv e-prints*, art. arXiv:2301.05247, January 2023. doi:10.48550/arXiv.2301.05247.
- Yu-Hsiu Huang, Hiroyuki Hirashita, Yun-Hsin Hsu, Yen-Ting Lin, Dylan Nelson, and Andrew P. Cooper. Evolution of the grain size distribution in Milky Way-like galaxies in post-processed IllustrisTNG simulations. , 501(1):1336–1351, February 2021. doi:10.1093/mnras/staa3695.
- J. D. Hunter. Matplotlib: A 2d graphics environment. *Computing in Science & Engineering*, 9(3):90–95, 2007. doi:10.1109/MCSE.2007.55.

- Hanae Inami, Hiddo S. B. Algera, Sander Schouws, Laura Sommovigo, Rychard Bouwens, Renske Smit, Mauro Stefanon, Rebecca A. A. Bowler, Ryan Endsley, Andrea Ferrara, Pascal Oesch, Daniel Stark, Manuel Aravena, Laia Barrufet, Elisabete da Cunha, Pratika Dayal, Ilse De Looze, Yoshinobu Fudamoto, Valentino Gonzalez, Luca Graziani, Jacqueline A. Hodge, Alexander P. S. Hygate, Themiya Nanayakkara, Andrea Pallottini, Dominik A. Riechers, Raffaella Schneider, Michael Topping, and Paul van der Werf. The ALMA REBELS Survey: dust continuum detections at $z > 6.5$. , 515(3):3126–3143, September 2022. doi:10.1093/mnras/stac1779.
- A. K. Inoue. The origin of dust in galaxies revisited: the mechanism determining dust content. *Earth, Planets and Space*, 63(10):1027–1039, October 2011. doi:10.5047/eps.2011.02.013.
- Takuma Izumi, Masafusa Onoue, Hikari Shirakata, Tohru Nagao, Kotaro Kohno, Yoshiki Matsuoka, Masatoshi Imanishi, Michael A. Strauss, Nobunari Kashikawa, Andreas Schulze, John D. Silverman, Seiji Fujimoto, Yuichi Harikane, Yoshiki Toba, Hideki Ume-hata, Kouichiro Nakanishi, Jenny E. Greene, Yoichi Tamura, Akio Taniguchi, Yuki Yamaguchi, Tomotsugu Goto, Yasuhiro Hashimoto, Soh Ikarashi, Daisuke Iono, Kazushi Iwasawa, Chien-Hsiu Lee, Ryu Makiya, Takeo Minezaki, and Ji-Jia Tang. Subaru High- z Exploration of Low-Luminosity Quasars (SHELLQs). III. Star formation properties of the host galaxies at $z \gtrsim 6$ studied with ALMA. , 70(3):36, June 2018. doi:10.1093/pasj/psy026.
- A. P. Jones. Dust Destruction Processes. In Adolf N. Witt, Geoffrey C. Clayton, and Bruce T. Draine, editors, *Astrophysics of Dust*, volume 309 of *Astronomical Society of the Pacific Conference Series*, page 347, May 2004.
- Eric Jones, Travis Oliphant, Pearu Peterson, et al. SciPy: Open source scientific tools for Python, 2001. URL <http://www.scipy.org/>.
- Tucker Jones, Ryan Sanders, Guido Roberts-Borsani, Richard S. Ellis, Nicolas Laporte, Tommaso Treu, and Yuichi Harikane. The Mass-Metallicity Relation at $z \approx 8$: Direct-method Metallicity Constraints and Near-future Prospects. , 903(2):150, November 2020. doi:10.3847/1538-4357/abb943.
- Nissim Kanekar, Jeff Wagg, Ranga Ram Chary, and Christopher L. Carilli. A Search for C II 158 μm Line Emission in HCM 6A, a Ly α Emitter at $z = 6.56$. , 771(2):L20, July 2013. doi:10.1088/2041-8205/771/2/L20.
- R. Kannan, E. Garaldi, A. Smith, R. Pakmor, V. Springel, M. Vogelsberger, and L. Hernquist. Introducing the THESAN project: radiation-magnetohydrodynamic simulations of the epoch of reionization. , 511(3):4005–4030, April 2022. doi:10.1093/mnras/stab3710.
- Rahul Kannan, Federico Marinacci, Mark Vogelsberger, Laura V. Sales, Paul Torrey, Volker Springel, and Lars Hernquist. Simulating the interstellar medium of galaxies with radiative transfer, non-equilibrium thermochemistry, and dust. , 499(4):5732–5748, December 2020. doi:10.1093/mnras/staa3249.

- Ryota Kawamata, Masafumi Ishigaki, Kazuhiro Shimasaku, Masamune Oguri, Masami Ouchi, and Shingo Tanigawa. Size-Luminosity Relations and UV Luminosity Functions at $z = 6-9$ Simultaneously Derived from the Complete Hubble Frontier Fields Data. , 855 (1):4, March 2018. doi:10.3847/1538-4357/aaa6cf.
- Jeong-Gyu Kim, Eve C. Ostriker, and Nina Filippova. Star Formation Efficiency and Dispersal of Giant Molecular Clouds with UV Radiation Feedback: Dependence on Gravitational Boundedness and Magnetic Fields. , 911(2):128, April 2021. doi:10.3847/1538-4357/abe934.
- Florian Kirchschrager, Lars Mattsson, and Frederick A. Gent. Supernova induced processing of interstellar dust: impact of interstellar medium gas density and gas turbulence. , 509 (3):3218–3234, January 2022. doi:10.1093/mnras/stab3059.
- Kirsten K. Knudsen, Johan Richard, Jean-Paul Kneib, Mathilde Jauzac, Benjamin Clément, Guillaume Drouart, Eiichi Egami, and Lukas Lindroos. [C II] emission in $z \sim 6$ strongly lensed, star-forming galaxies. , 462(1):L6–L10, October 2016. doi:10.1093/mnrasl/slw114.
- Kirsten K. Knudsen, Darach Watson, David Frayer, Lise Christensen, Anna Gallazzi, Michał J. Michałowski, Johan Richard, and Jesús Zavala. A merger in the dusty, $z = 7.5$ galaxy A1689-zD1? , 466(1):138–146, April 2017. doi:10.1093/mnras/stw3066.
- Andrey V. Kravtsov. *High-resolution simulations of structure formation in the universe*. PhD thesis, NEW MEXICO STATE UNIVERSITY, January 1999.
- Andrey V. Kravtsov, Anatoly Klypin, and Yehuda Hoffman. Constrained Simulations of the Real Universe. II. Observational Signatures of Intergalactic Gas in the Local Supercluster Region. , 571(2):563–575, June 2002. doi:10.1086/340046.
- Pavel Kroupa. On the variation of the initial mass function. , 322(2):231–246, April 2001. doi:10.1046/j.1365-8711.2001.04022.x.
- Eric Lagadec, Albert A. Zijlstra, Mikako Matsuura, J. W. Menzies, Jacco Th. van Loon, and Patricia A. Whitelock. Dust mass-loss rates from asymptotic giant branch stars in the Fornax and Sagittarius dwarf spheroidal galaxies. , 383(1):399–410, January 2008. doi:10.1111/j.1365-2966.2007.12561.x.
- Danial Langeroodi, Jens Hjorth, Wenlei Chen, Patrick L. Kelly, Hayley Williams, Yu-Heng Lin, Claudia Scarlata, Adi Zitrin, Tom Broadhurst, Jose M. Diego, Xiaosheng Huang, Alexei V. Filippenko, Ryan J. Foley, Saurabh Jha, Anton M. Koekemoer, Masamune Oguri, Ismael Perez-Fournon, Justin Pierel, Frederick Poidevin, and Lou Strolger. Evolution of the Mass-Metallicity Relation from Redshift $z \approx 8$ to the Local Universe. *arXiv e-prints*, art. arXiv:2212.02491, December 2022. doi:10.48550/arXiv.2212.02491.
- N. Laporte, R. S. Ellis, F. Boone, F. E. Bauer, D. Quénard, G. W. Roberts-Borsani, R. Pelló, I. Pérez-Fournon, and A. Streblyanska. Dust in the Reionization Era: ALMA Observations of a $z = 8.38$ Gravitationally Lensed Galaxy. , 837(2):L21, March 2017. doi:10.3847/2041-8213/aa62aa.

- O. Le Fèvre, M. Béthermin, A. Faisst, G. C. Jones, P. Capak, P. Cassata, J. D. Silverman, D. Schaerer, L. Yan, R. Amorin, S. Bardelli, M. Boquien, A. Cimatti, M. Dessauges-Zavadsky, M. Giavalisco, N. P. Hathi, Y. Fudamoto, S. Fujimoto, M. Ginolfi, C. Gruppioni, S. Hemmati, E. Ibar, A. Koekemoer, Y. Khusanova, G. Lagache, B. C. Lemaux, F. Loiacono, R. Maiolino, C. Mancini, D. Narayanan, L. Morselli, Hugo Méndez-Hernández, P. A. Oesch, F. Pozzi, M. Romano, D. Riechers, N. Scoville, M. Talia, L. A. M. Tasca, R. Thomas, S. Toft, L. Vallini, D. Vergani, F. Walter, G. Zamorani, and E. Zucca. The ALPINE-ALMA [CII] survey. Survey strategy, observations, and sample properties of 118 star-forming galaxies at $4 < z < 6$. , 643:A1, November 2020. doi:10.1051/0004-6361/201936965.
- Claus Leitherer, Daniel Schaerer, Jeffrey D. Goldader, Rosa M. González Delgado, Carmelle Robert, Denis Foo Kune, Duília F. de Mello, Daniel Devost, and Timothy M. Heckman. Starburst99: Synthesis Models for Galaxies with Active Star Formation. , 123(1):3–40, July 1999. doi:10.1086/313233.
- Aleksandra Leńniewska and Michał Jerzy Michałowski. Dust production scenarios in galaxies at $z \sim 6$ –8.3. , 624:L13, April 2019. doi:10.1051/0004-6361/201935149.
- Joseph S. W. Lewis, Pierre Ocvirk, Yohan Dubois, Dominique Aubert, Jonathan Chardin, Nicolas Gillet, and Émilie Thélie. DUSTiER (DUST in the Epoch of Reionization): dusty galaxies in cosmological radiation-hydrodynamical simulations of the Epoch of Reionization with RAMSES-CUDATON. , 519(4):5987–6007, March 2023. doi:10.1093/mnras/stad081.
- Hui Li, Mark Vogelsberger, Federico Marinacci, and Oleg Y. Gnedin. Disruption of giant molecular clouds and formation of bound star clusters under the influence of momentum stellar feedback. , 487(1):364–380, July 2019a. doi:10.1093/mnras/stz1271.
- Qi Li, Desika Narayanan, and Romeel Davé. The dust-to-gas and dust-to-metal ratio in galaxies from $z = 0$ to 6. , 490(1):1425–1436, November 2019b. doi:10.1093/mnras/stz2684.
- Qi Li, Desika Narayanan, Paul Torrey, Romeel Davé, and Mark Vogelsberger. The origin of the dust extinction curve in milky way-like galaxies. , 507(1):548–559, October 2021. doi:10.1093/mnras/stab2196.
- Lichen Liang, Robert Feldmann, Christopher C. Hayward, Desika Narayanan, Onur Çatmabacak, Dušan Kereš, Claude-André Faucher-Giguère, and Philip F. Hopkins. The IRX- β relation of high-redshift galaxies. , 502(3):3210–3241, April 2021. doi:10.1093/mnras/stab096.
- U. Lisenfeld and A. Ferrara. Dust-to-Gas Ratio and Metal Abundance in Dwarf Galaxies. , 496(1):145–154, March 1998. doi:10.1086/305354.
- Katharina Lodders. Solar Elemental Abundances. *arXiv e-prints*, art. arXiv:1912.00844, December 2019. doi:10.48550/arXiv.1912.00844.

- Sidney Lower, Desika Narayanan, Qi Li, and Romeel Davé. Cosmic Sands: The Origin of Dusty, Star-forming Galaxies in the Epoch of Reionization. *arXiv e-prints*, art. arXiv:2212.02636, December 2022. doi:10.48550/arXiv.2212.02636.
- Xiangcheng Ma, Philip F. Hopkins, Shea Garrison-Kimmel, Claude-André Faucher-Giguère, Eliot Quataert, Michael Boylan-Kolchin, Christopher C. Hayward, Robert Feldmann, and Dušan Kereš. Simulating galaxies in the reionization era with FIRE-2: galaxy scaling relations, stellar mass functions, and luminosity functions. *MNRAS*, 478(2):1694–1715, August 2018. doi:10.1093/mnras/sty1024.
- Xiangcheng Ma, Christopher C. Hayward, Caitlin M. Casey, Philip F. Hopkins, Eliot Quataert, Lichen Liang, Claude-André Faucher-Giguère, Robert Feldmann, and Dušan Kereš. Dust attenuation, dust emission, and dust temperature in galaxies at $z \geq 5$: a view from the FIRE-2 simulations. *MNRAS*, 487(2):1844–1864, August 2019. doi:10.1093/mnras/stz1324.
- Piero Madau and Mark Dickinson. Cosmic Star-Formation History. *MNRAS*, 52:415–486, August 2014. doi:10.1146/annurev-astro-081811-125615.
- R. Maiolino, S. Carniani, A. Fontana, L. Vallini, L. Pentericci, A. Ferrara, E. Vanzella, A. Grazian, S. Gallerani, M. Castellano, S. Cristiani, G. Brammer, P. Santini, J. Wagg, and R. Williams. The assembly of ‘normal’ galaxies at $z \sim 7$ probed by ALMA. *MNRAS*, 452(1):54–68, September 2015. doi:10.1093/mnras/stv1194.
- M. Mancini, R. Schneider, L. Graziani, R. Valiante, P. Dayal, U. Maio, B. Ciardi, and L. K. Hunt. The dust mass in $z > 6$ normal star-forming galaxies. *MNRAS*, 451:L70–L74, July 2015. doi:10.1093/mnrasl/slv070.
- Mattia Mancini, Raffaella Schneider, Luca Graziani, Rosa Valiante, Pratika Dayal, Umberto Maio, and Benedetta Ciardi. Interpreting the evolution of galaxy colours from $z = 8$ to 5. *MNRAS*, 462(3):3130–3145, November 2016. doi:10.1093/mnras/stw1783.
- D. P. Marrone, J. S. Spilker, C. C. Hayward, J. D. Vieira, M. Aravena, M. L. N. Ashby, M. B. Bayliss, M. Béthermin, M. Brodwin, M. S. Bothwell, J. E. Carlstrom, S. C. Chapman, Chian-Chou Chen, T. M. Crawford, D. J. M. Cunningham, C. De Breuck, C. D. Fassnacht, A. H. Gonzalez, T. R. Greve, Y. D. Hezaveh, K. Lacaille, K. C. Litke, S. Lower, J. Ma, M. Malkan, T. B. Miller, W. R. Morningstar, E. J. Murphy, D. Narayanan, K. A. Phadke, K. M. Rotermund, J. Sreevani, B. Stalder, A. A. Stark, M. L. Strandet, M. Tang, and A. Weiß. Galaxy growth in a massive halo in the first billion years of cosmic history. *Nature*, 553(7686):51–54, January 2018. doi:10.1038/nature24629.
- Charlotte A. Mason, Michele Trenti, and Tommaso Treu. The brightest galaxies at cosmic dawn. *MNRAS*, 521(1):497–503, May 2023. doi:10.1093/mnras/stad035.
- M. Matsuura, M. J. Barlow, A. A. Zijlstra, P. A. Whitelock, M. R. L. Cioni, M. A. T. Groenewegen, K. Volk, F. Kemper, T. Kodama, E. Lagadec, M. Meixner, G. C. Sloan,

- and S. Srinivasan. The global gas and dust budget of the Large Magellanic Cloud: AGB stars and supernovae, and the impact on the ISM evolution. , 396(2):918–934, June 2009. doi:10.1111/j.1365-2966.2009.14743.x.
- M. Matsuura, E. Dwek, M. Meixner, M. Otsuka, B. Babler, M. J. Barlow, J. Roman-Duval, C. Engelbracht, K. Sandstrom, M. Lakićević, J. Th. van Loon, G. Sonneborn, G. C. Clayton, K. S. Long, P. Lundqvist, T. Nozawa, K. D. Gordon, S. Hony, P. Panuzzo, K. Okumura, K. A. Misselt, E. Montiel, and M. Sauvage. Herschel Detects a Massive Dust Reservoir in Supernova 1987A. *Science*, 333(6047):1258, September 2011. doi:10.1126/science.1205983.
- J. Matthee, D. Sobral, L. A. Boogaard, H. Röttgering, L. Vallini, A. Ferrara, A. Paulino-Afonso, F. Boone, D. Schaerer, and B. Mobasher. Resolved UV and [C II] Structures of Luminous Galaxies within the Epoch of Reionization. , 881(2):124, August 2019. doi:10.3847/1538-4357/ab2f81.
- Lars Mattsson and Anja C. Andersen. On the dust abundance gradients in late-type galaxies - II. Analytical models as evidence for massive interstellar dust growth in SINGS galaxies. , 423(1):38–48, June 2012. doi:10.1111/j.1365-2966.2012.20574.x.
- H. J. McCracken, B. Milvang-Jensen, J. Dunlop, M. Franx, J. P. U. Fynbo, O. Le Fèvre, J. Holt, K. I. Caputi, Y. Goranova, F. Buitrago, J. P. Emerson, W. Freudling, P. Hudelot, C. López-Sanjuan, F. Magnard, Y. Mellier, P. Møller, K. K. Nilsson, W. Sutherland, L. Tasca, and J. Zabl. UltraVISTA: a new ultra-deep near-infrared survey in COSMOS. , 544:A156, August 2012. doi:10.1051/0004-6361/201219507.
- C. McKee. Dust Destruction in the Interstellar Medium. In Louis J. Allamandola and A. G. G. M. Tielens, editors, *Interstellar Dust*, volume 135 of *IAU Symposium*, page 431, January 1989.
- Ryan McKinnon, Paul Torrey, and Mark Vogelsberger. Dust formation in Milky Way-like galaxies. , 457(4):3775–3800, April 2016. doi:10.1093/mnras/stw253.
- Ryan McKinnon, Paul Torrey, Mark Vogelsberger, Christopher C. Hayward, and Federico Marinacci. Simulating the dust content of galaxies: successes and failures. , 468(2):1505–1521, June 2017. doi:10.1093/mnras/stx467.
- Ryan McKinnon, Rahul Kannan, Mark Vogelsberger, Stephanie O’Neil, Paul Torrey, and Hui Li. Simulating dust grain-radiation coupling on a moving mesh. *arXiv e-prints*, art. arXiv:1912.02825, December 2019.
- E. R. Micelotta, M. Matsuura, and A. Sarangi. Dust in Supernovae and Supernova Remnants II: Processing and Survival. , 214(2):53, March 2018. doi:10.1007/s11214-018-0484-7.
- Elisabetta R. Micelotta, Eli Dwek, and Jonathan D. Slavin. Dust destruction by the reverse shock in the Cassiopeia A supernova remnant. , 590:A65, May 2016. doi:10.1051/0004-6361/201527350.

- M. J. Michałowski, J. Hjorth, C. Gall, D. T. Frayer, A. L. Tsai, H. Hirashita, K. Rowlands, T. T. Takeuchi, A. Leśniewska, D. Behrendt, N. Bourne, D. H. Hughes, E. Spring, J. Zavala, and P. Bartczak. The fate of the interstellar medium in early-type galaxies. I. First direct measurement of the timescale of dust removal. , 632:A43, December 2019. doi:10.1051/0004-6361/201936055.
- Jordan Mirocha and Steven R. Furlanetto. Balancing the efficiency and stochasticity of star formation with dust extinction in $z \gtrsim 10$ galaxies observed by JWST. , 519(1):843–853, February 2023. doi:10.1093/mnras/stac3578.
- Alexander L. Muratov, Dušan Kereš, Claude-André Faucher-Giguère, Philip F. Hopkins, Eliot Quataert, and Norman Murray. Gusty, gaseous flows of FIRE: galactic winds in cosmological simulations with explicit stellar feedback. , 454(3):2691–2713, December 2015. doi:10.1093/mnras/stv2126.
- Norman Murray, Eliot Quataert, and Todd A. Thompson. The Disruption of Giant Molecular Clouds by Radiation Pressure & the Efficiency of Star Formation in Galaxies. , 709(1):191–209, January 2010. doi:10.1088/0004-637X/709/1/191.
- Norman Murray, Brice Ménard, and Todd A. Thompson. Radiation Pressure from Massive Star Clusters as a Launching Mechanism for Super-galactic Winds. , 735(1):66, July 2011. doi:10.1088/0004-637X/735/1/66.
- Muzammil Mushtaq, Daniel Ceverino, Ralf S. Klessen, Stefan Reissl, and Prajwal Hassan Puttasiddappa. Dust attenuation in galaxies at cosmic dawn from the FirstLight simulations. *arXiv e-prints*, art. arXiv:2304.10150, April 2023. doi:10.48550/arXiv.2304.10150.
- Thorsten Naab and Jeremiah P. Ostriker. Theoretical Challenges in Galaxy Formation. , 55(1):59–109, August 2017. doi:10.1146/annurev-astro-081913-040019.
- Rohan P. Naidu, Pascal A. Oesch, David J. Setton, Jorryt Matthee, Charlie Conroy, Benjamin D. Johnson, John R. Weaver, Rychard J. Bouwens, Gabriel B. Brammer, Pratika Dayal, Garth D. Illingworth, Laia Barrufet, Sirio Belli, Rachel Bezanson, Sownak Bose, Kasper E. Heintz, Joel Leja, Ecaterina Leonova, Rui Marques-Chaves, Mauro Stefanon, Sune Toft, Arjen van der Wel, Pieter van Dokkum, Andrea Weibel, and Katherine E. Whitaker. Schrodinger’s Galaxy Candidate: Puzzlingly Luminous at $z \approx 17$, or Dusty/Quenched at $z \approx 5$? *arXiv e-prints*, art. arXiv:2208.02794, August 2022a. doi:10.48550/arXiv.2208.02794.
- Rohan P. Naidu, Pascal A. Oesch, Pieter van Dokkum, Erica J. Nelson, Katherine A. Suess, Gabriel Brammer, Katherine E. Whitaker, Garth Illingworth, Rychard Bouwens, Sandro Tacchella, Jorryt Matthee, Natalie Allen, Rachel Bezanson, Charlie Conroy, Ivo Labbe, Joel Leja, Ecaterina Leonova, Dan Magee, Sedona H. Price, David J. Setton, Victoria Strait, Mauro Stefanon, Sune Toft, John R. Weaver, and Andrea Weibel. Two Remarkably Luminous Galaxy Candidates at $z \approx 10$ -12 Revealed by JWST. , 940(1):L14, November 2022b. doi:10.3847/2041-8213/ac9b22.

- Kimihiko Nakajima, Masami Ouchi, Yuki Isobe, Yuichi Harikane, Yechi Zhang, Yoshiaki Ono, Hiroya Umeda, and Masamune Oguri. JWST Census for the Mass-Metallicity Star-Formation Relations at $z=4-10$ with the Self-Consistent Flux Calibration and the Proper Metallicity Calibrators. *arXiv e-prints*, art. arXiv:2301.12825, January 2023. doi:10.48550/arXiv.2301.12825.
- Ambra Nanni, Martin A. T. Groenewegen, Bernhard Aringer, Stefano Rubele, Alessandro Bressan, Jacco Th van Loon, Steven R. Goldman, and Martha L. Boyer. The mass-loss, expansion velocities, and dust production rates of carbon stars in the Magellanic Clouds. , 487(1):502–521, July 2019. doi:10.1093/mnras/stz1255.
- Desika Narayanan, J. D. Smith, Brandon Hensley, Qi Li, Chia-Yu Hu, Karin Sandstrom, Paul Torrey, Mark Vogelsberger, Federico Marinacci, and Laura Sales. A Framework for Modeling Polycyclic Aromatic Hydrocarbon Emission in Galaxy Evolution Simulations. *arXiv e-prints*, art. arXiv:2301.07136, January 2023. doi:10.48550/arXiv.2301.07136.
- Isaac Noel, Hanjue Zhu, and Nickolay Gnedin. Mass-Metallicity Relation during the Epoch of Reionization in the CROC Simulations. *arXiv e-prints*, art. arXiv:2210.16750, October 2022. doi:10.48550/arXiv.2210.16750.
- Masami Ouchi, Richard Ellis, Yoshiaki Ono, Kouichiro Nakanishi, Kotaro Kohno, Rieko Momose, Yasutaka Kurono, M. L. N. Ashby, Kazuhiro Shimasaku, S. P. Willner, G. G. Fazio, Yoichi Tamura, and Daisuke Iono. An Intensely Star-forming Galaxy at $z \sim 7$ with Low Dust and Metal Content Revealed by Deep ALMA and HST Observations. , 778(2): 102, December 2013. doi:10.1088/0004-637X/778/2/102.
- A. Pallottini, A. Ferrara, S. Gallerani, L. Vallini, R. Maiolino, and S. Salvadori. Zooming on the internal structure of $z6$ galaxies. , 465(3):2540–2558, March 2017. doi:10.1093/mnras/stw2847.
- A. Pallottini, A. Ferrara, S. Gallerani, C. Behrens, M. Kohandel, S. Carniani, L. Vallini, S. Salvadori, V. Gelli, L. Sommovigo, V. D’Odorico, F. Di Mascia, and E. Pizzati. A survey of high- z galaxies: SERRA simulations. , 513(4):5621–5641, July 2022. doi:10.1093/mnras/stac1281.
- Viraj Pandya, Drummond B. Fielding, Daniel Anglés-Alcázar, Rachel S. Somerville, Greg L. Bryan, Christopher C. Hayward, Jonathan Stern, Chang-Goo Kim, Eliot Quataert, John C. Forbes, Claude-André Faucher-Giguère, Robert Feldmann, Zachary Hafen, Philip F. Hopkins, Dušan Kereš, Norman Murray, and Andrew Wetzel. Characterizing mass, momentum, energy, and metal outflow rates of multiphase galactic winds in the FIRE-2 cosmological simulations. , 508(2):2979–3008, December 2021. doi:10.1093/mnras/stab2714.
- Massimiliano Parente, Cinthia Ragone-Figueroa, Gian Luigi Granato, Stefano Borgani, Giuseppe Murante, Milena Valentini, Alessandro Bressan, and Andrea Lapi. Dust evolution with MUPPI in cosmological volumes. , July 2022. doi:10.1093/mnras/stac1913.

- Riccardo Pavesi, Dominik A. Riechers, Peter L. Capak, Christopher L. Carilli, Chelsea E. Sharon, Gordon J. Stacey, Alexander Karim, Nicholas Z. Scoville, and Vernesa Smolčić. ALMA Reveals Weak [N II] Emission in “Typical” Galaxies and Intense Starbursts at $z = 5-6$. , 832(2):151, December 2016. doi:10.3847/0004-637X/832/2/151.
- Molly S. Peeples, Jessica K. Werk, Jason Tumlinson, Benjamin D. Oppenheimer, J. Xavier Prochaska, Neal Katz, and David H. Weinberg. A Budget and Accounting of Metals at $z \sim 0$: Results from the COS-Halos Survey. , 786(1):54, May 2014. doi:10.1088/0004-637X/786/1/54.
- Céline Péroux and J. Christopher Howk. The Cosmic Baryon and Metal Cycles. , 58:363–406, August 2020. doi:10.1146/annurev-astro-021820-120014.
- M. A. C. Perryman, K. S. de Boer, G. Gilmore, E. Høg, M. G. Lattanzi, L. Lindegren, X. Luri, F. Mignard, O. Pace, and P. T. de Zeeuw. GAIA: Composition, formation and evolution of the Galaxy. , 369:339–363, April 2001. doi:10.1051/0004-6361:20010085.
- Thomas Peters, Svitlana Zhukovska, Thorsten Naab, Philipp Girichidis, Stefanie Walch, Simon C. O. Glover, Ralf S. Klessen, Paul C. Clark, and Daniel Seifried. The turbulent life of dust grains in the supernova-driven, multiphase interstellar medium. , 467(4):4322–4342, June 2017. doi:10.1093/mnras/stx341.
- Annalisa Pillepich, Volker Springel, Dylan Nelson, Shy Genel, Jill Naiman, Rüdiger Pakmor, Lars Hernquist, Paul Torrey, Mark Vogelsberger, Rainer Weinberger, and Federico Marinacci. Simulating galaxy formation with the IllustrisTNG model. , 473(3):4077–4106, January 2018. doi:10.1093/mnras/stx2656.
- Annalisa Pillepich, Dylan Nelson, Volker Springel, Rüdiger Pakmor, Paul Torrey, Rainer Weinberger, Mark Vogelsberger, Federico Marinacci, Shy Genel, Arjen van der Wel, and Lars Hernquist. First results from the TNG50 simulation: the evolution of stellar and gaseous discs across cosmic time. , 490(3):3196–3233, December 2019. doi:10.1093/mnras/stz2338.
- Alexey Potapov, Cornelia Jäger, and Thomas Henning. Ice Coverage of Dust Grains in Cold Astrophysical Environments. , 124(22):221103, June 2020. doi:10.1103/PhysRevLett.124.221103.
- F. Pozzi, F. Calura, Y. Fudamoto, M. Dessauges-Zavadsky, C. Gruppioni, M. Talia, G. Zamorani, M. Bethermin, A. Cimatti, A. Enia, Y. Khusanova, R. Decarli, O. Le Fèvre, P. Capak, P. Cassata, A. L. Faisst, L. Yan, D. Schaerer, J. Silverman, S. Bardelli, M. Boquien, A. Enia, D. Narayanan, M. Ginolfi, N. P. Hathi, G. C. Jones, A. M. Koekemoer, B. C. Lemaux, F. Loiacono, R. Maiolino, D. A. Riechers, G. Rodighiero, M. Romano, L. Vallini, D. Vergani, and E. Zucca. The ALPINE-ALMA [CII] survey. Dust mass budget in the early Universe. , 653:A84, September 2021. doi:10.1051/0004-6361/202040258.

- F. D. Priestley, I. De Looze, and M. J. Barlow. The impact of metallicity-dependent dust destruction on the dust-to-metals ratio in galaxies. , 509(1):L6–L10, January 2022. doi:10.1093/mnrasl/slab114.
- A. Rémy-Ruyer, S. C. Madden, F. Galliano, M. Galametz, T. T. Takeuchi, R. S. Asano, S. Zhukovska, V. Lebouteiller, D. Cormier, A. Jones, M. Bocchio, M. Baes, G. J. Bendo, M. Boquien, A. Boselli, I. DeLooze, V. Doublier-Pritchard, T. Hughes, O. Ł. Karczewski, and L. Spinoglio. Gas-to-dust mass ratios in local galaxies over a 2 dex metallicity range. , 563:A31, March 2014. doi:10.1051/0004-6361/201322803.
- D. Riebel, S. Srinivasan, B. Sargent, and M. Meixner. The Mass-loss Return from Evolved Stars to the Large Magellanic Cloud. VI. Luminosities and Mass-loss Rates on Population Scales. , 753(1):71, July 2012. doi:10.1088/0004-637X/753/1/71.
- Dominik A. Riechers, C. M. Bradford, D. L. Clements, C. D. Dowell, I. Pérez-Fournon, R. J. Ivison, C. Bridge, A. Conley, Hai Fu, J. D. Vieira, J. Wardlow, J. Calanog, A. Cooray, P. Hurley, R. Neri, J. Kamenetzky, J. E. Aguirre, B. Altieri, V. Arumugam, D. J. Benford, M. Béthermin, J. Bock, D. Burgarella, A. Cabrera-Lavers, S. C. Chapman, P. Cox, J. S. Dunlop, L. Earle, D. Farrah, P. Ferrero, A. Franceschini, R. Gavazzi, J. Glenn, E. A. Gonzalez Solares, M. A. Gurwell, M. Halpern, E. Hatziminaoglou, A. Hyde, E. Ibar, A. Kovács, M. Krips, R. E. Lupu, P. R. Maloney, P. Martinez-Navajas, H. Matsuhara, E. J. Murphy, B. J. Naylor, H. T. Nguyen, S. J. Oliver, A. Omont, M. J. Page, G. Petitpas, N. Rangwala, I. G. Roseboom, D. Scott, A. J. Smith, J. G. Staguhn, A. Streblyanska, A. P. Thomson, I. Valtchanov, M. Viero, L. Wang, M. Zemcov, and J. Zmuidzinas. A dust-obscured massive maximum-starburst galaxy at a redshift of 6.34. , 496(7445):329–333, April 2013. doi:10.1038/nature12050.
- Guido Roberts-Borsani, Takahiro Morishita, Tommaso Treu, Gabriel Brammer, Victoria Strait, Xin Wang, Marusa Bradac, Ana Acebron, Pietro Bergamini, Kristan Boyett, Antonello Calabró, Marco Castellano, Adriano Fontana, Karl Glazebrook, Claudio Grillo, Alaina Henry, Tucker Jones, Matthew Malkan, Danilo Marchesini, Sara Mascia, Charlotte Mason, Amata Mercurio, Emiliano Merlin, Themiya Nanayakkara, Laura Pentericci, Piero Rosati, Paola Santini, Claudia Scarlata, Michele Trenti, Eros Vanzella, Benedetta Vulcani, and Chris Willott. Early Results from GLASS-JWST. I: Confirmation of Lensed $z \geq 7$ Lyman-break Galaxies behind the Abell 2744 Cluster with NIRISS. , 938(2):L13, October 2022a. doi:10.3847/2041-8213/ac8e6e.
- Guido Roberts-Borsani, Tommaso Treu, Wenlei Chen, Takahiro Morishita, Eros Vanzella, Adi Zitrin, Pietro Bergamini, Marco Castellano, Adriano Fontana, Karl Glazebrook, Claudio Grillo, Patrick L. Kelly, Emiliano Merlin, Themiya Nanayakkara, Diego Paris, Piero Rosati, Lilan Yang, Ana Acebron, Andrea Bonchi, Kit Boyett, Maruša Bradač, Gabriel Brammer, Tom Broadhurst, Antonello Calabrò, Jose M. Diego, Alan Dressler, Lukas J. Furtak, Alexei V. Filippenko, Alaina Henry, Anton M. Koekemoer, Nicha Leethochawalit, Matthew A. Malkan, Charlotte Mason, Amata Mercurio, Benjamin Metha, Laura Pentericci, Justin Pierel, Steven Rieck, Namrata Roy, Paola Santini, Victoria Strait, Robert

- Strausbaugh, Michele Trenti, Benedetta Vulcani, Lifan Wang, Xin Wang, and Rogier Windhorst. The nature of an ultra-faint galaxy in the cosmic Dark Ages seen with JWST. *arXiv e-prints*, art. arXiv:2210.15639, October 2022b. doi:10.48550/arXiv.2210.15639.
- B. E. Robertson, S. Tacchella, B. D. Johnson, K. Hainline, L. Whitler, D. J. Eisenstein, R. Endsley, M. Rieke, D. P. Stark, S. Alberts, A. Dressler, E. Egami, R. Hausen, G. Rieke, I. Shivaee, C. C. Williams, C. N. A. Willmer, S. Arribas, N. Bonaventura, A. Bunker, A. J. Cameron, S. Carniani, S. Charlot, J. Chevallard, M. Curti, E. Curtis-Lake, F. D’Eugenio, P. Jakobsen, T. J. Looser, N. Lützgendorf, R. Maiolino, M. V. Maseda, T. Rawle, H. W. Rix, R. Smit, H. Übler, C. Willott, J. Witstok, S. Baum, R. Bhatawdekar, K. Boyett, Z. Chen, A. de Graaff, M. Florian, J. M. Helton, R. E. Hviding, Z. Ji, N. Kumari, J. Lyu, E. Nelson, L. Sandles, A. Saxena, K. A. Suess, F. Sun, M. Topping, and I. E. B. Wallace. Identification and properties of intense star-forming galaxies at redshifts $z > 10$. *Nature Astronomy*, 7:611–621, May 2023. doi:10.1038/s41550-023-01921-1.
- Giulia Rodighiero, Laura Bisigello, Edoardo Iani, Antonino Marasco, Andrea Grazian, Francesco Sinigaglia, Paolo Cassata, and Carlotta Gruppioni. JWST unveils heavily obscured (active and passive) sources up to z 13. , 518(1):L19–L24, January 2023. doi:10.1093/mnras/slac115.
- Douglas H. Rudd, Andrew R. Zentner, and Andrey V. Kravtsov. Effects of Baryons and Dissipation on the Matter Power Spectrum. , 672(1):19–32, January 2008. doi:10.1086/523836.
- A. Sarangi, M. Matsuura, and E. R. Micelotta. Dust in Supernovae and Supernova Remnants I: Formation Scenarios. , 214(3):63, April 2018. doi:10.1007/s11214-018-0492-7.
- D. Schaerer, F. Boone, M. Zamojski, J. Staguhn, M. Dessauges-Zavadsky, S. Finkelstein, and F. Combes. New constraints on dust emission and UV attenuation of $z = 6.5$ – 7.5 galaxies from millimeter observations. , 574:A19, February 2015. doi:10.1051/0004-6361/201424649.
- Joop Schaye, Robert A. Crain, Richard G. Bower, Michelle Furlong, Matthieu Schaller, Tom Theuns, Claudio Dalla Vecchia, Carlos S. Frenk, I. G. McCarthy, John C. Helly, Adrian Jenkins, Y. M. Rosas-Guevara, Simon D. M. White, Maarten Baes, C. M. Booth, Peter Camps, Julio F. Navarro, Yan Qu, Alireza Rahmati, Till Sawala, Peter A. Thomas, and James Trayford. The EAGLE project: simulating the evolution and assembly of galaxies and their environments. , 446(1):521–554, January 2015. doi:10.1093/mnras/stu2058.
- Raffaella Schneider, Rosa Valiante, Paolo Ventura, Flavia dell’Agli, Marcella Di Criscienzo, Hiroyuki Hirashita, and Francisca Kemper. Dust production rate of asymptotic giant branch stars in the Magellanic Clouds. , 442(2):1440–1450, August 2014. doi:10.1093/mnras/stu861.
- Sander Schouws, Mauro Stefanon, Rychard Bouwens, Renske Smit, Jacqueline Hodge, Ivo Labbé, Hiddo Algera, Leindert Boogaard, Stefano Carniani, Yoshinobu Fudamoto, Benne W. Holwerda, Garth D. Illingworth, Roberto Maiolino, Michael Maseda, Pascal

- Oesch, and Paul van der Werf. Significant Dust-obscured Star Formation in Luminous Lyman-break Galaxies at z 7-8. , 928(1):31, March 2022. doi:10.3847/1538-4357/ac4605.
- Vadim A. Semenov, Andrey V. Kravtsov, and Nickolay Y. Gnedin. Nonuniversal Star Formation Efficiency in Turbulent ISM. , 826(2):200, August 2016. doi:10.3847/0004-637X/826/2/200.
- Vadim A. Semenov, Andrey V. Kravtsov, and Nickolay Y. Gnedin. The Physical Origin of Long Gas Depletion Times in Galaxies. , 845(2):133, August 2017. doi:10.3847/1538-4357/aa8096.
- Vadim A. Semenov, Andrey V. Kravtsov, and Nickolay Y. Gnedin. How Galaxies Form Stars: The Connection between Local and Global Star Formation in Galaxy Simulations. , 861(1):4, July 2018. doi:10.3847/1538-4357/aac6eb.
- Vadim A. Semenov, Andrey V. Kravtsov, and Damiano Caprioli. Cosmic-Ray Diffusion Suppression in Star-forming Regions Inhibits Clump Formation in Gas-rich Galaxies. , 910(2):126, April 2021a. doi:10.3847/1538-4357/abe2a6.
- Vadim A. Semenov, Andrey V. Kravtsov, and Nickolay Y. Gnedin. Spatial Decorrelation of Young Stars and Dense Gas as a Probe of the Star Formation-Feedback Cycle in Galaxies. , 918(1):13, September 2021b. doi:10.3847/1538-4357/ac0a77.
- Jonathan D. Slavin, Eli Dwek, Mordecai-Mark Mac Low, and Alex S. Hill. The Dynamics, Destruction, and Survival of Supernova-formed Dust Grains. , 902(2):135, October 2020. doi:10.3847/1538-4357/abb5a4.
- Rachel S. Somerville and Romeel Davé. Physical Models of Galaxy Formation in a Cosmological Framework. , 53:51–113, August 2015. doi:10.1146/annurev-astro-082812-140951.
- L. Sommovigo, A. Ferrara, A. Pallottini, P. Dayal, R. J. Bouwens, R. Smit, E. da Cunha, I. De Looze, R. A. A. Bowler, J. Hodge, H. Inami, P. Oesch, R. Endsley, V. Gonzalez, S. Schouws, D. Stark, M. Stefanon, M. Aravena, L. Graziani, D. Riechers, R. Schneider, P. van der Werf, H. Algera, L. Barrufet, Y. Fudamoto, A. P. S. Hygate, I. Labbé, Y. Li, T. Nanayakkara, and M. Topping. The ALMA REBELS Survey: cosmic dust temperature evolution out to z 7. , 513(3):3122–3135, July 2022. doi:10.1093/mnras/stac302.
- Volker Springel and Lars Hernquist. Cosmological smoothed particle hydrodynamics simulations: a hybrid multiphase model for star formation. , 339(2):289–311, February 2003. doi:10.1046/j.1365-8711.2003.06206.x.
- J. Squire and P. F. Hopkins. Resonant Drag Instability of Grains Streaming in Fluids. , 856(1):L15, March 2018. doi:10.3847/2041-8213/aab54d.
- Sundar Srinivasan, Margaret Meixner, Claus Leitherer, Uma Vijh, Kevin Volk, Robert D. Blum, Brian L. Babler, Miwa Block, Steve Bracker, Martin Cohen, Charles W. Engelbracht, Bi-Qing For, Karl D. Gordon, Jason Harris, Joseph L. Hora, Remy Indebetouw,

- Francisca Markwick-Kemper, Marilyn Meade, Karl A. Misselt, Marta Sewilo, and Barbara Whitney. The Mass Loss Return from Evolved Stars to the Large Magellanic Cloud: Empirical Relations for Excess Emission at 8 and 24 μm . , 137(6):4810–4823, June 2009. doi:10.1088/0004-6256/137/6/4810.
- Z. Staniszewski, J. J. Bock, C. M. Bradford, J. Brevik, A. Cooray, Y. Gong, S. Hailey-Dunsheath, R. O’Brient, M. Santos, E. Shirokoff, M. Silva, and M. Zemcov. The Tomographic Ionized-Carbon Mapping Experiment (TIME) CII Imaging Spectrometer. *Journal of Low Temperature Physics*, 176(5-6):767–772, September 2014. doi:10.1007/s10909-014-1126-4.
- M. L. Strandet, A. Weiss, C. De Breuck, D. P. Marrone, J. D. Vieira, M. Aravena, M. L. N. Ashby, M. Béthermin, M. S. Bothwell, C. M. Bradford, J. E. Carlstrom, S. C. Chapman, D. J. M. Cunningham, Chian-Chou Chen, C. D. Fassnacht, A. H. Gonzalez, T. R. Greve, B. Gullberg, C. C. Hayward, Y. Hezaveh, K. Litke, J. Ma, M. Malkan, K. M. Menten, T. Miller, E. J. Murphy, D. Narayanan, K. A. Phadke, K. M. Rotermond, J. S. Spilker, and J. Sreevani. ISM Properties of a Massive Dusty Star-forming Galaxy Discovered at $z \sim 7$. , 842(2):L15, June 2017. doi:10.3847/2041-8213/aa74b0.
- Sandro Tacchella, Daniel J. Eisenstein, Kevin Hainline, Benjamin D. Johnson, William M. Baker, Jakob M. Helton, Brant Robertson, Katherine A. Suess, Zuyi Chen, Erica Nelson, Dávid Puskás, Fengwu Sun, Stacey Alberts, Eiichi Egami, Ryan Hausen, George Rieke, Marcia Rieke, Irene Shivaiei, Christina C. Williams, Christopher N. A. Willmer, Andrew Bunker, Alex J. Cameron, Stefano Carniani, Stephane Charlot, Mirko Curti, Emma Curtis-Lake, Tobias J. Looser, Roberto Maiolino, Michael V. Maseda, Tim Rawle, Hans-Walter Rix, Renske Smit, Hannah Übler, Chris Willott, Joris Witstok, Stefi Baum, Rachana Bhatawdekar, Kristan Boyett, A. Lola Danhaive, Anna de Graaff, Ryan Endsley, Zhiyuan Ji, Jianwei Lyu, Lester Sandles, Aayush Saxena, Jan Scholtz, Michael W. Topping, and Lily Whitler. JADES Imaging of GN-z11: Revealing the Morphology and Environment of a Luminous Galaxy 430 Myr After the Big Bang. *arXiv e-prints*, art. arXiv:2302.07234, February 2023. doi:10.48550/arXiv.2302.07234.
- Yoichi Tamura, Ken Mawatari, Takuya Hashimoto, Akio K. Inoue, Erik Zackrisson, Lise Christensen, Christian Binggeli, Yuichi Matsuda, Hiroshi Matsuo, Tsutomu T. Takeuchi, Ryosuke S. Asano, Kaho Sunaga, Ikkoh Shimizu, Takashi Okamoto, Naoki Yoshida, Minju M. Lee, Takatoshi Shibuya, Yoshiaki Taniguchi, Hideki Umehata, Bunyo Hatsukade, Kotaro Kohno, and Kazuaki Ota. Detection of the Far-infrared [O III] and Dust Emission in a Galaxy at Redshift 8.312: Early Metal Enrichment in the Heart of the Reionization Era. , 874(1):27, March 2019. doi:10.3847/1538-4357/ab0374.
- Todd A. Thompson, Andrew C. Fabian, Eliot Quataert, and Norman Murray. Dynamics of dusty radiation-pressure-driven shells and clouds: fast outflows from galaxies, star clusters, massive stars, and AGN. , 449(1):147–161, May 2015. doi:10.1093/mnras/stv246.
- S. Tosi, D. Kamath, F. Dell’Agli, H. Van Winckel, P. Ventura, T. Marchetti, E. Marini, and M. Tailo. A study of carbon-rich post-AGB stars in the Milky Way to understand the pro-

- duction of carbonaceous dust from evolved stars. , 673:A41, May 2023. doi:10.1051/0004-6361/202245563.
- Silvia Tosi, Flavia Dell’Agli, Erendira Huerta-Martinez, and Paolo Ventura. Dust Formation in the Wind of AGB Stars—The Effects of Mass, Metallicity and Gas-Dust Drift. *Universe*, 8(5):270, May 2022. doi:10.3390/universe8050270.
- Maxime Trebitsch, Yohan Dubois, Marta Volonteri, Hugo Pfister, Corentin Cadiou, Harley Katz, Joakim Rosdahl, Taysun Kimm, Christophe Pichon, Ricarda S. Beckmann, Julien Devriendt, and Adrienne Slyz. The OBELISK simulation: Galaxies contribute more than AGN to H I reionization of protoclusters. , 653:A154, September 2021. doi:10.1051/0004-6361/202037698.
- M. J. Turk, B. D. Smith, J. S. Oishi, S. Skory, S. W. Skillman, T. Abel, and M. L. Norman. yt: A Multi-code Analysis Toolkit for Astrophysical Simulation Data. *The Astrophysical Journal Supplement Series*, 192:9, January 2011. doi:10.1088/0067-0049/192/1/9.
- Rosa Valiante, Raffaella Schneider, Simone Bianchi, and Anja C. Andersen. Stellar sources of dust in the high-redshift Universe. , 397(3):1661–1671, August 2009. doi:10.1111/j.1365-2966.2009.15076.x.
- B. P. Venemans, R. G. McMahon, F. Walter, R. Decarli, P. Cox, R. Neri, P. Hewett, D. J. Mortlock, C. Simpson, and S. J. Warren. Detection of Atomic Carbon [C II] 158 μm and Dust Emission from a $z = 7.1$ Quasar Host Galaxy. , 751(2):L25, June 2012. doi:10.1088/2041-8205/751/2/L25.
- Bram P. Venemans, Fabian Walter, Roberto Decarli, Eduardo Bañados, Chris Carilli, Jan Martin Winters, Karl Schuster, Elisabete da Cunha, Xiaohui Fan, Emanuele Paolo Farina, Chiara Mazzucchelli, Hans-Walter Rix, and Axel Weiss. Copious Amounts of Dust and Gas in a $z = 7.5$ Quasar Host Galaxy. , 851(1):L8, December 2017. doi:10.3847/2041-8213/aa943a.
- Pauli Virtanen, Ralf Gommers, Travis E. Oliphant, Matt Haberland, Tyler Reddy, David Cournapeau, Evgeni Burovski, Pearu Peterson, Warren Weckesser, Jonathan Bright, Stéfan J. van der Walt, Matthew Brett, Joshua Wilson, K. Jarrod Millman, Nikolay Mayorov, Andrew R. J. Nelson, Eric Jones, Robert Kern, Eric Larson, C J Carey, İlhan Polat, Yu Feng, Eric W. Moore, Jake VanderPlas, Denis Laxalde, Josef Perktold, Robert Cimrman, Ian Henriksen, E. A. Quintero, Charles R. Harris, Anne M. Archibald, Antônio H. Ribeiro, Fabian Pedregosa, Paul van Mulbregt, and SciPy 1.0 Contributors. SciPy 1.0: Fundamental Algorithms for Scientific Computing in Python. *Nature Methods*, 17:261–272, 2020. doi:10.1038/s41592-019-0686-2.
- Mark Vogelsberger, Ryan McKinnon, Stephanie O’Neil, Federico Marinacci, Paul Torrey, and Rahul Kannan. Dust in and around galaxies: dust in cluster environments and its impact on gas cooling. , 487(4):4870–4883, August 2019. doi:10.1093/mnras/stz1644.

- Mark Vogelsberger, Federico Marinacci, Paul Torrey, and Ewald Puchwein. Cosmological simulations of galaxy formation. *Nature Reviews Physics*, 2(1):42–66, January 2020. doi:10.1038/s42254-019-0127-2.
- Stéfan van der Walt, S. Chris Colbert, and Gaël Varoquaux. The numpy array: A structure for efficient numerical computation. *Computing in Science & Engineering*, 13(2):22–30, 2011. doi:10.1109/MCSE.2011.37. URL <https://aip.scitation.org/doi/abs/10.1109/MCSE.2011.37>.
- F. Walter, R. Decarli, C. Carilli, D. Riechers, F. Bertoldi, A. Weiß, P. Cox, R. Neri, R. Maiolino, M. Ouchi, E. Egami, and K. Nakanishi. Evidence for Low Extinction in Actively Star-forming Galaxies at $z > 6.5$. , 752(2):93, June 2012. doi:10.1088/0004-637X/752/2/93.
- Liang Wang, Aaron A. Dutton, Gregory S. Stinson, Andrea V. Macciò, Camilla Penzo, Xi Kang, Ben W. Keller, and James Wadsley. NIHAO project - I. Reproducing the inefficiency of galaxy formation across cosmic time with a large sample of cosmological hydrodynamical simulations. , 454(1):83–94, November 2015. doi:10.1093/mnras/stv1937.
- Ran Wang, Jeff Wagg, Chris L. Carilli, Fabian Walter, Lindley Lentati, Xiaohui Fan, Dominik A. Riechers, Frank Bertoldi, Desika Narayanan, Michael A. Strauss, Pierre Cox, Alain Omont, Karl M. Menten, Kirsten K. Knudsen, Roberto Neri, and Linhua Jiang. Star Formation and Gas Kinematics of Quasar Host Galaxies at $z \sim 6$: New Insights from ALMA. , 773(1):44, August 2013. doi:10.1088/0004-637X/773/1/44.
- Darach Watson, Lise Christensen, Kirsten Kraiberg Knudsen, Johan Richard, Anna Gallazzi, and Michał Jerzy Michałowski. A dusty, normal galaxy in the epoch of reionization. , 519(7543):327–330, March 2015. doi:10.1038/nature14164.
- E. Waxman and B. T. Draine. Dust Sublimation by Gamma-ray Bursts and Its Implications. , 537(2):796–802, July 2000. doi:10.1086/309053.
- Rainer Weinberger, Volker Springel, Lars Hernquist, Annalisa Pillepich, Federico Marinacci, Rüdiger Pakmor, Dylan Nelson, Shy Genel, Mark Vogelsberger, Jill Naiman, and Paul Torrey. Simulating galaxy formation with black hole driven thermal and kinetic feedback. , 465(3):3291–3308, March 2017. doi:10.1093/mnras/stw2944.
- Joseph C. Weingartner and B. T. Draine. Interstellar Depletion onto Very Small Dust Grains. , 517(1):292–298, May 1999. doi:10.1086/307197.
- Joseph C. Weingartner and B. T. Draine. Dust Grain-Size Distributions and Extinction in the Milky Way, Large Magellanic Cloud, and Small Magellanic Cloud. , 548(1):296–309, February 2001. doi:10.1086/318651.
- Lily Whitler, Ryan Endsley, Daniel P. Stark, Michael Topping, Zuyi Chen, and Stéphane Charlot. On the ages of bright galaxies 500 Myr after the big bang: insights into star formation activity at $z \gtrsim 15$ with JWST. , 519(1):157–171, February 2023. doi:10.1093/mnras/stac3535.

- Robert P. C. Wiersma, Joop Schaye, and Britton D. Smith. The effect of photoionization on the cooling rates of enriched, astrophysical plasmas. , 393(1):99–107, February 2009. doi:10.1111/j.1365-2966.2008.14191.x.
- Stephen M. Wilkins, Andrew J. Bunker, Elizabeth Stanway, Silvio Lorenzoni, and Joseph Caruana. The ultraviolet properties of star-forming galaxies - I. HST WFC3 observations of very high redshift galaxies. , 417(1):717–729, October 2011. doi:10.1111/j.1365-2966.2011.19315.x.
- Stephen M. Wilkins, Rychard J. Bouwens, Pascal A. Oesch, Ivo Labbé, Mark Sargent, Joseph Caruana, Julie Wardlow, and Scott Clay. Quantifying the UV-continuum slopes of galaxies to $z \sim 10$ using deep Hubble+Spitzer/IRAC observations. , 455(1):659–667, January 2016. doi:10.1093/mnras/stv2263.
- Hayley Williams, Patrick L. Kelly, Wenlei Chen, Gabriel Brammer, Adi Zitrin, Tommaso Treu, Claudia Scarlata, Anton M. Koekemoer, Masamune Oguri, Yu-Heng Lin, Jose M. Diego, Mario Nonino, Jens Hjorth, Danial Langeroodi, Tom Broadhurst, Noah Rogers, Ismael Perez-Fournon, Ryan J. Foley, Saurabh Jha, Alexei V. Filippenko, Lou Strolger, Justin Pierel, Frederick Poidevin, and Lilan Yang. A magnified compact galaxy at redshift 9.51 with strong nebular emission lines. *Science*, 380(6643):416–420, April 2023. doi:10.1126/science.adf5307.
- Chris J. Willott, Ross J. McLure, Pascale Hibon, Richard Bielby, Henry J. McCracken, Jean-Paul Kneib, Olivier Ilbert, David G. Bonfield, Victoria A. Bruce, and Matt J. Jarvis. An Exponential Decline at the Bright End of the $z = 6$ Galaxy Luminosity Function. , 145(1):4, January 2013. doi:10.1088/0004-6256/145/1/4.
- Chris J. Willott, Chris L. Carilli, Jeff Wagg, and Ran Wang. Star Formation and the Interstellar Medium in $z > 6$ UV-luminous Lyman-break Galaxies. , 807(2):180, July 2015. doi:10.1088/0004-637X/807/2/180.
- Joris Witstok, Gareth C. Jones, Roberto Maiolino, Renske Smit, and Raffaella Schneider. An empirical study of dust properties at the earliest epochs. , May 2023. doi:10.1093/mnras/stad1470.
- Xiaohan Wu, Romeel Davé, Sandro Tacchella, and Jennifer Lotz. Photometric properties of reionization-epoch galaxies in the SIMBA simulations. , 494(4):5636–5651, June 2020. doi:10.1093/mnras/staa1044.
- J. A. Zavala, C. M. Casey, S. M. Manning, M. Aravena, M. Bethermin, K. I. Caputi, D. L. Clements, E. da Cunha, P. Drew, S. L. Finkelstein, S. Fujimoto, C. Hayward, J. Hodge, J. S. Kartaltepe, K. Knudsen, A. M. Koekemoer, A. S. Long, G. E. Magdis, A. W. S. Man, G. Popping, D. Sanders, N. Scoville, K. Sheth, J. Staguhn, S. Toft, E. Treister, J. D. Vieira, and M. S. Yun. The Evolution of the IR Luminosity Function and Dust-obscured Star Formation over the Past 13 Billion Years. , 909(2):165, March 2021. doi:10.3847/1538-4357/abdb27.

Jorge A. Zavala, Véronique Buat, Caitlin M. Casey, Steven L. Finkelstein, Denis Burgarella, Micaela B. Bagley, Laure Ciesla, Emanuele Daddi, Mark Dickinson, Henry C. Ferguson, Maximilien Franco, E. F. Jiménez-Andrade, Jeyhan S. Kartaltepe, Anton M. Koekemoer, Aurélien Le Bail, E. J. Murphy, Casey Papovich, Sandro Tacchella, Stephen M. Wilkins, Itziar Aretxaga, Peter Behroozi, Jaclyn B. Champagne, Adriano Fontana, Mauro Gialisco, Andrea Grazian, Norman A. Grogin, Lisa J. Kewley, Dale D. Kocevski, Allison Kirkpatrick, Jennifer M. Lotz, Laura Pentericci, Pablo G. Pérez-González, Nor Pirzkal, Swara Ravindranath, Rachel S. Somerville, Jonathan R. Trump, Guang Yang, L. Y. Aaron Yung, Omar Almaini, Ricardo O. Amorín, Marianna Annunziatella, Pablo Arrabal Haro, Bren E. Backhaus, Guillermo Barro, Eric F. Bell, Rachana Bhatawdekar, Laura Bisigello, Fernando Buitrago, Antonello Calabrò, Marco Castellano, Óscar A. Chávez Ortiz, Katherine Chworowsky, Nikko J. Cleri, Seth H. Cohen, Justin W. Cole, Kevin C. Cooke, M. C. Cooper, Asantha R. Cooray, Luca Costantin, Isabella G. Cox, Darren Croton, Romeel Davé, Alexander de La Vega, Avishai Dekel, David Elbaz, Vicente Estrada-Carpenter, Vital Fernández, Keely D. Finkelstein, Jonathan Freundlich, Seiji Fujimoto, Ángela García-Argumánéz, Jonathan P. Gardner, Eric Gawiser, Carlos Gómez-Guijarro, Yuchen Guo, Timothy S. Hamilton, Nimish P. Hathi, Benne W. Holwerda, Michaela Hirschmann, Marc Huertas-Company, Taylor A. Hutchison, Kartheik G. Iyer, Anne E. Jaskot, Saurabh W. Jha, Shardha Jogee, Stéphanie Juneau, Intae Jung, Susan A. Kassin, Peter Kurczynski, Rebecca L. Larson, Gene C. K. Leung, Arianna S. Long, Ray A. Lucas, Benjamin Maggelli, Kameswara Bharadwaj Mantha, Jasleen Matharu, Elizabeth J. McGrath, Daniel H. McIntosh, Aubrey Medrano, Emiliano Merlin, Bahram Mobasher, Alexa M. Morales, Jeffrey A. Newman, David C. Nicholls, Viraj Pandya, Marc Rafelski, Kaila Ronayne, Caitlin Rose, Russell E. Ryan, Paola Santini, Lise-Marie Seillé, Ekta A. Shah, Lu Shen, Raymond C. Simons, Gregory F. Snyder, Elizabeth R. Stanway, Amber N. Straughn, Harry I. Teplitz, Brittany N. Vanderhoof, Jesús Vega-Ferrero, Weichen Wang, Benjamin J. Weiner, Christopher N. A. Willmer, Stijn Wuyts, and (The Ceers Team). Dusty Starbursts Masquerading as Ultra-high Redshift Galaxies in JWST CEERS Observations. , 943(2):L9, February 2023. doi:10.3847/2041-8213/acacfe.

Hanjue Zhu, Camille Avestruz, and Nikolay Y. Gnedin. Cosmic Reionization On Computers: The Galaxy-Halo Connection between $5 \leq z \leq 10$. , 899(2):137, August 2020. doi:10.3847/1538-4357/aba26d.

S. Zhukovska, H. P. Gail, and M. Tieloff. Evolution of interstellar dust and stardust in the solar neighbourhood. , 479(2):453–480, February 2008. doi:10.1051/0004-6361:20077789.

Svitlana Zhukovska, Clare Dobbs, Edward B. Jenkins, and Ralf S. Klessen. Modeling Dust Evolution in Galaxies with a Multiphase, Inhomogeneous ISM. , 831(2):147, November 2016. doi:10.3847/0004-637X/831/2/147.

Francesco Ziparo, Andrea Ferrara, Laura Sommovigo, and Mahsa Kohandel. Blue monsters. Why are JWST super-early, massive galaxies so blue? , 520(2):2445–2450, April 2023. doi:10.1093/mnras/stad125.